

STRUCTURE-PROPERTY RELATIONSHIPS OF DISSIMILAR FRICTION STIR WELDED  
ALUMINUM ALLOYS

by

ROGIE IRWIN RODRIGUEZ QUIÑONES

J. BRIAN JORDON, COMMITTEE CHAIR

VIOLA L. ACOFF  
PAUL G. ALLISON  
MARK E. BARKEY  
YUBEIN GUO

A DISSERTATION

Submitted in partial fulfillment of the requirements  
for the degree of Doctor of Philosophy  
in the Department of Mechanical Engineering  
in the Graduate School of  
The University of Alabama

TUSCALOOSA, ALABAMA

2015

Copyright Rogie I. Rodriguez Quiñones 2015  
ALL RIGHTS RESERVED

## ABSTRACT

In this work, the relationship between microstructure and mechanical properties of dissimilar friction stir welded AA6061-to-AA7050 aluminum alloys were evaluated. Experimental results from this study revealed that static strength increased with the tool rotational speed and was correlated with the material intermixing. Fully-reversed low cycle fatigue experimental results showed an increase in the strain hardening properties as well as the number of cycles-to-failure as the tool rotational speed was increased. Furthermore, under both static and cyclic loading, fracture of the joint was dominated by the AA6061 alloy side of the weld. In addition, inspection of the fatigue surfaces revealed that cracks initiated from intermetallic particles located near the surface. In order to determine the corrosion resistance of the dissimilar joint, corrosion defects were produced on the crown surface of the weld by static immersion in 3.5% NaCl for various exposure times. Results revealed localized corrosion damage in the thermo-mechanically affected and heat affected zones. Results demonstrated a decrease in the fatigue life, with evidence of crack initiation at the corrosion defects; however, the fatigue life was nearly independent of the exposure time. This can be attributed to total fatigue life dominated by incubation time. Furthermore, two types of failure were observed: fatigue crack initiation in the AA6061 side at high strain amplitudes ( $>0.3\%$ ); and fatigue crack initiation in the AA7050 side at low strain amplitudes ( $<0.2\%$ ). Lastly, a microstructure-sensitive model based on a multi-stage fatigue damage concept was extended to the dissimilar friction stir welded joints in order to capture the crack initiation and propagation in as-welded and pre-corroded conditions. Good

correlation between experimental fatigue results and the model was achieved based on the variation in the initial defect size, microstructure, and mechanical properties of the dissimilar friction stir welded AA6061-to-AA7050 aluminum alloys.

## DEDICATION

... to God, my family, friends and mentors. For all the support throughout this journey.

## LIST OF ABBREVIATIONS AND SYMBOLS

EAfs	Expeditionary airfields
PSP	pierced steel plank
AM-2	Aluminum matting
lbs	pounds
FSW	Friction stir welding
TWI	The Welding Institute
SLS	Space Launch System
ULA	United Space Launch Alliance
FSSW	Friction stir spot welding
SZ	Stir zone
TMAZ	Thermo-mechanically affected zone
HAZ	Heat affected zone
BM	Base material
AS	Advancing side
RS	Retreating side
OM	Optical microscopy
SEM	Scanning electron microscopy
EDS	Energy dispersive x-ray spectrometry
UTS, $S_u$	Ultimate tensile strength
YS, $S_y$	Yield strength

MPa	Mega Pascal
DRX	Dynamic recrystallization
GPa	Giga Pascal
AWS	American Welding Society
MSF	Multistage fatigue model
$E$	Elastic modulus
$\varepsilon$	Elongation
$K$	Strength coefficient
$n$	Hardening exponent
$\sigma'_f$	Fatigue strength coefficient
$b$	Fatigue strength exponent
$\varepsilon_f$	Fatigue ductility coefficient
$c$	fatigue ductility exponent
$N_f$	Number of cycles to failure
$\sigma_{ys,c}$	Cyclic yield strength
$n'$	Cyclic hardening exponent
$K'$	Cyclic strength coefficient
$\varepsilon'_f$	Fatigue ductility coefficient
$c$	Fatigue ductility exponent
$N_{Total}$	Total fatigue life
$N_{Inc}$	Number of cycles required for the crack incubation
$N_{MSC/PSC}$	Number of cycles required for the propagation of the microstructurally small/physically small crack ( <i>MSC/PSC</i> )
$N_{LC}$	Propagation of the long crack ( <i>LC</i> )
$C_{INC}$	Coefficient value obtained for the modified Coffin-Manson

	law for incubation
$\alpha$	Exponent value obtained for the modified Coffin-Manson law for incubation
$C_m$	MSF model constant
$C_n$	MSF model constant
R	Load ratio
$z$	Localization multiplier
$D$	The size of the critical inclusion where that crack incubates
$l$	The size of the plastic zone in front of the inclusion
$n_{lim}$	Limiting factor that defines the transition from constrained to unconstrained micronotch root plasticity
$\Delta CTD$	Crack tip opening displacement range
$\Delta CTD_{th}$	Crack tip displacement threshold
$\chi$	Material constant (0.32 for Al alloys)
$a_i$	Initial crack length
$C_I$	Low cycle fatigue coefficient
$C_{II}$	Coefficient for high cycle fatigue regime
$\zeta$	Exponent for high cycle fatigue regime
$\Delta \hat{\sigma}$	Equivalent uniaxial stress amplitude
$U.$	Means stress effects
LEFM	Linear elastic fracture mechanics

## ACKNOWLEDGEMENTS

I would like to acknowledge my family, friends and mentors for their continuous encouragement and support during this path. I would like to thank my parents and my sister for their unconditional support. Also, I would like to thank my friends and research colleagues, Joao Moraes, Robert McCullough, Dr. Harish Roao, Cuddy Rickard, Oscar Rivera, Abby Cysco and Omar Rodriguez. Furthermore, I would like to thank my graduate committee and mentors, Dr. J. Brian Jordon, Dr. Paul Allison, Dr. Mark Barkey, Dr. Yubein Guo, and Dr. Viola Acoff, for believing in me and for guiding me from the very beginning. Additionally, I would like to thank all the staff the Central Analytical Facility, which is supported by The University of Alabama, Rich Marteens, Rob Holler, Johny Goodwin and Dr. Fernando Laiginnhas for the constant support using the analytical equipment. Also, I would also to acknowledge the GAANN Fellowship Program and The Boeing Company for the supporting my graduate studies.

## CONTENTS

ABSTRACT .....	ii
DEDICATION .....	iv
LIST OF ABBREVIATIONS AND SYMBOLS .....	v
ACKNOWLEDGEMENTS .....	viii
LIST OF TABLES .....	xii
LIST OF FIGURES .....	xiii
CHAPTER 1 INTRODUCTION .....	1
1.1 Research Justification .....	1
1.2 Friction Stir Welding .....	5
1.2.1 High Strength Aluminum Alloys .....	7
1.2.2 Microstructure of FSW Al Alloys .....	9
1.2.3 Dissimilar Friction Stir Welding of Al Alloys .....	10
1.2.4 Mechanical Properties of FSW Al Alloys: Joint Efficiency and Fatigue Life .....	11
1.2.5 Susceptibility of FSW of Al Alloys to Environmental Factors: Corrosion .....	12
1.3 Preface of Chapters .....	13
CHAPTER 2 MICROSTRUCTURE AND MECHANICAL PROPERTIES OF DISSIMILAR FRICTION STIR WELDING OF AA6061-TO-AA7050 ALUMINUM ALLOYS .....	15
2.1 Abstract .....	15
2.2 Introduction .....	16

2.3	Materials and Methods.....	17
2.4	Results and Discussion.....	20
2.5	Summary and Conclusions.....	29
CHAPTER 3 LOW CYCLE FATIGUE OF DISSIMILAR FRICTION STIR WELDING OF AA6061-TO-AA7050 ALUMINUM ALLOYS.....		30
3.1	Abstract.....	30
3.2	Introduction.....	31
3.2.1	Low Cycle Fatigue in Friction Stir Welding.....	31
3.3	Materials and Experiments.....	33
3.4	Results And Discussion.....	36
3.4.1	Microstructure.....	36
3.4.2	Tensile Testing.....	41
3.4.3	Cyclic Stress and Strain Response.....	44
3.4.4	Low Cycle Fatigue Parameters.....	46
3.4.5	Fractography.....	49
3.4.6	Multistage Fatigue Modeling.....	56
3.5	Summary and Conclusions.....	61
CHAPTER 4 CORROSION EFFECTS ON THE FATIGUE LIFE OF DISSIMILAR FRICTION STIR WELDING OF HIGH STRENGTH ALUMINUM ALLOYS.....		62
4.1	Abstract.....	62
4.2	Introduction.....	63
4.3	Materials and Experiments.....	65
4.4	Results and Discussion.....	69
4.4.1	As welded microstructure.....	69
4.4.2	Pre-corroded FSW.....	70

4.4.2.1 FSWed AA6061-to-AA7050 .....	70
4.4.2.2 FSWed AA6061-to-AA6061 .....	72
4.4.2.3 FSWed AA7050-to-AA7050 .....	74
4.4.3 Fatigue Testing of Pre-corroded FSW .....	76
4.4.3.1 Fatigue of FSWed AA6061-to-AA7050 .....	76
4.4.3.2 Fatigue of FSWed AA6061-to-AA6061 .....	82
4.4.3.3 FSWed AA7050-to-AA7050 .....	85
4.4.4 Remarks in the Corrosion Behavior of dissimilar FSWed AA6061-to-AA7050.....	89
4.4.5 Multistage Fatigue Modeling .....	90
4.5 Conclusions .....	96
CHAPTER 5 CONCLUSIONS AND RECOMMENDATIONS .....	98
REFERENCES .....	102
APPENDIX.....	112

## LIST OF TABLES

Table 2-1. Nominal composition and mechanical properties for AA6061-T6 and AA7050-T7451 plates.....	18
Table 3-1. Nominal composition and mechanical properties for AA6061-T6 and AA7050-T7451 plates.....	34
Table 3-2. Average grain size for different locations of the weld and various tool rotational speeds.....	39
Table 3-3. Summary of the monotonic tensile properties for the dissimilar FSW AA6061-to-AA7050 and the base materials. ....	42
Table 3-4. Summary of the low cycle fatigue properties for the dissimilar FSW AA6061-to-AA7050.....	49
Table 4-1. FSW process parameter and material configuration used for this study.....	65
Table 4-2. Fatigue tests data for the pre-corroded FSWed AA6061-to-AA7050.....	82
Table 4-3. Fatigue tests data for the pre-corroded FSWed AA6061-to-AA6061.....	85
Table 4-4. Fatigue tests data for the pre-corroded FSWed AA7050-to-AA7050.....	88
Table 4-5. Summary of the low cycle fatigue properties for the dissimilar FSWed AA6061-to-AA7050, AA6061-to-AA6061 and AA7050-to-AA7050.....	94
Table 7-1. Dissimilar FSW of Al alloys. ....	112
Table 7-2. Fatigue life performance: Similar and dissimilar FSW Al alloys. ....	118
Table 7-3. Corrosion: Similar and dissimilar FSW of Al alloys.....	123
Table 7-4. Microstructure-sensitive fatigue modeling parameters for dissimilar FSWed AA6061-to-AA7050. ....	128
Table 7-5. Microstructure-sensitive fatigue modeling parameters for FSWed AA6061-to-AA6061 (460 rpm-205.4 mm/min).....	129
Table 7-6. Microstructure-sensitive fatigue modeling parameters for FSWed AA7050-to-AA7050 (360 rpm-152.4 mm/min).....	130

## LIST OF FIGURES

Figure 1-1. AM-2 aluminum matting for temporary airfield applications (Adapted from [19,20]).....	4
Figure 1-2. Schematic showing the basic principles of Friction Stir Welding [24].....	6
Figure 1-3. Weldability of various aluminum alloys [36]. .....	9
Figure 1-4. Cross-section of FSWed of AA7075-to-AA7075 Al alloy. The characteristic features of the weld such as the TMAZ for both the advancing (AS) and retreating side (RS), the HAZ, the SZ and void defects in the nugget section can be observed.....	10
Figure 2-1. Schematic representation of the dissimilar AA6061-AA7050 FSW. The welds were carried out parallel to the rolling direction of the plates, and by placing the AA7050 alloy on the advancing side. Tensile test coupons were cut perpendicular to the welding direction. ....	19
Figure 2-2. Transverse sections of the joints produced by dissimilar AA6061-AA7050 FSW, at different tool rotational speeds.....	21
Figure 2-3. SEM-backscattered electron image showing the three distinct layers of material found in the SZ and their respective chemical composition. ....	22
Figure 2-4. Transverse section of the dissimilar AA6061-AA7050 FSW, showing magnified optical images of different locations within the weld. ....	23
Figure 2-5. (a) Vickers microhardness profile for the dissimilar AA6061-7050 FSW, under different tool speeds. The left side corresponds to the AA6061 whereas the right side corresponds to the AA7050. (b) Summary of the tensile properties for the AA6061-AA7050 FSW, under different tool rotational speeds. ....	25
Figure 2-6. (a) OM micrograph showing the transverse section of the fractured samples showing the fracture location in the AA6061 alloy. (b) Typical SEM micrographs of the fractured surfaces for the AA6061-AA7050 FSW processed at 270 rpm. (c) Magnified SEM image of the welding defect (void). (d) SEM image of the fractured surface and a magnified view (e), showing the distribution of the deformation dimples found in the current sample. ....	27
Figure 3-1. Schematic representation of the dissimilar AA6061-AA7050 FSW. The welds were carried out parallel to the rolling direction of the plates, and by placing the AA7050 alloy on the advancing side. Fatigue test coupons were cut perpendicular to the welding direction. ....	35

Figure 3-2. (a) Top (crown), (b) cross-section and (c) bottom (root) surface for the dissimilar FSW of AA6061-to-AA7050, processed at 410 RPM. (d) Microhardness profiles obtained from the center of the cross-sections of the dissimilar FSW at various tool rotational speeds. ....	37
Figure 3-3. Optical micrographs showing the microstructure at different locations of the (a-d) cross section of the weld and (e-f) the base materials. ....	40
Figure 3-4. SEM backscatter micrograph showing the location of the secondary intermetallic parties located in the TMAZ corresponding to the (a) AA6061 and the (b) AA7050, and the (C) SZ. This micrographs were obtained form the top view of the weld. ....	41
Figure 3-5. Experimental data for the low–cycle fatigue life for the dissimilar FSW AA6061-to-AA7050 for various tool rotational speeds, and the low cycle fatigue data for the AA6061-T6 base material [30], FSW AA6061-T6 (600 rpm-200 mm/min) [30], and the FSW 2219 (300 rpm- 100 mm/min) [78] adopted from various studies.....	43
Figure 3-6. (a) Stress amplitude and (b) plastic strain amplitude versus the number of cycles to failure for various strain amplitudes and tool rotational speeds. Hysteresis loops for (c) 0.4% and (d) 0.2% strain amplitude for a tool rotational speed of 410 rpm. ....	45
Figure 3-7. (a) Monotonic and cyclic stress strain curves for the dissimilar FSW of AA6061 and AA7050 Al alloys produced at a tool rotational speeds of 410 rpm. (b) Cyclic strength coefficient and cycle strength exponent as a function of the tool rotational speed. ....	46
Figure 3-8. Typical optical micrographs showing the failure locations at various strain amplitudes the dissimilar FSW 6061-to-7050 Al alloys. (a) Welds produced at (a) 270 rpm and (b) 410 rpm.....	51
Figure 3-9. Optical micrographs showing the fracture surfaces for the welds processed at 270 RPM (a-b) and 410 (c-d) and tested under cyclic loading at 0.2 % (a-c) and 0.4% 9b-d) strain amplitude.....	53
Figure 3-10. (a) Typical fracture surface for the weld produced at a tool rational speed of 410 rpm and tested at 0.2% strain amplitude. (b) Magnified images of a crack initiation site on the bottom surface (Region I). (C) Backscatter electron image of showing the morphology of the fractured second particles in Region II. (d) Magnified image of Region III, showing the striations observed in the stable crack propagation region. ....	54
Figure 3-11. (a) Typical fracture surface for the weld produced at a tool rational speed of 410 rpm and tested at 0.4% strain amplitude. (b-c) Magnified images of a crack initiation site on the top surface (region I). (c) Backscatter electron image of the crack initiation site at Region I showing the secondary particles and crack initiating from them. The secondary intermetallic particles at the crack inanition site are identified with the white arrows.....	55
Figure 3-12. MSF model fit for the dissimilar FSW of AA6061-to-AA7050 at a tool rotational speed of (a-b) 410 rpm. (b) The upper bound and lower bounds were obtained using the maximum (16.7 $\mu\text{m}$ ) and minimum (1.1 $\mu\text{m}$ ) particle diameters measured in the failure	

location (TMAZ/HAZ) of the AA6061 side. (c) Comparison of the MSF fit obtained between two rotational speeds (270 and 410 rpm).....	59
Figure 4-1. Optical micrograph showing the typical crown (top) surface and the cross-sections for the FSWed (a) AA6061-to-AA7050 (b) AA6061-to-AA6061 and (c) AA7050-to-AA7050..	67
Figure 4-2. Schematic representation of the sample preparation for the pre-corroded fatigue test.....	68
Figure 4-3. SEM backscatter micrograph showing the location of the secondary intermetallic parties located in the TMAZ corresponding to the (a) AA6061 and the (b) AA7050. This micrographs were obtained from the crown surface of the weld.....	70
Figure 4-4. (a) Corrosion damage produced in the FSWed AA6061-to-AA7050 after 30 days of static immersion in 3.5% NaCl aqueous solution. (b) Pitting damage in the AA6061 side. (c) Severe corrosion damage extending from the beginning of the TMAZ towards to base AA7050 base material.....	71
Figure 4-5. (a) Cross-section showing the corrosion pits observed in the AA6061 side and (b) the severe corrosion damaged observed in the AA7050 side. Magnified SEM micrograph showing the corrosion damage on the (c) AA6061 and in the (d) AA7050 side.....	73
Figure 4-6. (a) Corrosion damage produced in FSWed AA6061-to-AA6061 Al alloy after 30 days of static immersion in 3.5% NaCl aqueous solution. (b) Cross section showing the severe corrosion damage observed in the advancing side.....	74
Figure 4-7. (a) Corrosion damage produced in FSWed AA7050-to-AA7050 after 30 days of static immersion in 3.5% NaCl aqueous solution. (b) Cross-section showing the severe corrosion damage observed in the advancing side.....	75
Figure 4-8. Fatigue life results for the FSWed (a) AA6061-to-AA7050 (b) AA6061-to-AA6061 and (c) AA7050-to-AA7050 in the as-welded and pre-corroded condition for various exposure times. ....	77
Figure 4-9. Typical optical micrographs showing the failure locations at various strain amplitudes for the pre-corroded FSWed 6061-to-7050. (a) Top surface of the welds. (b) Surfaces parallel to the cross-section of the welds. ....	78
Figure 4-10. (a) Plastic strain amplitude versus the number of cycles to failure for various strain amplitude condition and tool rotational speeds (welding parameters). Hysteresis loops for (b) 0.2% strain amplitude. All the results are for sample sin the “as-welded” condition. ....	79
Figure 4-11. Typical fracture surfaces of the pre-corroded FSWed AA6061-to-AA7050 for the samples tested at (a-b) 0.3% and (c-d) 0.2% strain amplitude. (b) The white arrow indicates the crack initiation site at a corrosion pit of a sample tested at 0.3% strain amplitude. This sample failed at the AA6061 Al side. (d) At 0.2% strain amplitude, the crack initiated (Region I) from the severe corrosion attack (region II) generated after 30 days of static immersion in 3.5% NaCl.....	81

Figure 4-12. Typical optical micrographs showing the failure locations at various strain amplitudes for the pre-corroded FSWed AA6061-toAA6061. (a) Top surface of the welds. (b) Surfaces parallel to the cross-section of the welds. ....83

Figure 4-13. Fracture surface of the pre-corroded FSWed AA6061-toAA6061 samples tested at 0.2% strain amplitude and 30 days of static immersion in 3.5% NaCl. (a) Overview of the fracture surface. (b-c) Magnified view of the corrosion pits in the crown surface of the weld. (d) Typical striations on the fracture surface of the weld. ....84

Figure 4-14. Typical optical micrographs showing the failure locations at various strain amplitudes for the pre-corroded FSWed AA705-to-AA7050. (a) Top surface of the welds. (b) Surfaces parallel to the cross-section of the welds. ....87

Figure 4-15. (a) Typical fracture surface of the pre-corroded FSWed AA7050-to-AA7050 for the samples tested at 0.2% strain amplitude after static immersion in 3.5% NaCl for 30 days. (b) Magnified view of the crack initiation at corrosion defects (region I). (c) Magnified view of the stable crack propagation (region II). (d) Magnified view of region II showing the striations. ....87

Figure 4-16. MSF model fit for the fatigue life prediction after corrosion attack for the FSWed (a) AA6061-to-AA7050, (b) AA6061-to-AA6061 and (c) AA7050-to-AA7050. ....93

Figure 7-1. Design of the FSW used for the samples preparation of this study. ....131

## CHAPTER 1 INTRODUCTION

Due to their high strength-to-weight ratio, good machinability, and high resistance to corrosion, aluminum alloys are ideal as structural materials. Among the most widely used and advanced high strength aluminum alloys, there are the heat treatable AA6061 and AA7050. Both alloys have been extensively employed in for structural applications in the automotive, marine and aerospace and military applications. While, friction stir welding has been successfully demonstrated for the joining a similar aluminum alloys, particular interest have been established on the research and development of joining dissimilar metals by the same process. Therefore, the aim of this study is to investigate the achievable microstructural and mechanical properties of similar joining and dissimilarly joining of AA6061-to-AA7050 via FSW. As such, in this study the environmental effects on the microstructure and mechanical properties of similarly and dissimilar welded aluminum alloys are studied through pre-exposed corrosion. A comprehensive study of the effects of the welding process parameter and environmental effects on the microstructure and mechanical performance under static and cyclic loading similar and dissimilar friction stir welding of 6061 and 7050 Al alloys is presented.

### 1.1 Research Justification

The rapid deployment of troops and military equipment is pivotal for the success of US and allied forces during overseas military campaigns and other civil operations. For this reason, US military forces depend on portable, rapid deployment, and temporary airfield technology.

Also known as Expeditionary Airfields (EAFs), these temporary airfields are meant to be constructed, used, broken down and moved to another site for re-use [1], requiring minimum use of heavy machinery for their deployment. The temporary airfield technology has been under development and use since the critical campaigns during the World War II. Initially made using steel panels, the landing matting known as the PSP (pierced steel plank) was extensively used by the front line construction personnel to build temporary runways over all type of terrains, becoming a critical element for the military operations success [2]. However, with the beginning of the jet aircraft era, and the exposure of harsh and high temperature associate with marine site and deserts, the PSP could not withstand the extreme corrosive environment requiring the development of a different landing mat technology. Therefore, due to its lightweight, high strength and high corrosion resistance properties, the US military forces decided to adopt aluminum alloys as the material for future designs.

Adopted by the Air Force in 1965, one of the designs that still in use is the AM-2 Aluminum Matting (Figure 1-1). This airfield mat consists of 366x61x3.8 cm panels made of hollow aluminum extrusions of AA6061-T6 [3–5], weighting about 65 kg (144 lbs) each. Each extruded panel has a set of connectors which allows the connection with the neighbor panels until the desired runway size is assembled. This design allows the taxiway panel to be installed and interlock with a rotating motion [6], requiring no heavy machinery. The mats interlock with each other to form a brickwork matrix that provides the necessary strength for the support of the aircraft and other heavy machinery on top of it.

Typically, the service life of the airfield matting has been limited by the failure of the end-cap interlock connectors used for the assembly of the individual panels. Currently, the end-

cap connectors are welded using convectional fusion welding techniques. Although the AA6061 alloy can be joined by conventional fusion welding, the excess heat results in the dissolution of its  $Mg_2Si$  precipitates causing severe material softening and a decrease on the mechanical performance of the alloy [7]. On the other hand, there is the recently developed friction stir welding (FSW) [8–12], which is a solid welding technique that has been successfully used for the joining of aluminum alloys. The friction stir welding takes place in the solid state of the material and eliminates the issues associated to resolidification, the formation of second phases, porosity, embrittlement and material softening due to excess heat, which are typically associated with fusion welding [13–17]. Furthermore, FSW have been demonstrated for the joining of a wide range of aluminum alloys, including higher strength aluminum that are considered unweldable such as the 2XXX and 7XXX series [18]. In addition it has been demonstrated for the joining of dissimilar alloys, eliminating the issues associated with the compatibility of the filler material which is typical of conventional fusion welding. This allows the development of next generation airfield matting by combining higher strength materials such as the AA7050 Al alloy in the sections requiring higher fatigue resistance such as the end-cap connectors segments.



**Figure 1-1. AM-2 aluminum matting for temporary airfield applications (Adapted from [19,20]).**

Currently, the US ARMY Corps of Engineering is developing the next generation of airfield matting for military applications. The aim is to improve the service life of the AM-2 design by incorporating FSW to their design, and by combining the use of low cost and high strength aluminum alloys such as the AA6061 and AA7050. To the best of the author's knowledge, the dissimilar joining of AA6061-to-AA7050 Al alloys has not been investigated. Therefore, the aim of this study is to investigate the achievable microstructural and mechanical properties of joining dissimilarly joining of AA6061-to-AA7050 via FSW. As such, in this study the environmental effects on the microstructure and mechanical properties of friction stir welded aluminum alloys are studied through pre-exposed corrosion. A comprehensive study of the effects of the welding process parameter and environmental effects on the microstructure and mechanical performance under static and cyclic loading similar and dissimilar friction stir welding of AA6061 and AA7050 Al alloys is presented.

## 1.2 Friction Stir Welding

Friction stir welding (FSW) has become of high interest to multiple industries due to its many advantages as a suitable technology for joining of lightweight metals. Invented in 1991 by The Welding Institute (TWI) in UK, this process takes place on solid-state temperatures, eliminating issues associated with the formation of secondary and brittle phases, cracking during solidification, and high distortion and residual stress typically associated with conventional fusion welding [13–17]. As shown in Figure 1-2, the process comprises a non-consumable rotating tool, consisting of pin probe and a shoulder, which are plunged into the workpiece, generating heat from the resulting friction and plastic deformation [13]. The localized heating softens the material in direct interaction with the tool, allowing the movement of the material around the pin, and as a result, the joint is produced in a solid state [21].

Multiple metallurgical, environmental and energy benefits are associated with FSW. Among the metallurgical benefits there is the resulting low distortion of the workpieces, good dimensional stability, excellent mechanical properties in the weld and the absence of cracking associated with solidification. This process requires no shielding gas, minimal surface preparation, and eliminates the grinding wastes produced when using fusion welding. Also, this process allows the joining of multiple material thickness, multiple joint configurations (square-butt, T-butt, lap-joint, and fillet) and only requires about 2.5% of the energy needed for laser welding, making FSW an environmentally friendly technology [21]. Furthermore, the FSW allows the joining of dissimilar materials, eliminating the undesirable weight and stress concentration associated with the use fasteners and rivets [22,23], which is the main focus of this investigation.

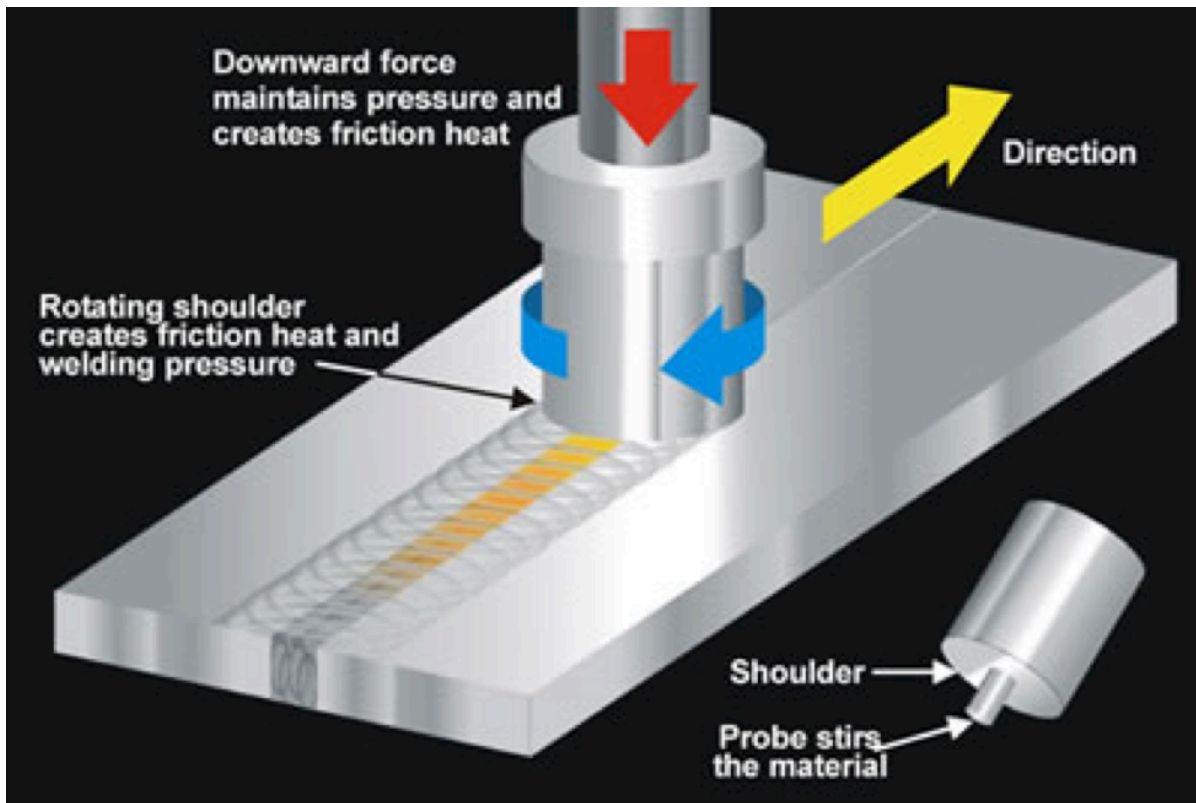


**Figure 1-2. Schematic showing the basic principles of Fiction Stir Welding [24].**

The quality and joint strength of the weld are strongly influenced by the microstructure development, which at the same time is dependent on the process parameters such as the tool design, tool tilt angle, and the tool rotational and transverse speed. The tool design is one of the most important process parameters and one of the areas of major research in the FSW community. The selected tool must provide the appropriate material mixing, heat generation, while maintaining the flash generation at a minimum and must have a high wear resistance. Among the most common tool designs are the cylindrical pin, threaded cylindrical, threaded with flats, and conical designs. On the other hand, the generated peak temperatures are significantly influenced by the tool rotational and transverse speeds, which have a direct effect on

microstructural development. Increasing the tool rotational speed leads to an increase in the peak temperature while increasing the transverse speed will lead to a slight decrease in the peak temperatures [25]. The inappropriate selection of these process parameters can lead to the formation of welding defects such as the formation of channel like voids, excess flash or significant material softening due the excessive heat.

Due to its numerous benefits, the application of FSW technology extends to multiples industries such as the aerospace, automotive, naval and electronics. For example, the need for the implementation of super lightweight aluminum alloys drove NASA to the development and application of FSW for the fabrication of the external fuel tank for the Space shuttle missions. In addition, NASA is currently using it for the fabrication of the new Space Launch System (SLS). FSW has also been used in the private space sector such as the United Launch Alliance (ULA) and most recently Space X, and as a replacement of rivet and fastener joining technology in aircrafts. On the other hand, the need for light weight materials, such as aluminum and magnesium alloys, have pushed the automotive industry to the implementation of FSW and its variant, the friction stir spot welding (FSSW). Most recently, FSW was implemented in the electronics industry by the introduction of the 2013 iMac computer from Apple Inc., where the aluminum body of its display was welded using this technology.

### 1.2.1 High Strength Aluminum Alloys

Due to their high strength-to-weight ratio, good machinability, and high resistance to corrosion, aluminum alloys are ideal as structural materials [26]. Among the most widely used and advanced aluminum alloys, there are the heat treatable 6XXX Al-Mg-Si and 7XXX Al-Mg-

Zn systems [26]. The AA6061 class have been extensively employed in marine frames, pipelines, storage tanks and aircraft application [7]. On the other hand there is the AA7050 alloy which is mostly used on the aerospace industry and is known to have an improved toughness and corrosion resistance when compared to other alloys from 7XXX series [22]. The strengthening of these alloys is achieved by producing hard nanosized precipitates via solution heat treatment, and subsequent artificial aging and quenching [27]. For the case of the AA6061, strengthening is achieved by the formation of  $Mg_2Si$  [8], whereas the AA7050 is done by the formation of  $Mg_2Zn$  precipitates [28,29]. The improvements in the mechanical properties (i.e. yield strength and strain hardening rate) are produced due to the presence of the nanosized precipitates, which serve as obstacle for the movement of dislocations [30]. Although the AA6061 alloy can be joined by conventional fusion welding, the excess heat results in the dissolution of its  $Mg_2Si$  precipitates, and therefore, in severe material softening and a decrease on the mechanical performance of the alloy [7]. Conversely, multiple studies have been conducted that demonstrated the effectiveness of FSW for the joining of this alloy [8–12]. On the other hand, the AA7050 alloy is considered to be “unweldable” by conventional fusion techniques [29], however, sound and reliable joints have been successfully produced by FSW [23,31–34] (Figure 1-3). While these alloys have been demonstrated to be welded by FSW, both alloys are still susceptible to thermal history, since the precipitates can dissolve and coarsened due the excess heat produced by the rotation FSW tool, which results in a decrease on the mechanical strength of the joint and adjacent base material [21,35].

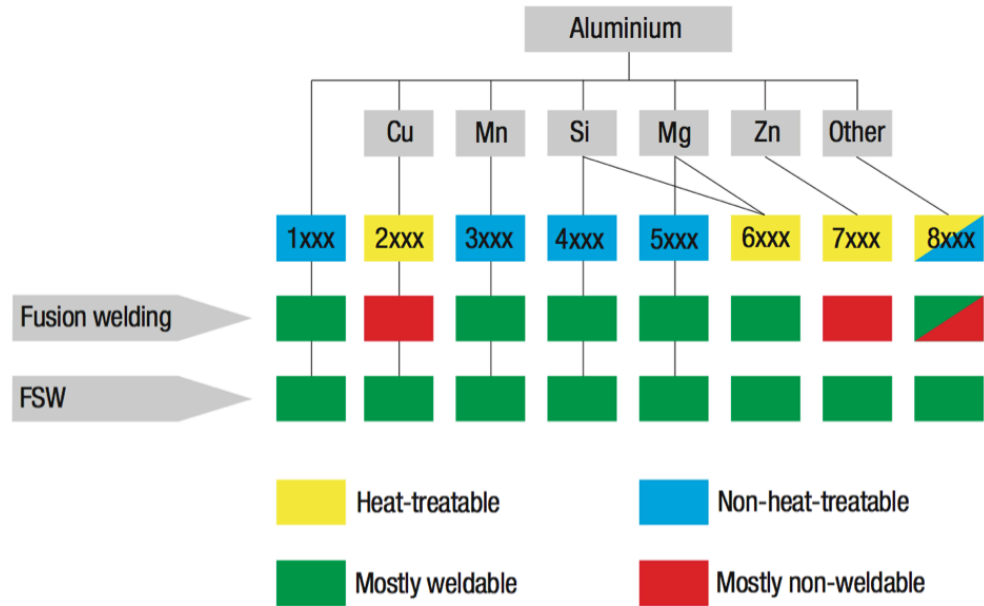


**Figure 1-3. Weldability of various aluminum alloys [36].**

### 1.2.2 Microstructure of FSW Al Alloys

The FSW on aluminum alloys is characterized by the formation of distinct microstructure in the nugget region and adjacent zones. Some of the mentioned characteristics features are shown in Figure 1-4. These characteristic features are the nugget or stir zone (SZ), the thermo-mechanically affected zone (TMAZ), the heat affected zone (HAZ), and the base material (BM). The stir zone is characterized by very fine dynamically recrystallized microstructure when compared to parent metal [25]. This microstructure results from the intense heat and severe plastic deformation produced from the direct interaction with the rotating pin. Adjacent to the SZ there is the TMAZ, which consists of the material that experienced less mechanical deformation when compared to the nugget region. This region is characterized by the grain distortion produced from the shearing load and flow of extruded material coming from the nugget. Next to

the TMAZ there is the HAZ, which compromises the material that has not experienced any mechanical deformation, but experienced microstructural changes due to the dissipated heat coming from the center of the weld. The HAZ retains the same grain morphology as the parent material, however, it experiences temperatures as high as 250°C, which exerts significant changes on the precipitates structures of the material, leading to a decrease in strength and further joint failure.



**Figure 1-4. Cross-section of FSWed of AA7075-to-AA7075 Al alloy. The characteristic features of the weld such as the TMAZ for both the advancing (AS) and retreating side (RS), the HAZ, the SZ and void defects in the nugget section can be observed.**

### 1.2.3 Dissimilar Friction Stir Welding of Al Alloys

While FSW has been successfully demonstrated for the joining a similar aluminum alloys, particular interest have been established on the research and development of joining dissimilar metals by the same process [37]. For example, Lee et al. [38] studied the microstructure and tensile properties of A356/AA6061 Al dissimilar FS welds. Murr et al. [39] studied the microstructure and vortex formation on the friction stir welding of dissimilar joints (AA6061/Cu and AA2024/AA6061). Also, other dissimilar aluminum based FSW joints were investigated such as AA2024/AA7075 Al [40], the AA5083-H111/AA6351-T6 [41] and the

5083/6061 Al [42]. In all of these studies, material intermixing was evident by the formation of complex and intercalated vortices, also known as “onion rings” [37], which are strongly related to the material flow during the welding process. This complex, intercalated flow directly affects the microstructure formation and therefore the mechanical properties of the welds. Recently, Guo et al. [43] studied the microstructure and the monotonic strength of dissimilar FSW between AA6061 and AA7075. In their study, they evaluated the effects of the material position and welding speed on the material flow on tensile properties, demonstrating that material mixing was more effective when the relatively softer alloy was located on the advancing side, and revealing that all joints failed at the heat-affected zone (HAZ) of the softer material (AA6061) regardless of their position with respect to the welding (advancing or retreating side). Table 7-1 in the appendix presents other relevant studies on dissimilar FSW.

#### 1.2.4 Mechanical Properties of FSW Al Alloys: Joint Efficiency and Fatigue Life

Understanding the static and fatigue properties of friction stir welded materials is critical for safe designs. Multiple studies on the mechanical properties of friction stir welded Al alloys have reported joint strengths in many cases as high as the strengths of the parent materials. For the case of the AA6061 and AA7050 alloys, joint efficiencies as high as 79% and 81% have been reported [21]. Regarding fracture, most of the failure has been observed to occur due to excess softening occurred in the TMAZ and HAZ zones. For the case of the dissimilar welds, in all cases failure occurred through TMAZ and HAZ of the material having the lowest strength.

In many applications these materials are meant to be used on structures under dynamic loading such as in such as the aerospace structures, transport vehicles, bridges, etc., therefore, understanding the material properties under dynamic loading is critical. Regarding fatigue life

behavior, several investigations have been conducted on the FSW joints of multiple aluminum alloys. Among the most relevant there are FSW of AA6061-T651 [30], FSW of AA7075 [44] and FSW of AA7050 [32]. In general, these investigations revealed that the fatigue life of the welds at  $10^7$  cycles was much lower than that of the base materials. Despite this fact, the resulting fatigue strength of the FSW was higher when compared to the fusion welds, which is attributed to the significantly finer and uniform microstructure produced from the FSW process. For the case of the fatigue life of dissimilar FSW, very limited research can be found in literature. The following studies on dissimilar FSW were found in literature: AA6082/AA2024 Al [45], AA7075/AA6061 [46], AC4CH-T6/A6061-T6 [47] (Table 4). However, it is important to know that other alloy combinations such as the AA6061-AA7050 FS welds have not been investigated. Therefore, it is essential to study and to evaluate the effects of the process parameters on the microstructure and mechanical performance under static and cyclic loading of AA6061-AA7050 FSW dissimilar welds. Table 6-2 in the appendix presents other relevant studies on mechanical properties of FSW.

### 1.2.5 Susceptibility of FSW of Al Alloys to Environmental Factors: Corrosion

Depending on the particular application, the FSWed structure can be exposed to certain environmental factors that could have detrimental effects on the mechanical integrity of the joint. For example, the structure could be exposed to highly corrosive environments as in the case of marine applications.

Corrosion susceptibility of friction welded aluminum alloy for both similar and dissimilar welds have been studied before [48–54]. In general, studies have shown that friction stir welds are more susceptible to localized corrosion when compared to the parent material, due to the pitting

and intergranular corrosion introduced by the thermomechanical processing associated with FSW. Furthermore, for the case of high strength heat treatable alloys such as the 6XXX and 7XXX series, it is known that the precipitates play an important role in the corrosion resistance, therefore, it is expected that the precipitate development in the distinct region of the welds will affect its corrosion and mechanical performance. However, the corrosion effects on the mechanical properties, specifically on the dissimilar FSW of AA6061-to-AA7050 Al alloys, which is still unknown. A brief summary of corrosion susceptibility of FSW on aluminum alloys is presented in Table 6-3 in the Appendix.

### 1.3 Preface of Chapters

The overall objective of this research is to study the process effects on the static and fatigue properties of similar and dissimilar FSW of high strength aluminum alloys. This investigation comprises two main sections, Section I and Section II. The first section consists of Chapter 2 and 3 and is focused on the static and fatigue properties of dissimilar FSWed AA6061-to-AA7050 Al alloys. The second section consists of Chapter 4, which is focused on the effects of corrosion damage on the fatigue properties of dissimilar and similar FSW of high strength Al alloys.

Chapter 2 focuses on the dissimilar friction stir welding of two high strength aluminum alloys (AA6061 and AA7050). In this chapter, microstructure development and static mechanical properties of the FSWed AA6061-to-AA7050 are evaluated at three different tool rotational speeds. The static strength of the joint increased with the increase in the tool rotational speed, and was governed by the AA6061 alloy and by the degree of material intermixing. Furthermore,

to the author's knowledge, this was the first study to demonstrate the effectiveness of joining both materials (AA6061 and AA7050) by means of FSW.

Chapter 3 presents the results of an experimental and modeling study on the low cycle fatigue properties of the dissimilar FSWed AA6061-to-AA7050 Al alloys. In this chapter, the process effects on the fatigue life of the dissimilar butt joints were evaluated on fully reversed uniaxial loading. Fatigue results revealed an increase in the strain hardening properties as well as the fatigue life as the tool rotational speed was increased. Also, fracture analysis was performed to establish the failure modes of the joint. Furthermore, the microstructure sensitive multistage fatigue model was calibrated and extended for the prediction of the fatigue life of the dissimilar joint.

Chapter 4 is a study on the effects of corrosion defects on the low cycle fatigue performance of dissimilar and similar FSW of high strength aluminum alloys. In this chapter, three joints combinations were evaluated including dissimilar FSWed AA6061-to-AA7050, and similar FSWed AA6061-to-AA6061 and AA7050-to-7050. In this study, the low cycle fatigue properties of the different joint configurations were evaluated after been exposed too 3.5% NaCl for various exposure times. Results revealed localized corrosion damage in the thermo-mechanically affected and heat affected zones. Fatigue life decreased with the presence of corrosion defects, however, it was found to be nearly independent of the corrosion time. Lastly, the multistage fatigue model was extended by including the depth of the corrosion defects for the life prediction of the pre-corroded joints.

CHAPTER 2  
MICROSTRUCTURE AND MECHANICAL PROPERTIES OF DISSIMILAR FRICTION  
STIR WELDING OF AA6061-TO-AA7050 ALUMINUM ALLOYS

2.1 Abstract

In this work, the microstructure and mechanical properties of friction stir welded dissimilar butt joints of AA6061-to-AA7050 aluminum alloys were evaluated. Microstructure analysis of the cross-section of the joints revealed distinct lamellar bands and various degrees of intermixing that were correlated with tool rotational speed. Due to the distinct mechanical properties of the two alloys, microhardness measurements showed a consistent asymmetric hardness distribution profile across the weld nugget, regardless of tool rotational speed. Under monotonic tensile loading, an increase in the joint strength was observed with the increase in the tool rotational speed. Regarding fracture, all the joints failed on the AA6061 aluminum alloy side. Two modes of failure were observed, one through the stir zone and another through the heat-affected zone. Inspection of the fracture surfaces suggested that inadequate material intermixing produced at low tool rotational speeds, was the cause for the poor mechanical strength and failure through the stir zone. On the other hand the failure observed through the heat-affected zone at high rotational speeds was produced due to the material softening as confirmed by the microhardness measurements.

## 2.2 Introduction

Due to their high strength-to-weight ratio, good machinability, and high resistance to corrosion [26], aluminum alloys are an attractive lightweight metals for structural applications in the aerospace, automotive, and naval industry. However, the joining of Al alloys by convectional fusion welding techniques is known to be problematic [2], where some of these issues include the formation of secondary brittle phases, cracking during solidification, high distortion, and residual stresses [13].

Among aluminum alloys, the heat treatable 6XXX Al-Mg-Si and 7XXX Al-Mg-Zn systems [26] are some of the most widely advanced and used alloys. The AA6061 class have been extensively employed in marine frames, pipelines, storage tanks and aircrafts [7]. On the other hand, the AA7050 alloy is widely used in the aerospace industry and is known to have an improved toughness and corrosion resistance when compared to other alloys from 7XXX series [22]. The strengthening of these alloys is achieved by producing hard nanosized Mg-rich precipitates via solution heat treatment, and subsequent artificial aging [8,27–30]. Although the AA6061 alloy can be joined by conventional fusion welding, the AA7050 alloy is considered to be “unweldable” by these methods [29]. However, multiple studies have demonstrated the effectiveness of friction stir welding (FSW) for the joining of the AA6061 [8,10–12,55] and the AA7050 [23,31–33].

While FSW has been successfully demonstrated for joining similar aluminum alloys [56–59], particular interest have been established on the research and development of joining dissimilar metals [37,60]. Recent studies have been conducted in the dissimilar FSW of AA6061-to-AA7075 [43], AA2024-to-AA6061 Al alloys [39] and others [38–42,61], however,

to the best of the authors' knowledge, this is the first study to investigate the joining of AA6061-to-AA7050 aluminum alloy with FSW.

### 2.3 Materials and Methods

Butt friction stir welds were produced using 5 mm thick rolled plates of AA6061-T6 and AA7050-T7451. The nominal composition and mechanical properties for each material is summarized in Table 2-1. Three different tool rotational speeds were evaluated (270, 340, and 410 rpm), while the welding transverse speed was fixed to 114 mm/min. Similar parameter have been reported in literature [43,60,62–64]. A cylindrical threaded tool, having a pin and shoulder diameter of 10 mm and 18 mm respectively, was used for this study (Figure 6-1). The butt friction stir welding was performed parallel to the rolling direction of the plates, and by placing the AA7050-T7451 on the advancing side. After the welding was completed, the top and bottom surfaces of the welded plates were machined down to a 4 mm of thickness. This was done to eliminate the stress raisers produced due to the flash material at the top of the weld. Flash material is produced on top of the welded plates due to the direct interaction of the tool shoulder and the underneath material that is been extruded and stirred around the pin. Afterwards, specimens for microstructural and mechanical characterization were cut perpendicular to the welding direction by using a water jet cutting. A schematic representation of the preparation of the samples is presented in Figure 2-1. Microstructural characterization of the welds was carried out using optical (OM) and scanning electron microscopy (SEM), and energy dispersive x-ray spectrometry (EDS). The transverse and longitudinal sections of the welds were prepared using conventional metallographic techniques. All samples were etched for 60 seconds in a solution

consisting of 1g NaCl and 50mL H<sub>3</sub>PO<sub>4</sub> dissolved in 125mL of ethanol, followed by a 5 seconds step using Wecks's tint (4 g of KMnO<sub>4</sub> and 1 g of NaOH dissolved in 100 ml of distilled water). Vickers microhardness measurements were performed in the transverse cross section of the FSWed samples using 0.5 mm spacing, a load of 100 gf and a dwell time of 5 seconds.

**Table 2-1. Nominal composition and mechanical properties for AA6061-T6 and AA7050-T7451 plates.**

Material	Al	Si	Cu	Mg	Cr	Zn	UTS (MPa)	YS (MPa)	Elongation (%)
AA6061-T6	Bal.	0.6	0.3	1.0	0.2	-	310	275	15
AA7050-T7451	Bal.	-	2.3	2.2	-	6.2	524	469	11

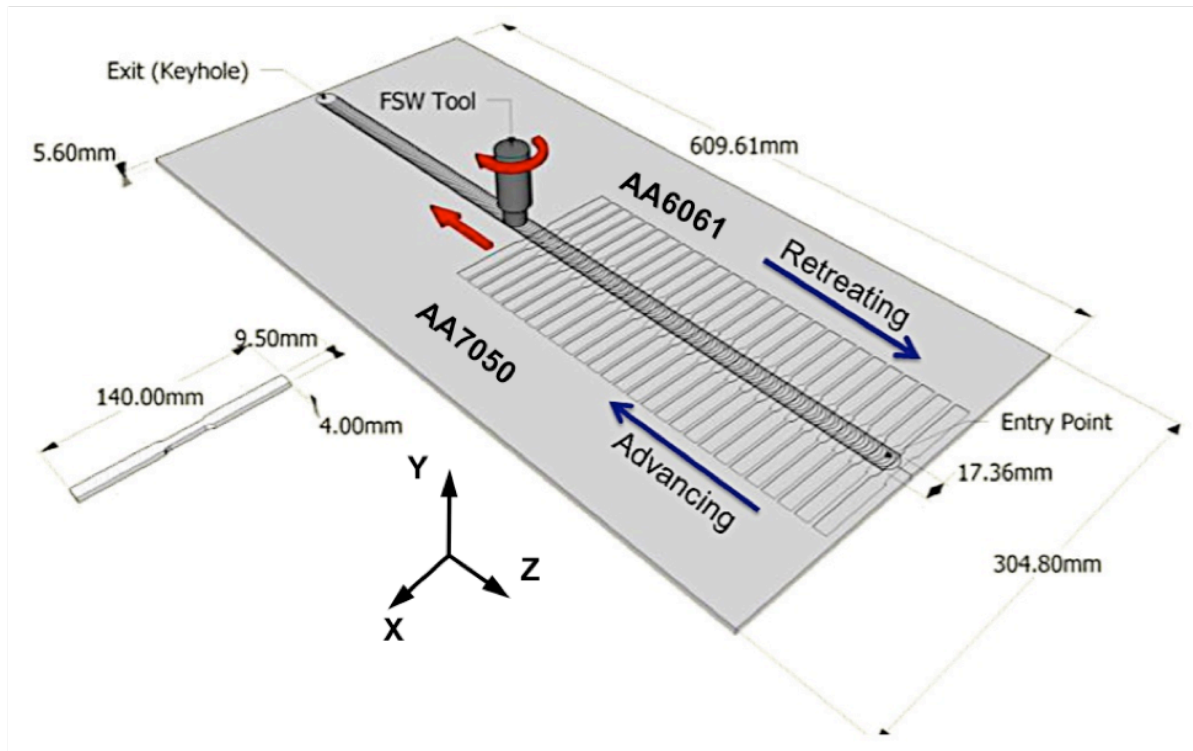


**Figure 2-1. Schematic representation of the dissimilar AA6061-AA7050 FSW. The welds were carried out parallel to the rolling direction of the plates, and by placing the AA7050 alloy on the advancing side. Tensile test coupons were cut perpendicular to the welding direction.**

To characterize the mechanical properties of the welds, monotonic tensile testing was performed on the FSWed coupons at room temperature using hydraulic mechanical tensile load frame. The testing was performed in displacement control mode at a rate of 1 mm/min using a 25.4 mm extensometer. Samples were prepared following the ASTM E8, having a width of 6 mm and a gage length of 50.8 mm, the overall dimensions of the samples are specified on Figure 2-1. A total of 9 samples, 3 per condition, were tested.

## 2.4 Results and Discussion

The transverse (X-Y) sections of the joints produced at different tool rotational speeds are shown on Figure 2-2. As stated earlier, the AA7050 was positioned on the advancing side (right hand side), while the AA6061 was placed on the opposite or rather the retreating side. Due to the differences in etching responses, AA6061 is shown as the bright colored regions, whereas the AA7050 is shown as the dark colored regions. No void defects were noticeable from the traverse sections in any of the tested parameters. Three main regions can be distinguished on the transverse sections, corresponding to the stir zone (SZ), the thermo mechanical affected zone (TMAZ), and the heat affected zone (HAZ). The SZ features vortex structures, that consists of alternate lamella of material corresponding to the base alloys and a mixture of both. Further examination using EDS confirmed the presence of three (3) distinct layers (Figure 2-3). Locations A and B consisted of the nominal composition for the AA6061 and AA7050 respectively, while location C consisted of a combination of both materials. Similar results have been demonstrated on dissimilar AA6061-AA7075 FSW [43]. The formation of the bands corresponding to the composition of Location C, have been attributed to the plasticized material constrained in the features associated with the tool geometry. As such, a fraction of the material is trapped in the features of the tool and subjected to extended deformation periods, allowing the material to be intermixed before being deposited in the SZ.

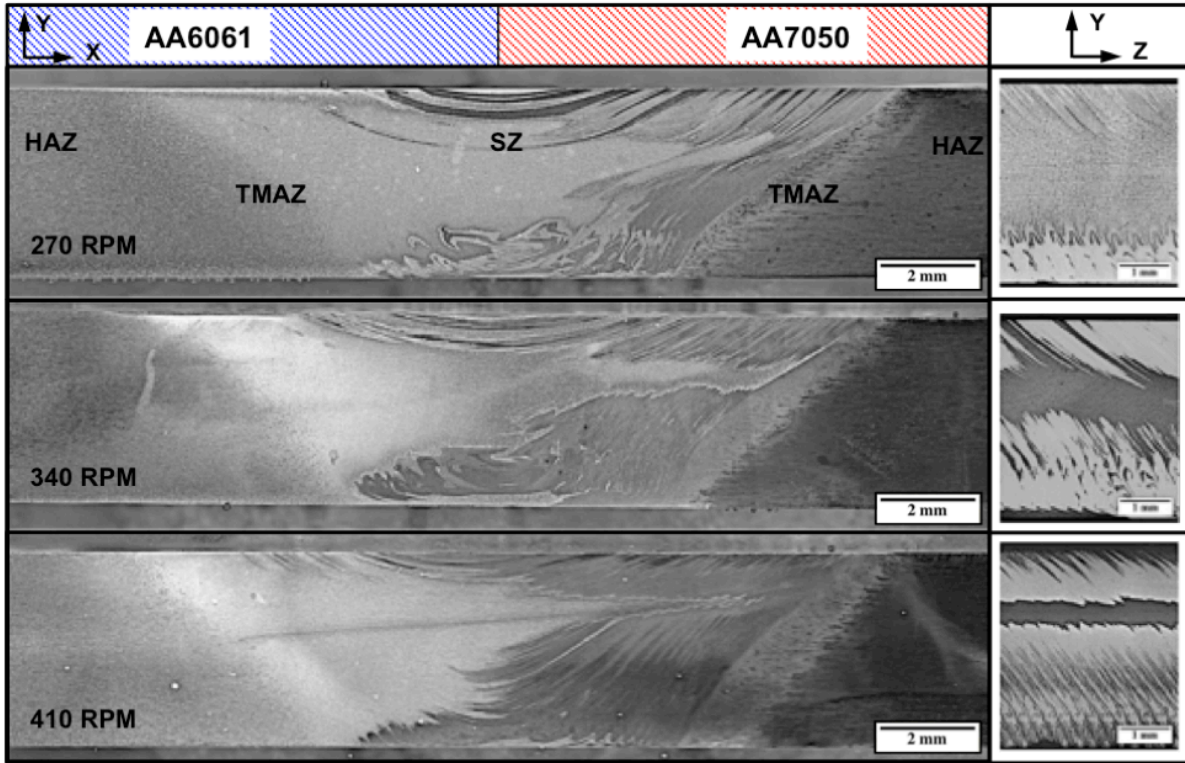


**Figure 2-2. Transverse sections of the joints produced by dissimilar AA6061-AA7050 FSW, at different tool rotational speeds.**

The formation of vortex structures or “onion rings” is typical of FSW, but is exaggerated in the welding of dissimilar metals [37]. These lamellar structures are attributed to the stirring action of the threaded tool, the in-situ extrusion, and to the transverse motion in the welding direction [60]. In fact, the thickness of the bands of unmixed material was also modified as the tool rotational speed was increased in the dissimilar welding of AA6061-to-AA7050. Microstructural examination of the longitudinal sections revealed that the spacing between the material bands decreased with the increasing tool rotational speed. Average values for the material bands interspacing of 460, 350 and 300  $\mu\text{m}$  were obtained for a tool speed of 270, 340

and 410 rpm respectively. This implies that a more uniform mechanical mixing was achieved at higher tool rotational speeds.

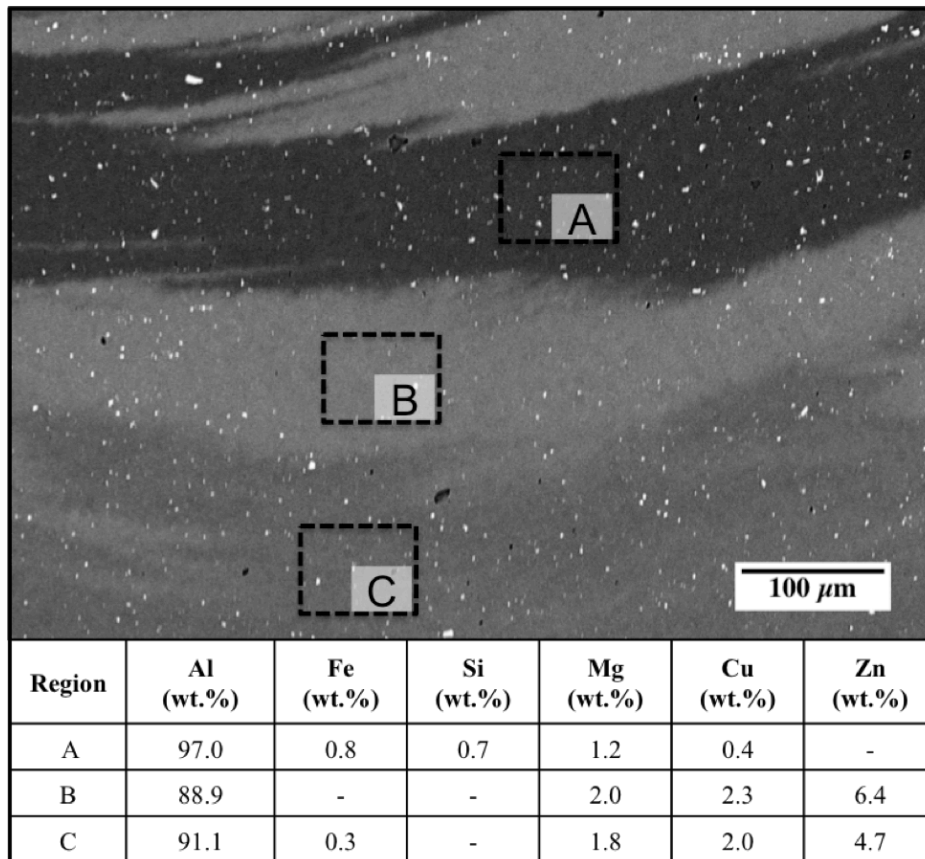


**Figure 2-3. SEM-backscattered electron image showing the three distinct layers of material found in the SZ and their respective chemical composition.**

For the current study, the aim was to demonstrate the effectiveness of FSW on the joining of AA6061 to AA7050, therefore, the location of the materials with respect to the tool rotation was not investigated. While not the aim of this study, several studies on FSW of dissimilar alloys have demonstrated the effect of the location of the materials with respect to the tool rotation. For example, for the FSW of AA6061-to-AA7075, Guo et al. [43] reported that a more effective

material mixing was achieved when the softer material, for instance the AA6061, was located in the advancing side. They reported that when placing the material with the highest strength (AA7075) on the advancing side, the developed high flow stresses, caused by the harder material, prevented the AA6061 from penetrating into the SZ. They also reported that higher ultimate tensile strengths were obtained by placing the AA6061 on the advancing side. Similar results have been reported on other dissimilar FSW studies for Al alloys [18,38]. For the case of the FSW of AA6061-to-AA7050, the effect of the location of the welded material with respect to the tool rotation and transverse speed will be considered in future studies.

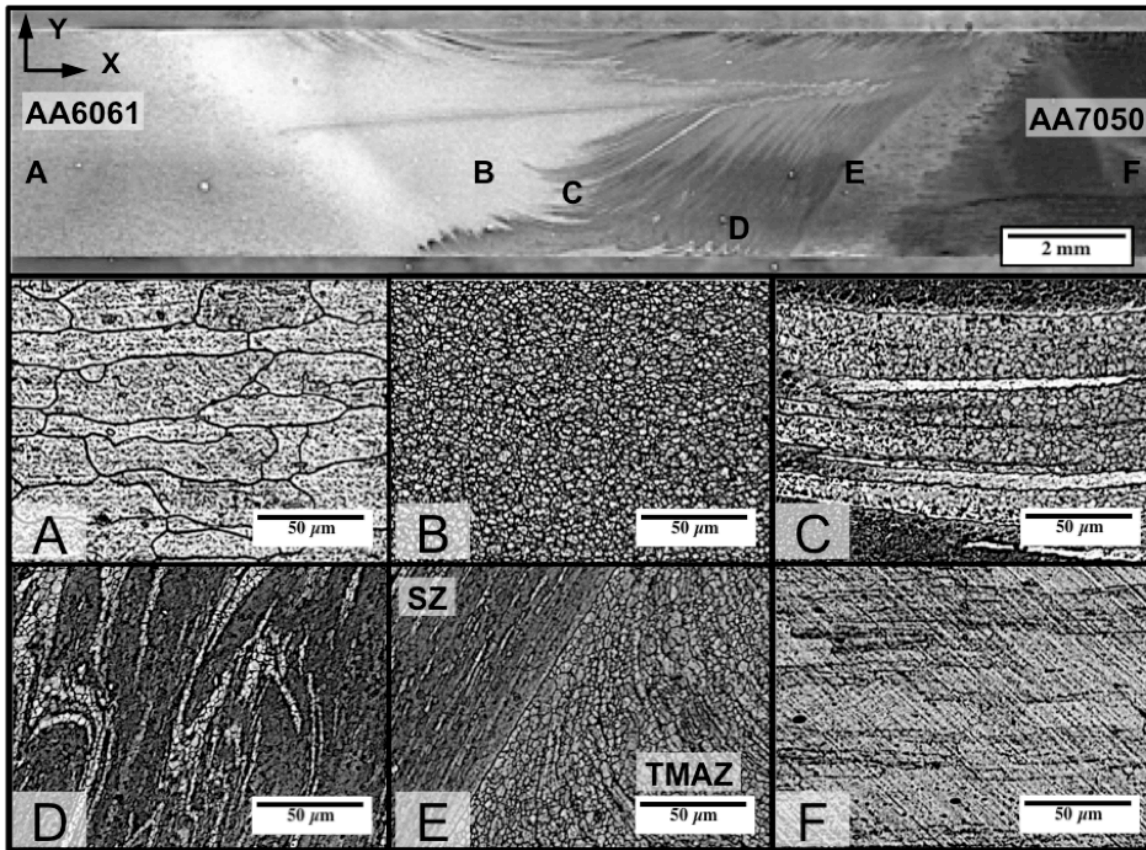


**Figure 2-4. Transverse section of the dissimilar AA6061-AA7050 FSW, showing magnified optical images of different locations within the weld.**

Figure 2-4 shows typical optical micrographs of the different regions on the transverse section of the AA6061-AA7050 welds. Location A and F correspond to the base materials of AA6061 and AA7050 Al alloys, respectively. Each of the base material comprises elongated grains,  $\sim 100$  and  $\sim 20$   $\mu\text{m}$  in the X and Y direction respectively. The AA6061 and the AA7050 base materials featured Al-Si-Fe and Al-Fe-Cu coarse intermetallic particles respectively, which were broken and modified from approximately from 10  $\mu\text{m}$  to 5  $\mu\text{m}$  in the SZ. Locations B, C, D, and E (Figure 2-4), show the distinct microstructure developed across the SZ, where the microstructures of both parent materials were significantly refined ( $< 7$   $\mu\text{m}$ ) due to the severe deformation and relatively high temperatures produced by the stirring action of the FSW tool. Location B (Figure 2-4) shows the microstructure developed in the SZ composed in its majority of the AA6061 alloy. Locations C and D (Figure 2-4) show magnified micrographs of the annular bands of the aforementioned mixed and unmixed materials. The formation of the significantly refined equiaxed microstructure in the SZ is known to be achieved via dynamic recrystallization (DRX)[31]. On the other hand, location E (Figure 2-4) shows the microstructure development in the boundary between the SZ and TMAZ, corresponding to the advancing side of the weld. Here the grains in the TMAZ flow upward toward the tool, thus creating a well defined boundary with the SZ. This region is characterized for grains undergoing plastic deformation but not recrystallization.

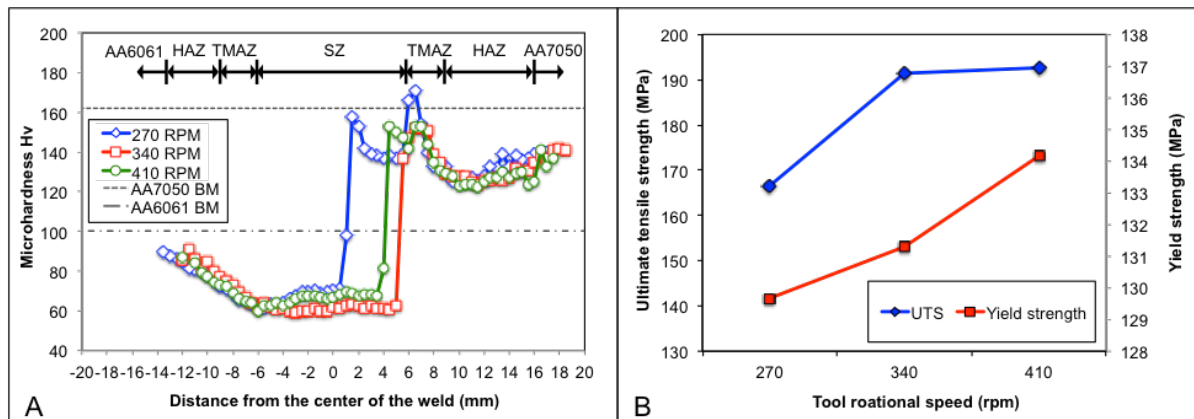


**Figure 2-5. (a) Vickers microhardness profile for the dissimilar AA6061-7050 FSW, under different tool speeds. The left side corresponds to the AA6061 whereas the right side corresponds to the AA7050. (b) Summary of the tensile properties for the AA6061-AA7050 FSW, under different tool rotational speeds.**

Vickers microhardness measurements were taken along the center of the transverse section of the welds (Figure 2-5a). Due to the distinct mechanical properties of the parent material, an asymmetric hardness distribution profile, which is typical of dissimilar friction stir welds, was obtained for all tested welding parameters. Hardness peak values were observed in SZ region adjacent to the advancing side, whereas low hardness regions were measured across the weld corresponding to the HAZ of both alloys and to the SZ adjacent to the retreating side. Since both alloys are precipitation hardenable via natural and artificial aging, they are susceptible to the thermal history produced during the welding process [25], which in fact explains the hardness variations measured across the weld. During the FSW process, high temperatures (ranging from 400 to 500 °C) [18] can be generated in the SZ. The temperature increase in the SZ and the excess heat dissipated into the surrounding material, produces a supersaturated solution

condition and a overaged condition at the SZ and surrounding material respectively. Precipitate dissolution into the matrix (supersaturate condition) at the SZ, and precipitate coarsening (overaging) at the HAZ, alters the strength of the material, which in fact result into the hardness profiles observed. In addition, natural aging at room temperature may have contributed to the hardness variations [32].

Figure 2-5b presents the results obtained from the monotonic tensile test performed on the dissimilar FSW of AA6061-to-AA7050. During monotonic tensile loading, all joints fractured through the AA6061 side of the joint. Similar results have been reported in other dissimilar FSW studies, where the joints failed either through the HAZ of the TMAZ of the material with the lowest strength [43,63,65,66]. In this study, experimental results demonstrated an apparent increase in the yield and the ultimate tensile strength of the joint as the tool rotational speed was increased. Yield strength values of  $129.7\pm 4.2$ ,  $131.3\pm 1.7$  and  $134.2\pm 0.9$  MPa were obtained for the tool rotational speed of 270, 340 and 410 rpm, respectively. The highest joint strength was obtained for the highest rotational speed (410 rpm), having an average ultimate tensile strength (UTS) of  $192.6\pm 1.5$  MPa. In addition, the results revealed an apparent decrease in the elongation as the tool rotational speed was increased, exhibiting average elongation values of  $8.2\pm 0.6$ ,  $8.0\pm 0.3$  and  $6.0\pm 0.6$  for a tool speed of 270, 340 and 410 rpm, respectively. However, the elastic modulus of the joint did not show significant differences between the welding parameters employed in this study. An average of  $69.7\pm 0.6$  GPa was measured for the elastic modulus, which represents a difference of less than 2% when compared to the elastic modulus of the AA6061 base material in the T6 condition.

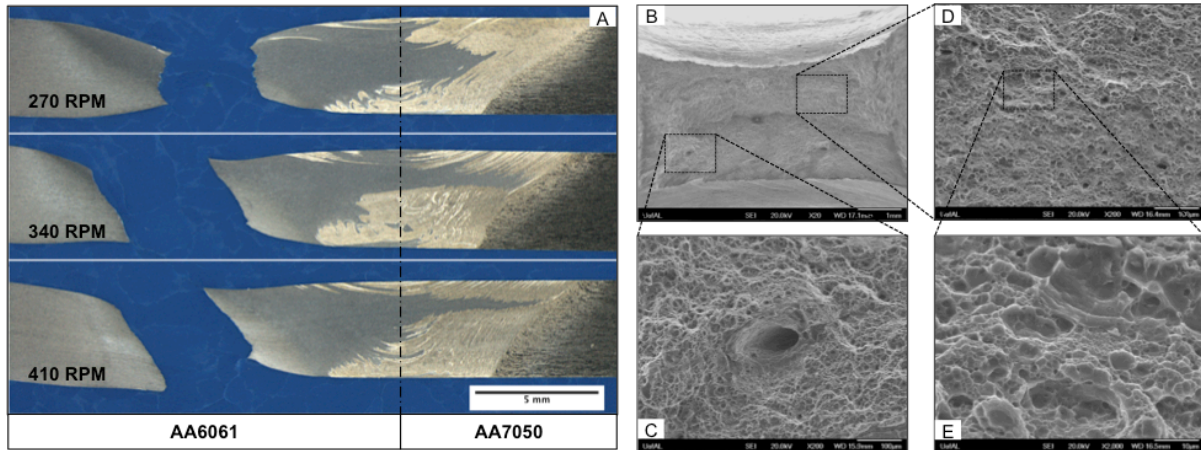


**Figure 2-6. (a) OM micrograph showing the transverse section of the fractured samples showing the fracture location in the AA6061 alloy. (b) Typical SEM micrographs of the fractured surfaces for the AA6061-AA7050 FSW processed at 270 rpm. (c) Magnified SEM image of the welding defect (void). (d) SEM image of the fractured surface and a magnified view (e), showing the distribution of the deformation dimples found in the current sample.**

Figure 2-6 shows the fractured surfaces after failure under monotonic tensile loading, it can be clearly seen that all the samples failed through the AA6601 side (Figure 2-6a), however, two failure modes were observed. The joints produced at the low rotational speed (270 RPM) demonstrated at crack propagating through the left end of the stir zone, in other words, the nugget region adjacent to the retreating side. On the other hand, for the joints produced at the medium and high tool parameters (340 and 410 rpm respectively), failure was observed along the TMAZ/HAZ boundary of the retreating side. Further SEM examination of the fractured surfaces of the samples processed at 270 rpm (Figure 2-6b) revealed the presence of a large amount of dimples (Figure 2-6d and Figure 2-6e) indicating the overload and ductile nature of the fracture. Similar features were observed on samples processed at higher rotational speeds. However, the

samples processed at the lowest tool rotational speed (270 rpm) also featured large voids (~100  $\mu\text{m}$  wide) located at the bottom portion of the weld (Figure 2-6c). These voids were distinct from the deformation dimples, suggesting that they may have resulted from an ineffective material mixing during the welding process. This evidence suggests that these voids are the source of failure through the nugget region, observed at the lowest tool rotational speed. The fact that these voids defects were not detected from metallographic evaluation of the traverse sections, suggests that they are discontinuous along the welding direction. Conversely, the failure observed through the heat affected zone at high rotational speeds was produced due to the material softening as confirmed by the microhardness measurements. As stated before, excess frictional heat dissipates into the material allowing for the coarsening of the strengthening precipitates, which leads to the formation of low strength regions such as the HAZ. This type of failure is typical of FSW joints.

It is important to note that the observed trending of increasing joint strength with increasing tool speed suggests that further studies may lead to higher joint strength for the dissimilar FSW of AA6061-to-AA7050. However, other process parameters such as the transverse welding speed, and the position of the welded materials with respect to the tool rotation, still needs consideration. Regardless, when compared to the AA6061-T6 base material, the resulting joint strength achieved in this study complies with the Specification for Friction Stir Welding of Aluminum Alloys for Aerospace Applications (AWS D17) from the American Welding Society (AWS). The AWS D17 specifies a minimum joint strength of 186 MPa [43].

## 2.5 Summary and Conclusions

The microstructure and mechanical properties of dissimilar friction stir welding of AA6061-to-AA7050 Al alloys were evaluated. FSW joints were produced under a range of tool rotational speeds, while other parameters were held constant. Microstructure analysis of the stir zone revealed the presence of bands of mixed and unmixed material that demonstrated the degree of material intermixing, as the tool rotational speed was varied. Material intermixing and joint strength were found to increase with the increasing tool rotational speed. Scanning electron microscopy analysis revealed that a majority of the welds tested under monotonic tensile loading failed through the heat-affected zone corresponding to the AA6061 Al alloy side of the weld. However, for the low tool rotational speeds, failure occurred in the stir zone due to poor material intermixing. Further research will focus on the optimization of the joint strength and its fatigue properties.

CHAPTER 3  
LOW CYCLE FATIGUE OF DISSIMILAR FRICTION STIR WELDING OF AA6061-TO-  
AA7050 ALUMINUM ALLOYS

3.1 Abstract

In this work, the fatigue behavior and corresponding microstructure of dissimilar friction stir welding (FSW) of AA6061-to-AA7050 high strength aluminum alloys were used to calibrate a microstructurally-sensitive multistage fatigue model. Experimental strain-controlled fatigue testing revealed an increase in the cyclic strain hardening and the number-of cycles to failure as the tool rotational speed was increased. At higher applied strain amplitudes ( $>0.3\%$ ), the corresponding stress amplitude increased and the plastic strain amplitude decreased, as the number of cycles increased. However, at  $0.2\%$  strain amplitude, the plastic strain decreased until it was almost negligible. Inspection of the hysteresis loops demonstrated that at low strain amplitudes, there was an initial stage of strain hardening that increased until it reached a maximum strain hardening level, afterwards a nearly perfect elastic behavior was observed. Under fully-reversed fatigue loading, all samples failed at the region between the heat-affected and thermomechanically-affected zones. Inspection of the fractured surfaces under scanning electron microscopy revealed that the cracks initiated at either the crown or the root surface of the weld, and from secondary intermetallic particles located near the free surface of the weld. Lastly, the microstructure-sensitive multistage fatigue model was employed to correlate the fatigue life of the dissimilar FSW'ed joint considering microstructural features such as grain size,

intermetallic particles and mechanical properties.

### 3.2 Introduction

Due to its numerous advantages over conventional fusion welding (e.g. low distortion of the workpiece, minor loss in parent material properties, and the lack of porosity), the friction stir welding (FSW) technology has been successfully demonstrated for the joining of a variety of materials including high strength aluminum alloys. For example, although weldable by conventional fusion techniques, AA6061 has also been extensively demonstrated to be welded by FSW [8,10–12,55]. On the other hand, the aerospace grade high strength AA7050 [22], which is known to be unweldable by fusion welding [29], has also been successfully welded by FSW [31,32,23,33]. In addition, particular attention has been given to the FSW of dissimilar alloys [43,39,38,40–42,61,67]. However, a dearth of information exists regarding the fatigue properties, especially in the low cycle regime. This article begins to fill that void by providing experimental characterization and modeling of the low cycle fatigue behavior of dissimilar FSW of AA6061-to-AA7050.

#### 3.2.1 Low Cycle Fatigue in Friction Stir Welding

Regarding fatigue life behavior, several investigations have been conducted on FSW of similar aluminum alloys [68,69,45,47,70–77]. In general, these investigations revealed that the fatigue life of the welds at  $10^7$  cycles was much lower than that of the base materials. Despite this fact, the resulting fatigue strength of the FSW was higher when compared to the fusion welds, which is attributed to the significantly finer and more uniform microstructure produced

from the FSW process and a much smaller HAZ. However, despite the many efforts in understanding the fatigue behavior of FSWed Al alloys, the majority of these investigations have been conducted on the high cycle regime, while very little is known about the fatigue performance in the low cycle regime.

Among the most relevant studies on low cycle fatigue behavior of FSW of aluminum alloys; there is the FSW of AA6061 [30], FSW of AA7075 [44] and among other alloys [78–80]. Feng et al. [30] evaluated the processing effects on the low cycle fatigue properties of the FSWed AA6061-T651 Al alloy and compared it with the properties of the parent material. Results revealed that the fatigue resistance and cyclic stress amplitude increased with the increasing tool transverse speed, however, little dependency was observed on the tool rotational speed. Cracks initiated at the sample surfaces and from near-surface defects. The fracture surface was also characterized by fatigue striations and secondary cracks. Similar results were found for the FSWed AA7075 Al alloy [44].

Regarding the fatigue life of dissimilar FSW, very limited published research exists. Among the published studies, the following alloy combinations have been investigated, AA6082-AA2024 Al [45], AA7075-AA6061 [46] and AC4CH-T6/AA6061-T6 [47]. Cavaliere et al [45] reported the high cycle fatigue properties of the dissimilar AA6082-AA2024 Al alloy joined by FSW revealing that the fatigue properties were strongly dependent on which alloy was placed on the advancing side of the joint. Furthermore, they found that fatigue strength increased with the increasing tool speed. Sarsilmaz et al. [46] studied the effects of the process parameters and tool profile on the static and cyclic properties on the dissimilar AA6061-AA7075 FSW. Lastly, Uematsu et al. [47] investigated the dissimilar FSW of AC4CH-T6 cast aluminum to AA6061-

T6 wrought aluminum alloy. In this study, cracks initiated at casting pore defects, resulting in similar fatigue properties as for the cast aluminum alloy.

The purpose of this paper is elucidate the low cycle fatigue behavior of dissimilar FSW of AA6061-to-AA7050 and extend the use of a microstructure-sensitive multistage fatigue model (MSF) for life prediction of the welded joint. To the best of the authors' knowledge, this is the first paper to characterize the fatigue behavior of dissimilar FSW of AA6061-to-AA7050.

### 3.3 Materials and Experiments

Butt friction stir welds were produced using 5 mm thick rolled plates of AA6061-T6 and AA7050-T7451. The nominal composition and mechanical properties for each material is listed in Table 3-1. The alloy plates were welded at three different tool rotational speeds (270, 340, and 410 rpm), while the welding transverse speed was fixed to 114 mm/min. The FSW tool used to weld the plates consisted of a cylindrical threaded pin and a shoulder having a diameter of 10 mm and 18 mm respectively. It is noted that the welding parameters chosen in this study were similar to other studies elsewhere [43,60,62–64]. The butt friction stir welding was performed parallel to the rolling direction of the plates, and by placing the AA7050 on the advancing side. After the welding was completed, the top and bottom surfaces of the welded plates were machined down to 4 mm of thickness. The machining eliminated the stress raisers produced by the flash material at the top of the weld, which are know to substantially reduce the fatigue life of the FS joints. After machining, the specimens for microstructural and mechanical characterization were cut perpendicular to the welding direction by using a water jet. A schematic representation of the preparation of the samples is presented in Figure 3-1. Microstructural characterization of the welds was carried out using optical (OM), scanning

electron microscopy (SEM), and energy dispersive x-ray spectrometry (EDS). The transverse sections of the welds were prepared using conventional metallographic techniques, and etched for 60 seconds in a solution consisting of 1g NaCl and 50mL H<sub>3</sub>PO<sub>4</sub> dissolved in 125mL of ethanol, followed by a 5 seconds step using Wecks's tint (4 g of KMnO<sub>4</sub> and 1 g of NaOH dissolved in 100 ml of distilled water). Vickers microhardness measurements were performed in the transverse sections of the FSWed samples using 0.5 mm spacing, a load of 100 gf and a dwell time of 5 seconds.

**Table 3-1. Nominal composition and mechanical properties for AA6061-T6 and AA7050-T7451 plates.**

Material	Al	Si	Cu	Mg	Cr	Zn	UTS S <sub>u</sub> (MPa)	YS S <sub>y</sub> (MPa)	Elongation ε (%)
AA6061-T6	Bal.	0.6	0.3	1.0	0.2	-	310	275	15
AA7050-T7451	Bal.	-	2.3	2.2	-	6.2	524	469	11

The fatigue and tensile samples were prepared having a width of 6 mm and a gage length of 50.8 mm (Figure 3-1). Prior to any testing, samples were hand ground using silicon carbide paper to 600 grit finish. Subsequently, fatigue testing was performed in fully reversed (R=-1) strain control condition at 5 Hz using a servo-hydraulic load frame. Testing was conducted at room temperature (~21°C) with relative humidity varying from 30 to 40%. The strain amplitude was

varied from 0.7 to 0.2 % strain while testing was performed in duplicates. Fatigue failure was defined when the maximum cycle load dropped by 50%. A servo-hydraulic load frame with a 100 kN load cell performed the tensile experiments in triplicate with a 25 mm clip-on extensometer at a strain rate of 0.001/s. Post-mortem fractography was performed using optical and scanning electron microscopy techniques.

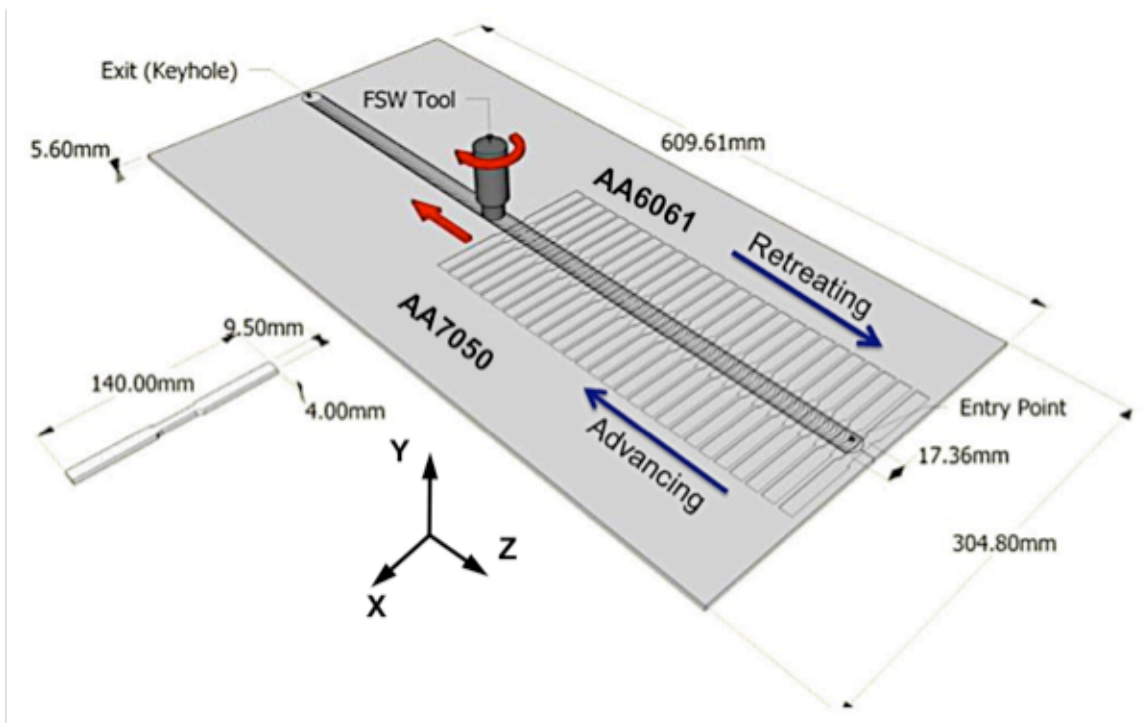


**Figure 3-1. Schematic representation of the dissimilar AA6061-AA7050 FSW. The welds were carried out parallel to the rolling direction of the plates, and by placing the AA7050 alloy on the advancing side. Fatigue test coupons were cut perpendicular to the welding direction.**

## 3.4 Results And Discussion

### 3.4.1 Microstructure

An example of the macrostructure of the dissimilar FSW of AA6061-to-AA7050 is shown in Figure 3-2. This particular joint was prepared under a tool rotational speed of 410 rpm and a transverse welding speed of 114 mm/min. Figure 3-2a-c correspond to the top surface (crown), cross-section and bottom surface (root) of the weld, respectively. The material in the right-hand-side (advancing side) of the joint corresponds to the AA7050, while the material in the left-hand-side (retreading side) corresponds to the AA6061. Three main regions of the weld can be clearly distinguished, corresponding to the stir zone (SZ), the thermo mechanical affected zone (TMAZ), and the heat affected zone (HAZ). The SZ features vortex structures, or “onion rings” which are typical of FSW, but are exaggerated in the welding of dissimilar metals [37]. Furthermore, these onion rings comprises alternate lamella of material corresponding to the base alloys and a mixture of both as presented in [81].

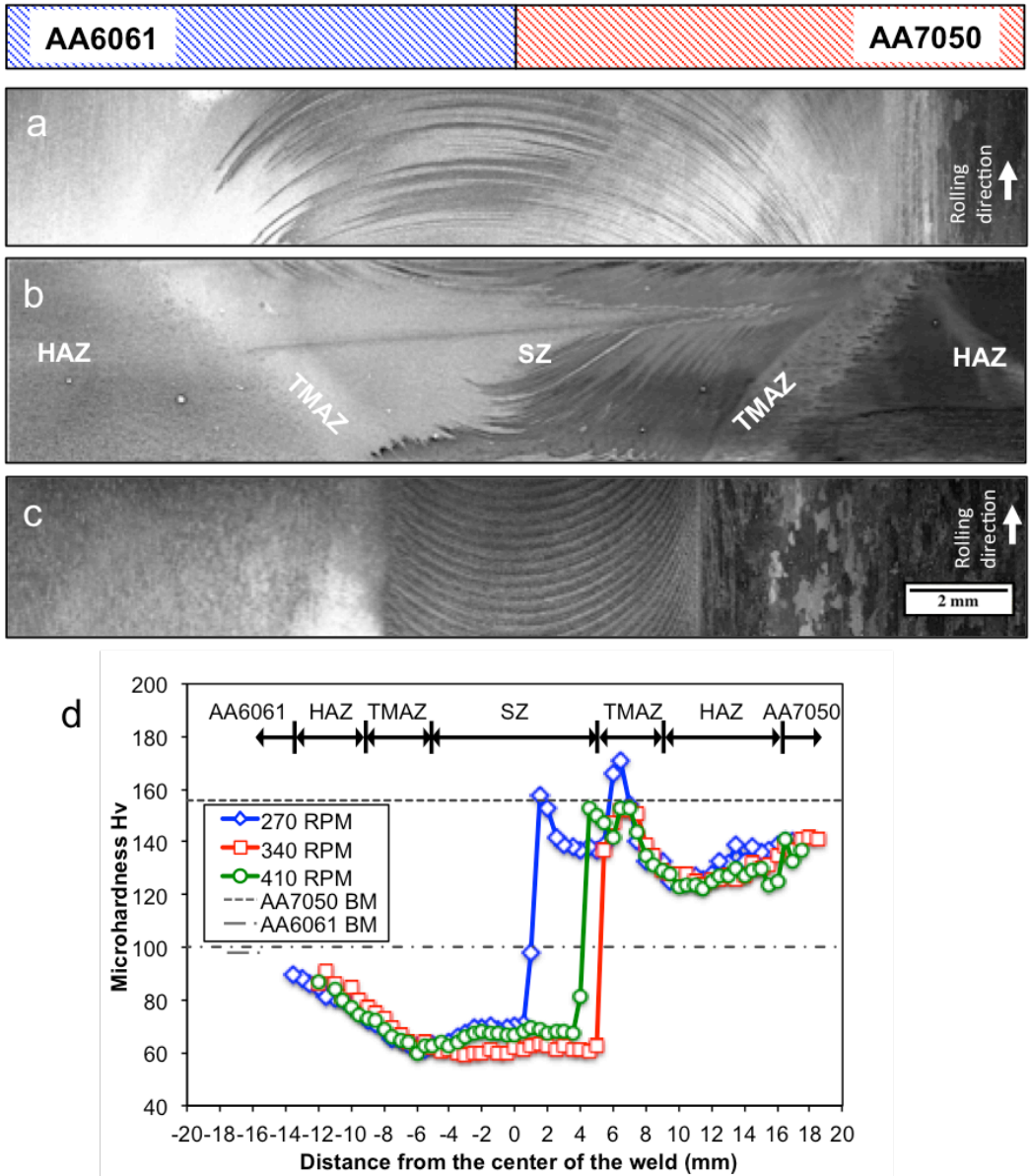


Figure 3-2. (a) Top (crown), (b) cross-section and (c) bottom (root) surface for the dissimilar FSW of AA6061-to-AA7050, processed at 410 RPM. (d) Microhardness profiles obtained from the center of the cross-sections of the dissimilar FSW at various tool rotational speeds.

Figure 3-2d shows the Vickers microhardness profiles for the three parameters evaluated in this study. As can be seen, an asymmetric hardness profile was obtained, which is typical of dissimilar FSW. Hardness peaks were observed in the SZ adjacent to the AA7050 AL Alloys, whereas local minimums were observed in the SZ adjacent to the AA6061 Al alloy. Furthermore, the formation of the HAZ was observed due to the presence of low hardness regions next to the SZ for both parent alloys. It is well known that both alloys are susceptible to thermal processing [25], therefore, the excess heat produced during the FSW alters the formation of the strengthening precipitates, which results in the hardness variation observed along the cross section of the weld. In addition, natural aging at room temperature may have also contributed to the observed hardness variations [32]. In summary, no obvious differences were found between the tool rotational speeds evaluated in this study. However, as presented later in this paper, differences were found in the cyclic hardening properties and the crack propagation characteristics between the parameters evaluated in this study.

Figures 3a-f presents magnified images corresponding to the SZ, TMAZ and to the base materials (BM) of the AA6061 and AA7050. As can be seen in Figures 3a-b the microstructures of both parent materials were severely refined in the SZ due to the stirring action of the rotating tool. The base materials comprise elongated grains,  $\sim 100$  and  $\sim 20$   $\mu\text{m}$  in the X and Y direction, respectively (Figure 3e-f). However, the SZ featured significantly refined equiaxed microstructure achieved via dynamic recrystallization (DRX)[31]. Results revealed a grain size varying from 3.8 to 5.8  $\mu\text{m}$  for the SZ consisting of AA6061 and for the AA7050. On the other hand, the TMAZ featured large subgrains; evidence that partial mechanical deformation occurred in this area. No significant differences in grain size were observed between the RPMs. A summary of the grain

size measurements of the various regions and tool rotational speeds is presented in Table 3-2. In addition, the Al-Si-Fe and Al-Fe-Cu coarse intermetallic particles corresponding to the TMAZ and SZ of the AA6061 and AA7050 were observed using the backscatter electron detector (BSE) as shown Figure 3-4. In fact, Figure 3-4 identifies secondary intermetallic particles between 16 and 1  $\mu\text{m}$  in diameter in the TMAZ of both materials. The large particles were broken into smaller particles ( $<5 \mu\text{m}$ ) in the SZ.

**Table 3-2. Average grain size for different locations of the weld and various tool rotational speeds.**

Tool Rotational Seed	Grain Size ( $\mu\text{m}$ )			
	SZ AA6061	SZ AA7050	TMAZ/HAZ	TMAZ/HAZ
			AA6061	AA7050
270 rpm	3.8	3.8	11.4	8.0
360 rpm	4.9	5.2	11.2	5.6
410 rpm	5.8	5.1	11.7	10.2

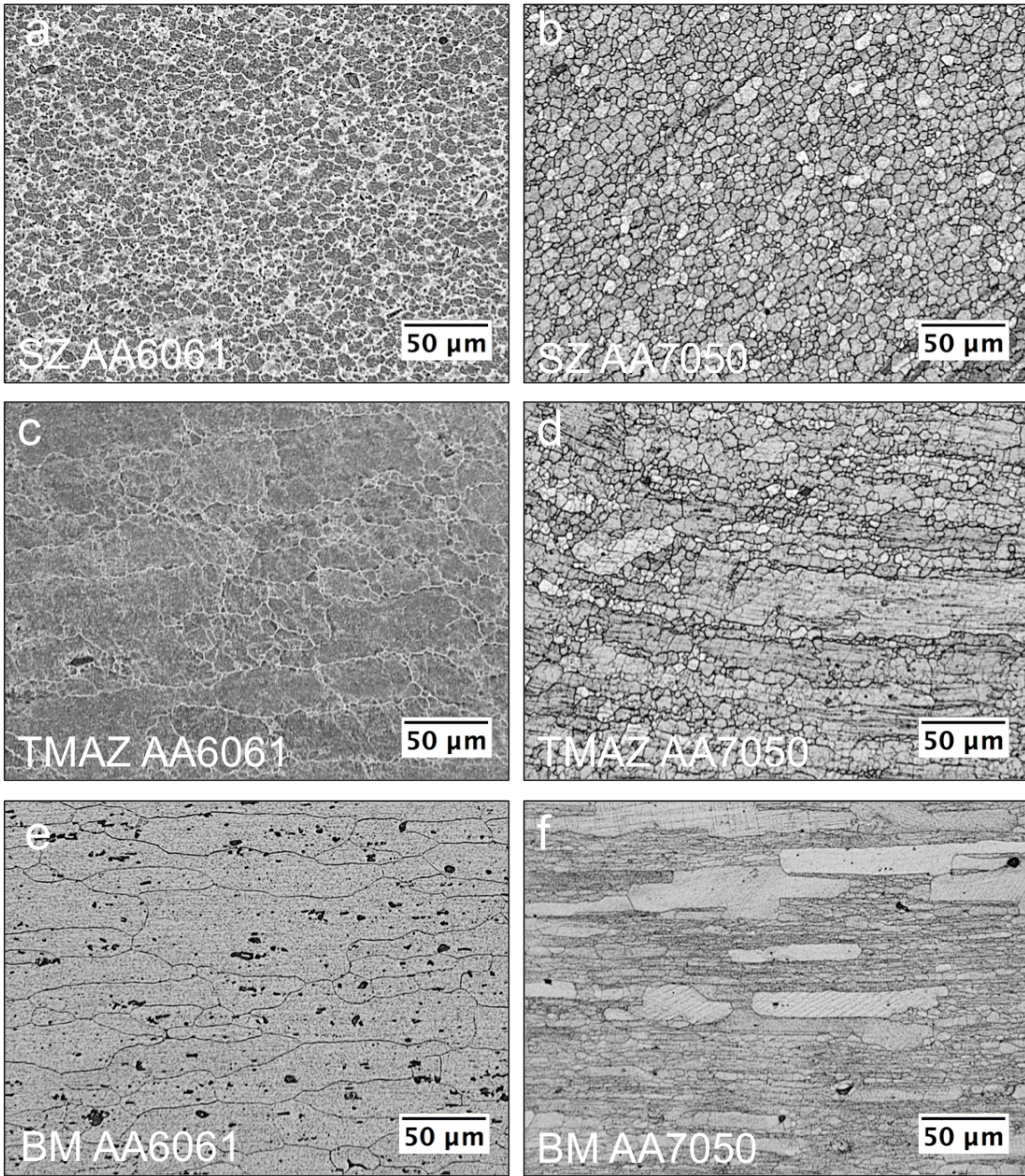


**Figure 3-3. Optical micrographs showing the microstructure at different locations of the (a-d) cross section of the weld and (e-f) the base materials.**

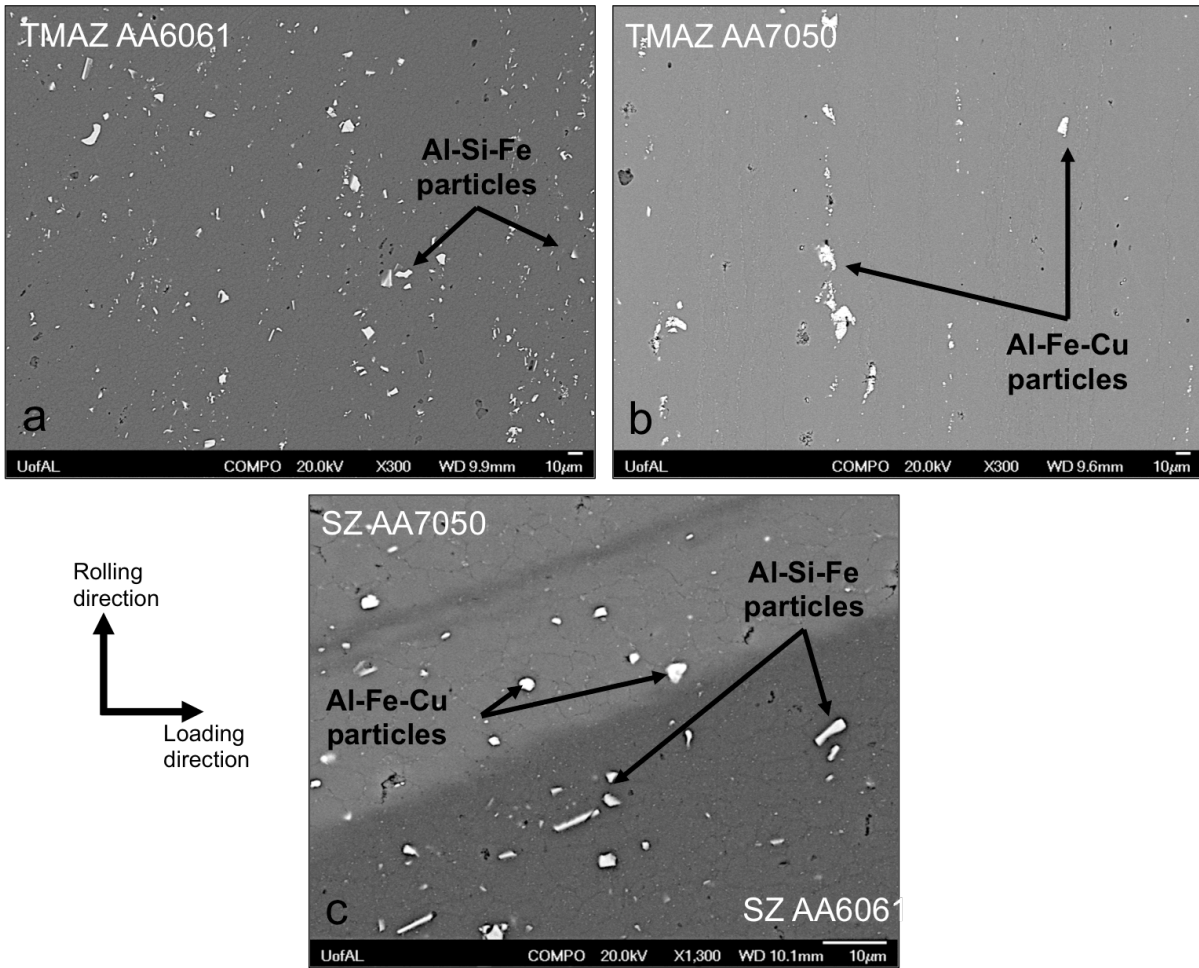


**Figure 3-4. SEM backscatter micrograph showing the location of the secondary intermetallic parties located in the TMAZ corresponding to the (a) AA6061 and the (b) AA7050, and the (C) SZ. This micrographs were obtained form the top view of the weld.**

### 3.4.2 Tensile Testing

Table 3 summarizes the monotonic tensile results of the dissimilar FSW of AA6061-to-AA7050. The monotonic tensile results demonstrated an apparent increase in the yield and the ultimate tensile strength of the joint as the tool rotational speed was increased. The highest joint strength was obtained for the highest tool rotational speed (410 rpm), having an average ultimate

tensile strength of 192.6 MPa. All the joints failed on the lower strength AA6061 side. These results are in agreement with other studies on dissimilar joining, where failure was observed at either the HAZ or the TMAZ of the material with the lowest strength [43,63,65,66].

**Table 3-3. Summary of the monotonic tensile properties for the dissimilar FSW AA6061-to-AA7050 and the base materials.**

Tool Rotational Speed	Modulus	YS	UTS	Elongation	Strength	Hardening
	of elasticity <i>E</i> (GPa)	<i>S<sub>y</sub></i> (MPa)	<i>S<sub>u</sub></i> (MPa)	$\epsilon$ (%)	coefficient <i>K</i> (MPa)	exponent <i>n</i>
270 rpm	69.7	129.7	166.4	8.2	355.2	0.159
360 rpm	69.7	131.3	191.3	8.0	354.9	0.155
410 rpm	69.7	134.2	192.6	6.0	352.1	0.151
AA6061-T6	68.9	310	275	15.0	-	-
AA7050- T7451	71.7	524	469	11.0	-	-

The results for the low cycle fatigue testing on the dissimilar FSW of AA6061-to-AA7050, including the low cycle fatigue data from literature for the AA6061 BM and other FSW studies are presented in Figure 3-5. As for the dissimilar FSW of AA6061-to-AA7050, for the strain amplitude range of 0.3% to 0.7%, the results revealed a small increase in the fatigue life as

the tool rotational speed increased. The differences in the fatigue life were more obvious on the lowest tool rotational speed (270 rpm), however, for the case of the medium and high levels (340 and 410 rpm), the results show no apparent increase in performance. Also, for low strain amplitudes (0.2% strain), the differences between the tool rotational speed and the resulting fatigue life were not obvious. Furthermore, the fatigue experiments of this study revealed a lower fatigue life at high strain amplitudes ( $>0.3\%$  strain) when compared to the results for the AA6061 BM and FSW AA6061 (600 rpm-200 mm/min) obtained by Feng et al. [30]. However, the results for fatigue life for the dissimilar FSW AA6061-to-AA7050 were very close to the results obtained by Feng for the BM and FSWed AA6061 at low strain amplitudes (0.2% strain).

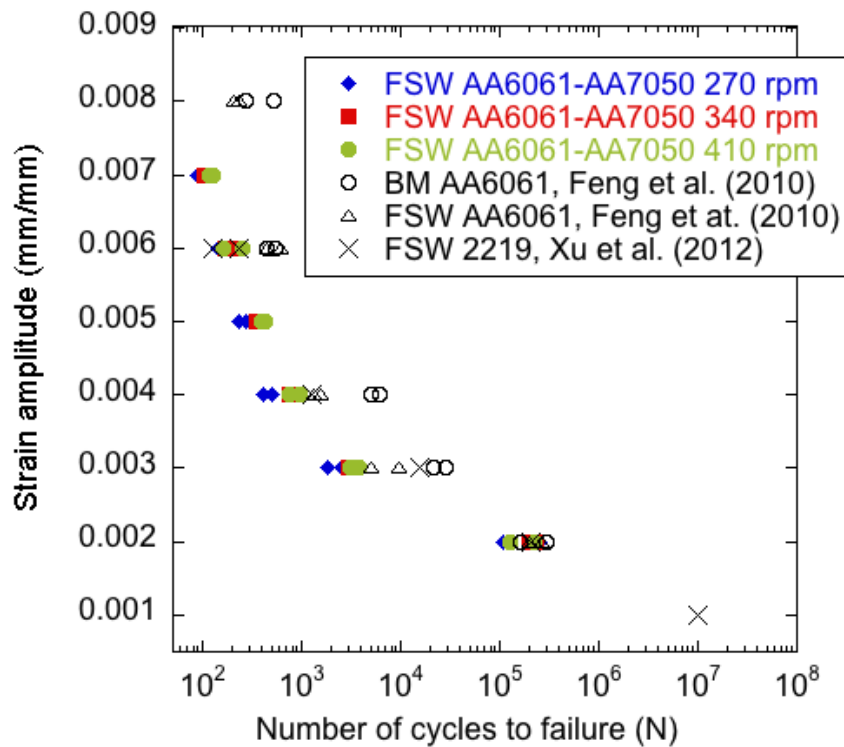


**Figure 3-5. Experimental data for the low-cycle fatigue life for the dissimilar FSW AA6061-to-AA7050 for various tool rotational speeds, and the low cycle fatigue data for the**

**AA6061-T6 base material [30], FSW AA6061-T6 (600 rpm-200 mm/min) [30], and the FSW 2219 (300 rpm- 100 mm/min) [78] adopted from various studies.**

### 3.4.3 Cyclic Stress and Strain Response

Figure 3-6a-b show the stress amplitude and the plastic strain amplitude evolution for the tool rotational speeds of 270 and 410 rpm. For all the range of parameters tested in this study, the stress amplitude increased with the increasing number of cycles (Figure 3-6a). Conversely, the plastic strain amplitude decreased with the increasing number of cycles, which illustrates the degree of cyclic hardening. Based on these observations, it is evident that the joint experienced cyclic strain hardening as the number of cycles increased, where larger strain hardening was measured for the tool rotational speed of 410 rpm. These observations are supported by Figure 3-6c, where the hysteresis loops corresponding to the low cycle fatigue for the tool rotational speed of 410 rpm and strain amplitude of 0.4% are shown. As can be seen in Figure 3-6, strain hardening occurred as the number of reversals was increased. The stable mid-life loop (Figure 3-6c) further illustrates when the maximum strain hardening was achieved at the 0.4% strain amplitude. Furthermore, for large strain amplitudes ( $>0.3\%$ ), the strain occurred in three stages, each of them showing a nearly linear increasing behavior. The first stage occurred at the first few cycles, the second stage occurred from a few cycles up to the  $10^2$ , and the last stage occurred after  $10^2$  cycles. Furthermore, the slope of the stress amplitude increased as each stage progressed, demonstrating that the rate of strain hardening was increasing.

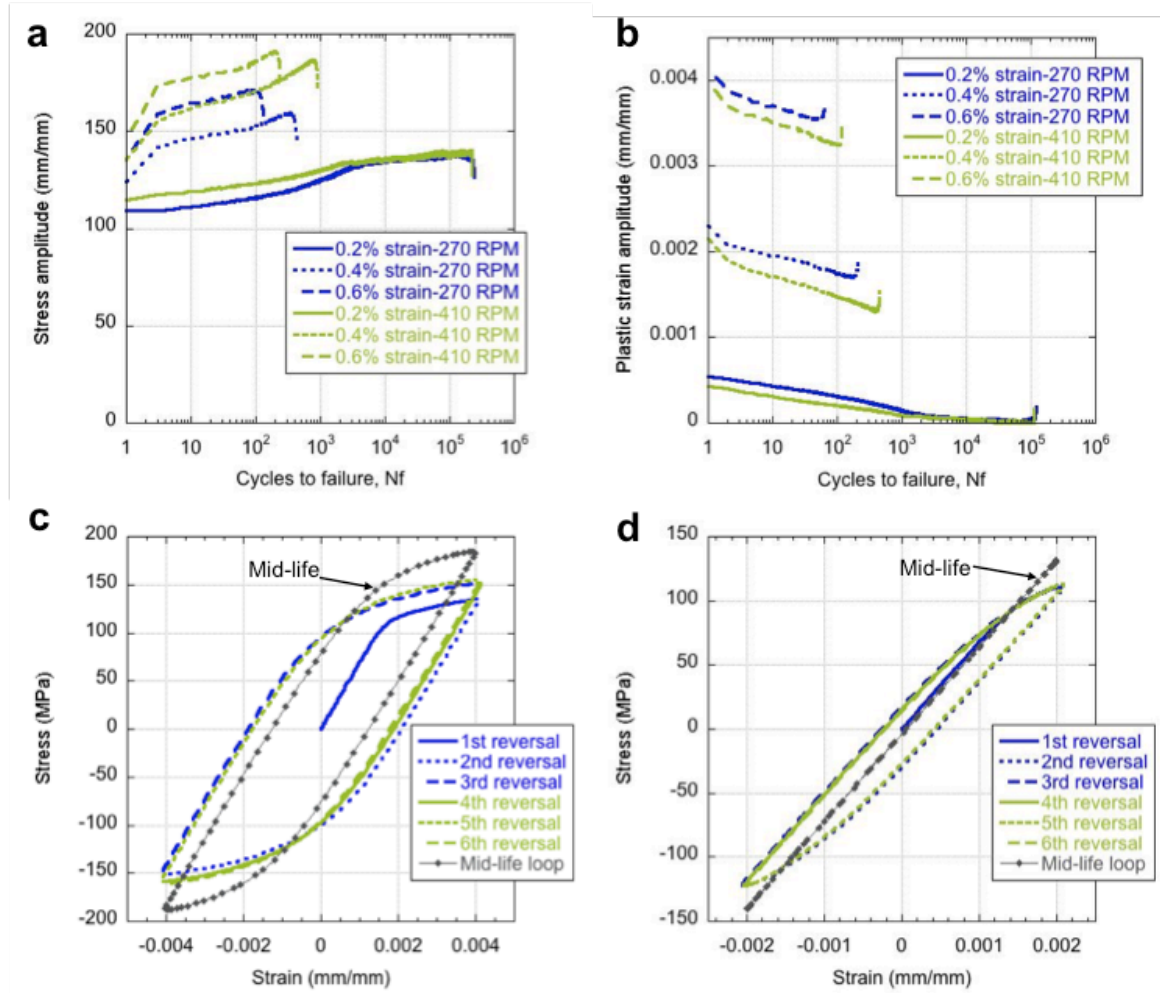


**Figure 3-6. (a) Stress amplitude and (b) plastic strain amplitude versus the number of cycles to failure for various strain amplitudes and tool rotational speeds. Hysteresis loops for (c) 0.4% and (d) 0.2% strain amplitude for a tool rotational speed of 410 rpm.**

As shown in Figure 3-6d, for the tool rotational speed of 410 rpm and a strain amplitude of 0.2%, the strain hardening continued increasing, resulting in the complete elastic behavior when the mid-life was reached. This behavior was observed in all the welding parameters and only at 0.2% strain amplitude. Furthermore, this behavior is confirmed by the stress and plastic strain

amplitude evolution shown in Figure 3-6a and Figure 3-6b, where at a strain amplitude of 0.2%, the stress amplitude increased at a non-linear rate until it reached  $10^3$  cycles, which after this point, a nearly linear behavior was observed, showing a much slower rate of strain hardening. Conversely, for the plastic strain amplitude (Figure 3-6b), the plastic strain decreased until  $10^3$  cycles was reached, after this point the plastic strain was almost or completely negligible. Inspection of the hysteresis loops demonstrated that at such low strain amplitudes, there is an initial stage of strain hardening that constantly increased until it reached a maximum strain hardening point; afterwards a nearly perfect elastic behavior was observed. Thus, observations of the hysteresis suggests that the first stage of hardening corresponded to the cyclic hardening of the low hardness regions, in particular the TMAZ/HAZ of the AA6061. This is supported by the crack propagation along the HAZ/TMAZ of the AA6061 side that will be discussed later in this paper.

### 3.4.4 Low Cycle Fatigue Parameters

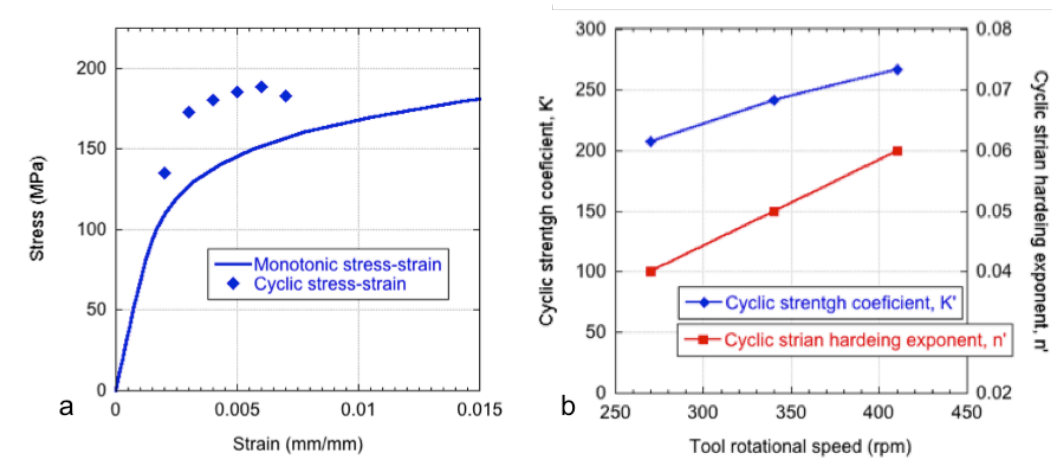


**Figure 3-7. (a) Monotonic and cyclic stress strain curves for the dissimilar FSW of AA6061 and AA7050 Al alloys produced at a tool rotational speeds of 410 rpm. (b) Cyclic strength coefficient and cycle strength exponent as a function of the tool rotational speed.**

The monotonic and the cyclic stress-strain curves for a FSW joint processed at 410 rpm are presented in Figure 3-7a. The solid curve was obtained from the monotonic tensile test performed at in displacement control mode at a rate of 1 mm/min using a 25.4 mm extensometer. On the other hand, the cyclic stress-strain points represent the average of the duplicates tested in low cycle fatigue for the same welding condition. The cyclic stress-strain curve was assembled by obtaining the stress amplitude values corresponding to the tip of the stable mid-life hysteresis loops, and their corresponding strain amplitude. As demonstrated in Figure 3-7a, the strain hardening occurred much faster during cyclic loading as compared to the monotonic tensile loading.

Similar to monotonic strain hardening behavior in the stress-strain curve, the cyclic strain hardening can be modeled as a power function as follows;

$$\sigma_a = K' \left( \frac{\Delta \varepsilon_p}{2} \right)^{n'} \quad (1)$$

where  $\sigma_a$  is the plastic strain amplitude,  $K'$  is the cyclic strength coefficient and  $n'$  is the cyclic strength exponent. The cyclic strain hardening coefficient and exponent calculated with Equation 1 demonstrated an increase in both properties as the tool rotation speed was increased. As shown in Figure 3-7b, a nearly linear dependency of the cyclic properties (i.e.  $K'$  and  $n'$ ) on the tool rotational speed was observed for the calculated values of both properties. It has to be clarified that these values represent the results for the range of evaluated parameters in this study. Further research is required for the optimization of this joint, including exploring the effects of a different range of welding parameters.

Using the strain-life approach, the low cycle fatigue properties can be estimated by resolving the elastic and plastic strain amplitude component from the total strain amplitude. This can be expressed as follows;

$$\frac{\Delta\varepsilon}{2} = \varepsilon_a = \frac{\Delta\varepsilon_e}{2} + \frac{\Delta\varepsilon_p}{2} \quad (2)$$

Where,  $\Delta\varepsilon/2 = \varepsilon_a$  is the total strain amplitude, and  $\Delta\varepsilon_e/2$  and  $\Delta\varepsilon_p/2$  are the elastic and plastic strain amplitude components obtained from the stable mid-life hysteresis loops.

The elastic and plastic strain components can be expressed by using the Basquin (Equation 3) and Coffin-Manson (Equation 4) equations, which are defined as;

$$\frac{\Delta\varepsilon_e}{2} = \frac{\sigma_f'}{E} (2N_f)^b \quad (3)$$

$$\frac{\Delta\varepsilon_p}{2} = \varepsilon_f (2N_f)^c \quad (4)$$

In Equation 3,  $E$  is the elastic modulus,  $\sigma_f'$  is the fatigue strength coefficient and  $b$  is the fatigue strength exponent. In Equation 4,  $\varepsilon_f$  is the fatigue ductility coefficient,  $c$  is the fatigue ductility exponent and  $N_f$  is the number of cycles to failure. The low cycle fatigue properties obtained for the dissimilar FSW AA6061-to-AA7050 samples under the range of the tested parameters, are summarized in Table 3-3.

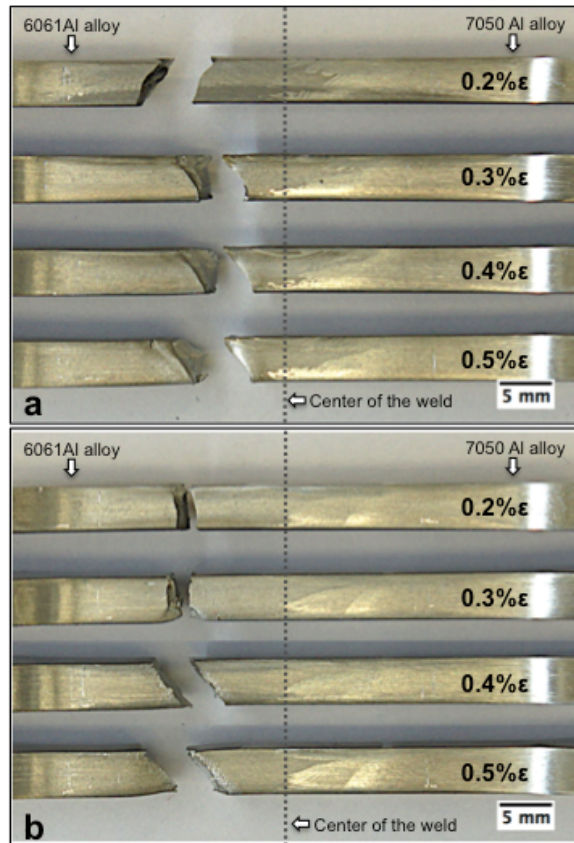
**Table 3-4. Summary of the low cycle fatigue properties for the dissimilar FSW AA6061-to-AA7050.**

Tool rotational speed	Cyclic yield strength	Cyclic hardening exponent	Cyclic strength coefficient	Fatigue strength coefficient	Fatigue strength exponent	Fatigue ductility coefficient	Fatigue ductility exponent
	$\sigma_{ys,c}$ (MPa)	$n'$	$K'$ (Mpa)	$\sigma'_y$ (MPa)	$b$	$\epsilon'_f$	$c$
270 rpm	164.3	0.04	207.6	196.7	-0.03	0.16	-0.75
360 rpm	174.6	0.05	241.1	218.3	-0.04	0.13	-0.69
410 rpm	181.0	0.06	266.9	238.7	-0.04	0.14	-0.68

### 3.4.5 Fractography

Figure 3-8 through Figure 3-11 shows the representative fracture surfaces of the dissimilar FSW AA6061-to-AA7050 after the low cycle fatigue testing. For brevity's sake, only the tool rotational speeds for the low and the high levels (270 rpm and 410 rpm) are presented. However, the results obtained for the samples processed at 410 rpm resemble the observations made for the samples processed at 360 rpm. As shown in Figure 3-8, all samples failed at the AA6061 side of the weld. A close examination revealed that the samples processed at 360 and 410 rpm, failed along the TMAZ/HAZ region of the AA6061 side. Interestingly, for high strain amplitudes (>0.4% strain), the crack propagation occurred along the TMAZ/HAZ region,

however, at low strain amplitudes ( $<0.3\%$  strain), a flat fracture surface was observed extending mostly in the HAZ. On the other hand, for the tool rotational speed of 270 rpm, the location for the crack propagation was different. As shown on Figure 3-8a, the samples produced at 270 rpm failed very close to the left-hand end of the SZ. This observation is in agreement with the results obtained from the monotonic tensile tests for the same processing conditions [81]. After monotonic tensile testing, inspection of the fracture surfaces of the dissimilar joints suggests that inadequate material intermixing (evidence by the presence of voids defects) produced at low tool rotational speeds, was the cause for the low mechanical strength and failure through the stir zone. In fact, these same defects have been reported in literature as partial forgings defects [71]. Although their presence was never associated with crack initiation during fatigue failure, they were found to affect the overall fatigue life by providing easy linking pathways between the initiated cracks.



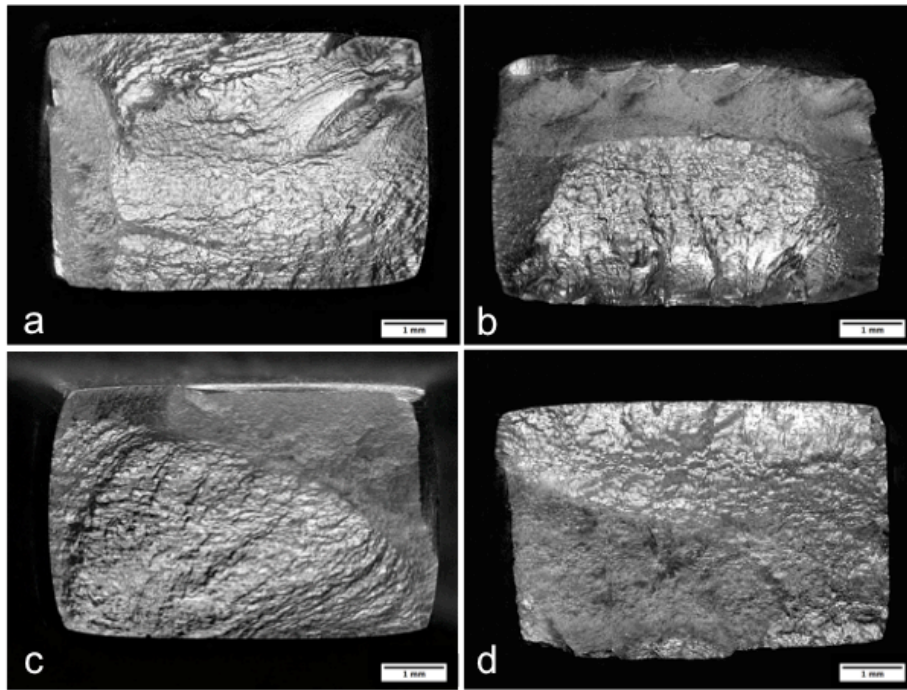
**Figure 3-8. Typical optical micrographs showing the failure locations at various strain amplitudes the dissimilar FSW 6061-to-7050 Al alloys. (a) Welds produced at (a) 270 rpm and (b) 410 rpm.**

Figure 3-9a-b show the overview of the fractured surfaces of the samples corresponding to the process parameter of 270 rpm and tested at 0.2% and 0.4% strain. Figure 3-9c-d shows the fractured surfaces of the samples corresponding to the process parameter of 410 rpm and tested at 0.2% and 0.4% strain. For all the process parameters, cracks initiated at either the top (crown) or bottom (root) surfaces of the welds, and propagated towards the center of the joints. In fact, for the medium and high tool rotational speeds (340 and 410 rpm), there was no evidence of

cracks initiating at the surfaces corresponding to the cross-section of the welds (side surfaces of the fatigue specimens). At low strain amplitudes (0.2% strain), the fracture was characterized by a flat surface with cracks initiating at the surfaces (either crown or root) of the specimen (Figure 3-8 and Figure 3-9). On the other hand, at high strain amplitudes (0.4% strain), the fracture surfaces were characterized by a shear type fracture along the TMAZ/HAZ boundary (Figure 3-8 and Figure 3-9). Although, at the low tool rotational speed (270 rpm), the cracks initiated in a similar fashion to the rest of the rotational speeds, the crack propagation was observed to be different. As presented in Figure 3-8a, at 270 rpm, the cracks propagated along the left-hand end of the SZ. At high strain amplitudes ( $>0.4\%$ ) for all the samples processed at 270 rpm, the cracks were initiated at the root surfaces. In fact, the lower portion of the fracture surfaces was characterized by the presence of ratchet marks as shown in Figure 3-9d. At 0.2% strain amplitude and 270 rpm, the cracks initiated at either the crown or root surfaces and propagated along the welded region.

The crack initiation sites for the samples are presented in Figure 3-10 and Figure 3-11. For the brevity's sake, only the fracture surfaces corresponding to the high level of tool rotational speed (410 rpm), and 0.2% and 0.4% strain amplitude, are presented. As shown in Figure 3-10a, crack initiation occurred at the bottom of the weld for the tool rotational speed of 410 rpm tested at a low strain amplitude (0.2% strain). A higher magnification image of the crack initiation site is shown in the SEM micrograph in Figure 3-10b. The crack initiation site featured a large void at the surface of the specimen, which is approximately 70  $\mu\text{m}$  wide by 40  $\mu\text{m}$  long. This evidence suggests that the crack initiated at this void, however, there was no correlation that the crack initiated at the secondary particles. Careful examination of the top and bottom surfaces of this

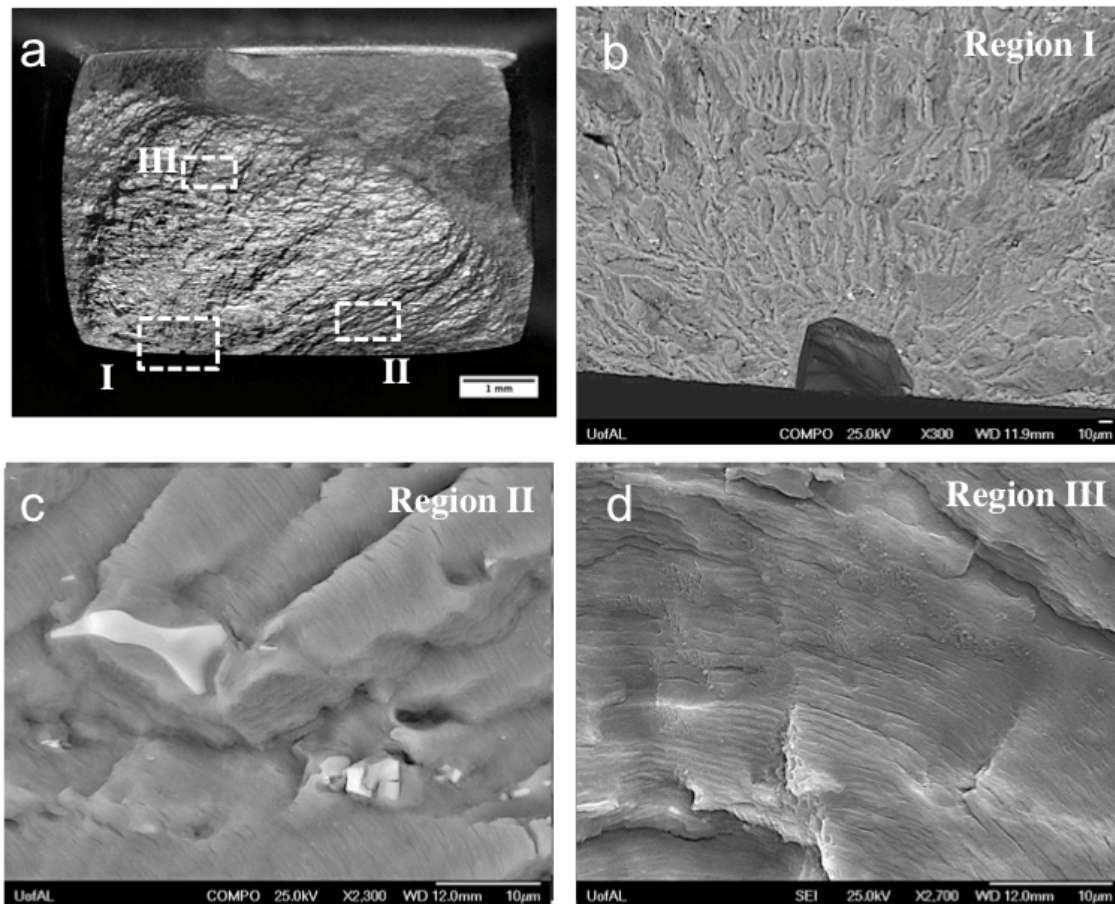
sample confirmed that the crack did not initiate at surface defects originated from the sample preparation prior to the mechanical test. Fractography analysis suggests that the defects corresponding to the base material, such as voids and particle clustering as the sources for the void observed in this fractured surfaces.



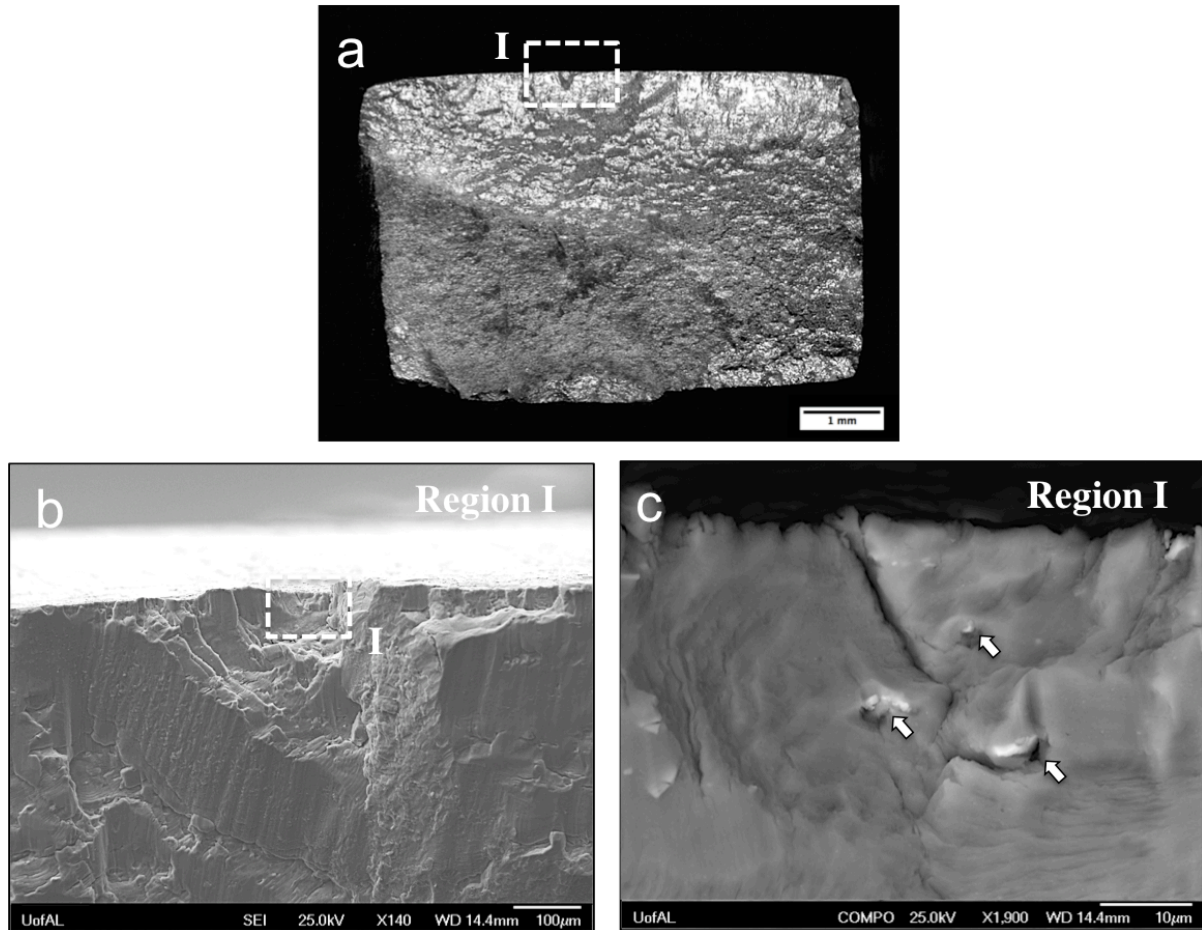
**Figure 3-9. Optical micrographs showing the fracture surfaces for the welds processed at 270 RPM (a-b) and 410 (c-d) and tested under cyclic loading at 0.2 % (a-c) and 0.4% (b-d) strain amplitude.**

Figure 3-11 depicts an SEM overview of the fracture surface for a joint produced at 410 rpm and tested at 0.4% strain. As shown in Figure 11a, the crack initiation site was identified at the crown surface of the weld (Region I). Close examination of the crack initiation site (Region I in Figure 3-11b) revealed that the crack initiated at secondary phase particles (white arrows

Figure 3-11c) located near the free surface of the specimen. The size of these particles appeared to be approximately 5  $\mu\text{m}$  in diameter.



**Figure 3-10. (a) Typical fracture surface for the weld produced at a tool rotational speed of 410 rpm and tested at 0.2% strain amplitude. (b) Magnified images of a crack initiation site on the bottom surface (Region I). (c) Backscatter electron image of showing the morphology of the fractured second particles in Region II. (d) Magnified image of Region III, showing the striations observed in the stable crack propagation region.**



**Figure 3-11. (a) Typical fracture surface for the weld produced at a tool rotational speed of 410 rpm and tested at 0.4% strain amplitude. (b-c) Magnified images of a crack initiation site on the top surface (region I). (c) Backscatter electron image of the crack initiation site at Region I showing the secondary particles and crack initiating from them. The secondary intermetallic particles at the crack initiation site are identified with the white arrows.**

In general, as shown in Figure 3-10 and Figure 3-11, the fatigue fracture surfaces of the dissimilar joints were characterized by fatigue striations and the presence of fractured secondary particles. At strain amplitudes larger than 0.3%, the effect of void defects in the SZ was

negligible since cracks initiated from intermetallic particles. However, at low strain amplitude (0.2%), the effects of the void defects were more evident since they provided easy linking pathways between the initiated cracks. This explains the small differences in the fatigue life between the tool rotations speeds at 0.2% strain amplitude (Figure 3-5).

#### 3.4.6 Multistage Fatigue Modeling

While the strain–life approach can effectively capture the fatigue behavior of FSW, this method cannot account for microstructural features and welding defects. As such, a multistage fatigue (MSF) modeling approach was implemented for the fatigue life correlation of the dissimilar FSW of AA6061-to-AA7050. Initially developed by McDowell and co-workers [82] for the fatigue life modeling of aluminum cast alloys, this model have been extended to other alloy systems and processing methods including Mg [83–86], Al alloys [87–90], and steels [91–93]. This model was developed to evaluate the sensitivity of fatigue response to microstructural features with the purpose of being applied to the fatigue life prediction in the design of materials and structural components. For example, the model considers the role of local constrained microplasticity at fractured inclusions and their effect in the crack incubation, and the microstructural small crack growth [94]. Lastly, based on the dimensions of the material inclusions, the upper and lower bounds of the fatigue life can be predicted.

The fatigue damage evolution predicted by the MSF model, is divided in three main stages as

$$N_{Total} = N_{Inc} + N_{MSC/PSC} + N_{LC} \quad (5)$$

where  $N_{Total}$  is the total fatigue life, the  $N_{Inc}$  is the number of cycles required for the crack incubation,  $N_{MSC/PSC}$  and  $N_{LC}$  are the number of cycles required for the propagation of the microstructurally small/physically small crack (*MSC/PSC*), and the propagation of the long crack (*LC*) respectively.

The  $N_{inc}$  comprises the number of cycles of a crack incubating at an inclusion, particle, cluster or pore. This stage is treated in the MSF model as a microscale damage parameter in a modified Coffin-Manson law. This nonlocal parameter around the inclusion is described as  $\beta$  and is expressed by Equation 6 as

$$C_{inc} N_{inc}^{\alpha} = \beta = \frac{\gamma_{max}^{P*}}{2} \quad (6)$$

Thus,

$$C_{inc} = CNC + z(C_m - CNC) \quad (7)$$

$$CNC = C_n(1 - R) \quad (8)$$

where  $C_{INC}$  and  $\alpha$  are the coefficient and exponent values obtained for the modified Coffin-Manson law for incubation (Equation 6). On the other hand,  $C_m$  and  $C_n$  are model constants and the  $R$  and  $z$ , are the load ratio and localization multiplier (Equation 9).

$$z = \frac{l}{D} - n_{lim} \quad (9)$$

Thus,  $D$  is the size of the critical inclusion where that crack incubates,  $l$  is the size of the plastic zone in front of the inclusion, and  $n_{lim}$  is the limiting factor that defines the transition from constrained to unconstrained micronotch root plasticity.

The driving force for the propagation of the microstructurally/physically small cracks in  $N_{MSC/PSC}$ , is defined by the crack tip opening displacement and expressed as

$$\left(\frac{da}{dN}\right)_{MSC} = \chi(\Delta CTD - \Delta CTD_{th}) \quad (10)$$

where  $\Delta CTD$  is the crack tip opening displacement range,  $\Delta CTD_{th}$  ( $2.48 \times 10^{-1} \mu\text{m}$ ) is the crack tip displacement threshold,  $\chi$  is a material constant (0.32 for Al alloys), and the initial crack  $a_i$  is defined as  $0.625D$ .

The crack tip opening displacement range is defined as

$$\Delta CTD = C_{II} \left(\frac{GS}{GS_0}\right)^\omega \left(\frac{GO}{GO_0}\right)^\varpi \left[\frac{U\Delta\hat{\sigma}}{S_{ut}}\right]^\zeta a + C_I \left(\frac{GS}{GS_0}\right)^\omega \left(\frac{GO}{GO_0}\right)^\varpi \left(\frac{\Delta\gamma_{max}^p}{2}\right)^2 \quad (11)$$

where  $C_I$  is the low cycle fatigue coefficient,  $C_{II}$  and  $\zeta$  are the coefficient and exponents for the high cycle fatigue regime.  $S_{ut}$  is the ultimate tensile strength obtained from the monotonic tensile test,  $a$  is the crack length.  $GS$ ,  $GS_0$ ,  $GO$ ,  $GO_0$   $\omega$  and  $\varpi$  are model constants for grain size and orientation. The equivalent uniaxial stress amplitude is defined by  $\Delta\hat{\sigma}$  and the means stress effects is defined by  $U$ . Additional detailed description of the model can be found in [82,89,94].

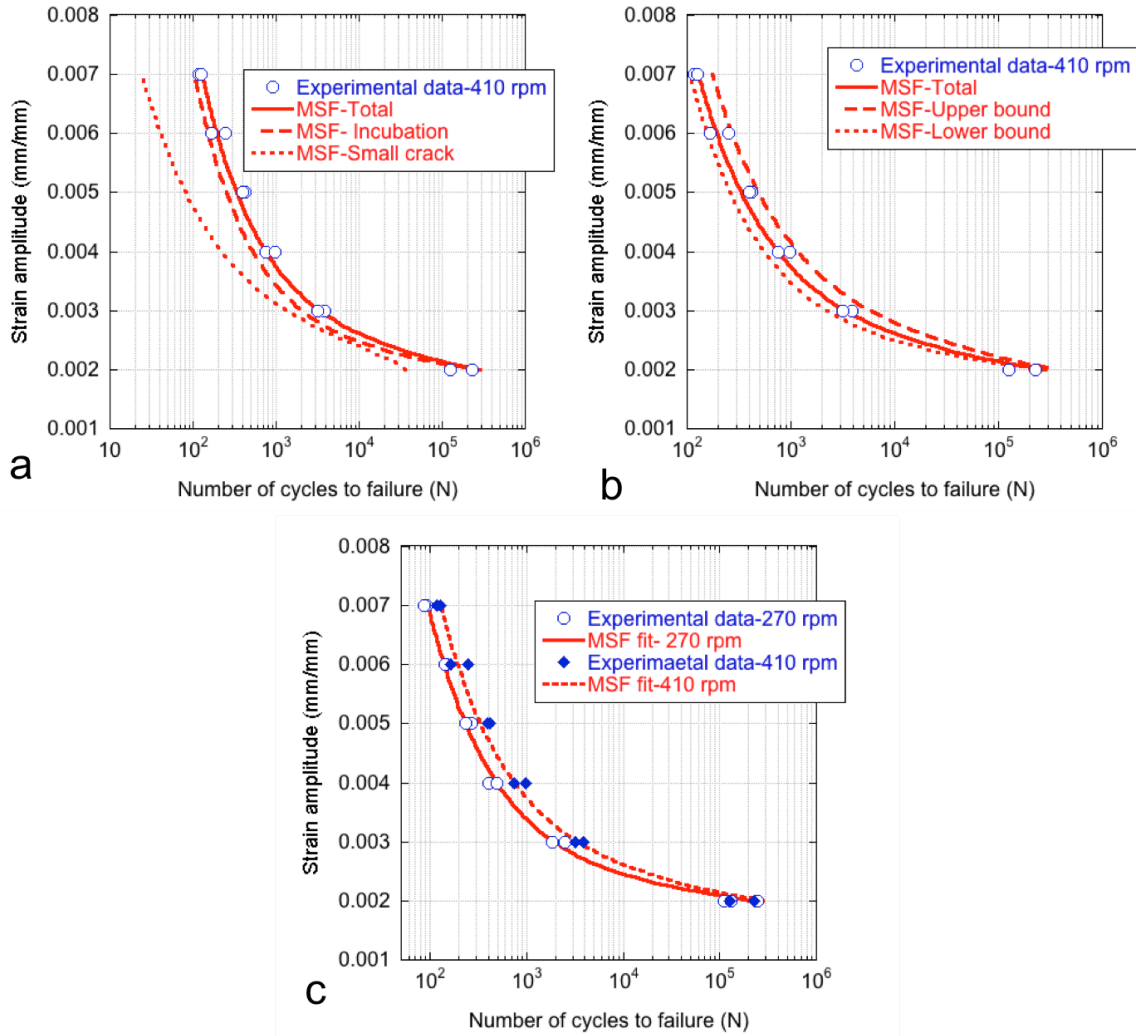


**Figure 3-12. MSF model fit for the dissimilar FSW of AA6061-to-AA7050 at a tool rotational speed of (a-b) 410 rpm. (b) The upper bound and lower bounds were obtained using the maximum (16.7  $\mu\text{m}$ ) and minimum (1.1  $\mu\text{m}$ ) particle diameters measured in the failure location (TMAZ/HAZ) of the AA6061 side. (c) Comparison of the MSF fit obtained between two rotational speeds (270 and 410 rpm).**

The MSF model for the fatigue life prediction of the dissimilar FSW of AA6061-to-AA7050 is shown in Figure 3-12. The MSF correlation was determined by including the

microstructural features such as the grain size and the diameter of the secondary particles in the TMAZ/HAZ of the AA6061, which is the location that coincides with the crack path. In addition, parameters related to cyclic mechanical behavior were obtained from using the standard strain-life approach. Figure 3-12a shows the MSF model prediction of the incubation and small crack (PSC/MSC) behavior for the dissimilar joint. In general, the majority of the fatigue life of the dissimilar weld is dominated by incubation, especially in the low strain amplitudes ( $<0.2\%$ ). At higher strain amplitudes ( $>0.3\%$ ), the fatigue life of the weld comprises both incubation and crack growth. In fact, the contribution of the small crack growth to the fatigue life increased from 20% to 40% for the strain amplitude of 0.7% and 0.3% respectively. However, a substantial decrease occurred at the low strain amplitude (0.2%), where incubation is the dominant stage. It also has to be considered that at 0.2% strain amplitude, a large amount of cyclic hardening was observed until the material stabilized and demonstrated nearly elastic behavior as shown in the hysteresis loop in Figure 3-6a. This suggests that a large portion of the fatigue life was consumed in the cyclic hardening and incubation of the crack. Furthermore, the upper and lower bound of the MSF model for the fatigue life prediction of the dissimilar FSW of AA6061-to-AA7050 are presented in Figure 3-12b. The MSF fit for the upper and lower bounds were calculated by including the minimum (1.1  $\mu\text{m}$ ) and maximum (16.7  $\mu\text{m}$ ) particle diameters measured in the location of the crack propagation of the dissimilar weld, which in fact corresponds to the TMAZ/HAZ of the AA6061 side. The models for the lower and upper bounds represent a good correlation by capturing the variation observed in that fatigue results. Lastly, Figure 3-12c presents a comparison of the experimental results and the MSF fit for the low and high tool

rational speeds corresponding to 270 and 410 rpm, respectively. This demonstrates the effectiveness of the MSF model for the life prediction of the dissimilar FSW materials.

### 3.5 Summary and Conclusions

The low cycle fatigue properties of the dissimilar welding of the heat treatable AA6061 and AA7050 high strength aluminum alloys were presented in this study. Failure was observed at the HAZ/TMAZ for all the tested conditions. Close inspection of the fractured surfaces revealed crack initiation sites at the surface of the specimen, possibly from near surface secondary intermetallic particles. As for the fatigue properties, the results revealed an increase in the strain hardening properties as well as the fatigue life as the tool rotational speed was increased. At large total strain amplitudes ( $>0.3\%$ ), the strain hardening progressed continuously until failure, however, at  $0.2\%$  strain amplitude, the plastic strain decreased until it was almost negligible before failure occurred. Inspection of the hysteresis loops demonstrated that at such low strain amplitudes, the plastic strain decreased continuously until it was null, at this point a nearly elastic behavior was observed from the hysteresis loops. Lastly, a microstructure sensitive multistage fatigue model (MSF) was implemented for the prediction of the fatigue life of the dissimilar joint. The model was successfully calibrated for the fatigue prediction of the dissimilar joint. The upper and lower bounds were calculated by considering the microstructural features existing in the location of failure of the welds such as grain size and secondary intermetallic particles.

## CHAPTER 4

### CORROSION EFFECTS ON THE FATIGUE LIFE OF DISSIMILAR FRICTION STIR WELDING OF HIGH STRENGTH ALUMINUM ALLOYS

#### 4.1 Abstract

This work presents a study on the effects of corrosion defects on the low cycle fatigue performance of dissimilar friction stir welded AA6061-to-AA7050. Corrosion defects were produced on the crown surface of the weld by static immersion in 3.5% NaCl for various exposure times. Results revealed localized corrosion damage in the thermo-mechanically affected and heat affected zones. The corrosion damage featured general pitting, pit clustering and exfoliation, revealing increasing depth with increasing exposure time. The highest corrosion attack was measured in the AA7050, which can be attributed to the highest corrosion susceptibility of this alloy when compared to the AA6061. Results demonstrated a decrease in the fatigue life, with evidence of crack initiation at the corrosion defects; however, the fatigue life was nearly independent of the exposure time. This can be attributed to total fatigue life dominated by incubation time. Furthermore, two types of failure were observed, crack propagation in the AA6061 side at high strain amplitudes ( $>0.3\%$ ), and crack propagation in the AA7050 side at low strain amplitudes ( $<0.2\%$ ). This can be attributed to the cyclic strain hardening evolution and the localized high stress field at the tip of the corrosion defect. Lastly, a microstructure-sensitive fatigue model was employed to capture the effect of corrosion defects for the life prediction of the dissimilar friction stir welded AA6061-to-AA7050.

## 4.2 Introduction

Aluminum alloys are well known to have excellent corrosion resistance, which is achieved by the formation of a protective oxide film when exposed in atmosphere. However, these alloys are also susceptible to localized corrosion when exposed to corrosive solutions such as that containing chloride ions [95]. Furthermore, welded aluminum structures are known to be susceptible to localized corrosion due to their thermal history. For the case of friction stir welded (FSWed) aluminum alloys, studies have reported localized corrosion damage, particularly in the thermo-mechanically affected zone (TMAZ) and the heat affected zone (HAZ) [48–54]. During FSW, the microstructure surrounding the nugget region is sensitized due to the dissipated excess heat. The increase in temperature leads to a precipitation widening and coarsening, which in fact leads to the formation of the microstructure characteristic of the HAZ and TMAZ, and to a reduction in the corrosion resistance of these regions due to the decreased breakdown potential [96]. The corrosion damage can be presented in the form of pitting, intergranular corrosion and environmentally induced cracking [95]. Furthermore, the formation of such corrosion defects could potentially have detrimental effect in the mechanical properties of the alloys, decreasing the service life and the safety of the structure in use. Therefore, the development of models and strategies for the fatigue life prediction is critical for the safety of aluminum aging structures exposed to corrosive environments.

It is known that the fatigue life of a structure can be affected by environmental factors including whether it is exposed to a corrosive atmosphere during service, the service temperature and type of loading. In many cases, the combination of a cyclic load and a corrosive atmosphere can lead to corrosion fatigue. Both processes can act simultaneously, inducing a more severe

damage compared to if each process occurred alone [97]. However, the synergistic effects of both process results in very complex mechanisms that are still not well understood. Many studies have opted for studying the both process independently. For example, various investigations have focused in modeling the fatigue life of different alloys by induction corrosion defects (i.e. surface pitting) in a predetermined region prior to loading, and then incorporating linear elastic fracture mechanics (LEFM) for the modeling of the crack growth [98–105]. Several studies have incorporated the software packages AFGROW [72,97,98,101] and FASTRAN [106]. For example, Burns et al. [98] implemented the AFGROW model for the fatigue life prediction of AA7075-T651 in the presence of induced corrosion defects. However, for the case of friction stir welded structures, there is very limited work done in implementing models for the fatigue life prediction in the presence of corrosion defects. For example, Ghidini et al. [72] used the software AFGROW for the fatigue life prediction of pre-corroded FSWed AA2024-T3. The results from the study showed good agreement between the model and the experimental data [72].

The aim of the current study is to extend the research on modeling the fatigue behavior of FSWed dissimilar materials, and to incorporate the effects of the presence of corrosion damage in an attempt to develop material models for the prediction fatigue life. The low cycle fatigue behavior of pre-corroded dissimilar FSWed AA6061-to-AA7050 is presented, and the microstructural sensitive the multistage fatigue model (MSF) developed by [82] is extended for the fatigue life prediction of the joints in the presence of corrosion damage. To the best of author's knowledge, this is the first study on the fatigue performance of pre-corroded dissimilar FSW of AA6061-to-AA7050 Al alloys.

### 4.3 Materials and Experiments

Butt friction stir welds were produced using 5 mm thick rolled plates of AA6061-T6 and AA7050-T7451. All samples were fabricated by The Edison Welding Institute, located in Ohio. Three different material configurations were evaluated including dissimilar FSWed of AA6061-to-AA7050, and the similar FSWed of AA6061-to-AA6061 and AA7050-to-AA7050. The butt friction stir welding was performed parallel to the rolling direction, using pre-determined welding parameters as summarized in **Table 4-1**. A cylindrical threaded tool, having a pin and shoulder diameter of 10 mm and 18 mm respectively, was used for this study.

**Table 4-1. FSW process parameter and material configuration used for this study.**

<b>Material configuration</b>	<b>Tool rotational speed (rpm)</b>	<b>Tool transverse speed (mm/min)</b>	<b>Time-static immersion in 3.5% NaCl</b>
AA6061-AA7050*	410	114.3	30 and 45 days
AA6061-AA6061	460	205.4	30 and 45 days
AA7050-AA7050	360	152.4	15 and 30 days

\*AA7050 fixed in the advancing side.

After the welding was completed, the top and bottom surfaces of the welded plates were machined down to a 4 mm of thickness. This was done to eliminate the stress raisers produced due to the flash material at the crown surface of the weld. Afterwards, specimens for

microstructural and mechanical characterization were cut perpendicular to the welding direction by using a water jet cutting. Microstructural characterization of the welds was carried out using optical (OM) and scanning electron microscopy (SEM). The cross-sections of the welds were prepared using conventional metallographic techniques. Samples corresponding to the FSWed AA6061-to-AA7050 and FSWed AA6061-to-AA6061 were etched for 60 seconds in a solution consisting of 1g NaCl and 50mL H<sub>3</sub>PO<sub>4</sub> dissolved in 125mL of ethanol, followed by a 5 seconds step using Wecks's tint (4 g of KMnO<sub>4</sub> and 1 g of NaOH dissolved in 100 ml of distilled water). On the other hand, the samples corresponding to the FSWed AA7050-to-AA7050 were etched using Keller's etching. The optical micrographs of the macrostructure of the welds corresponding to the crown (top) surfaces and the cross-section of the welds are shown in Figure 4-1.

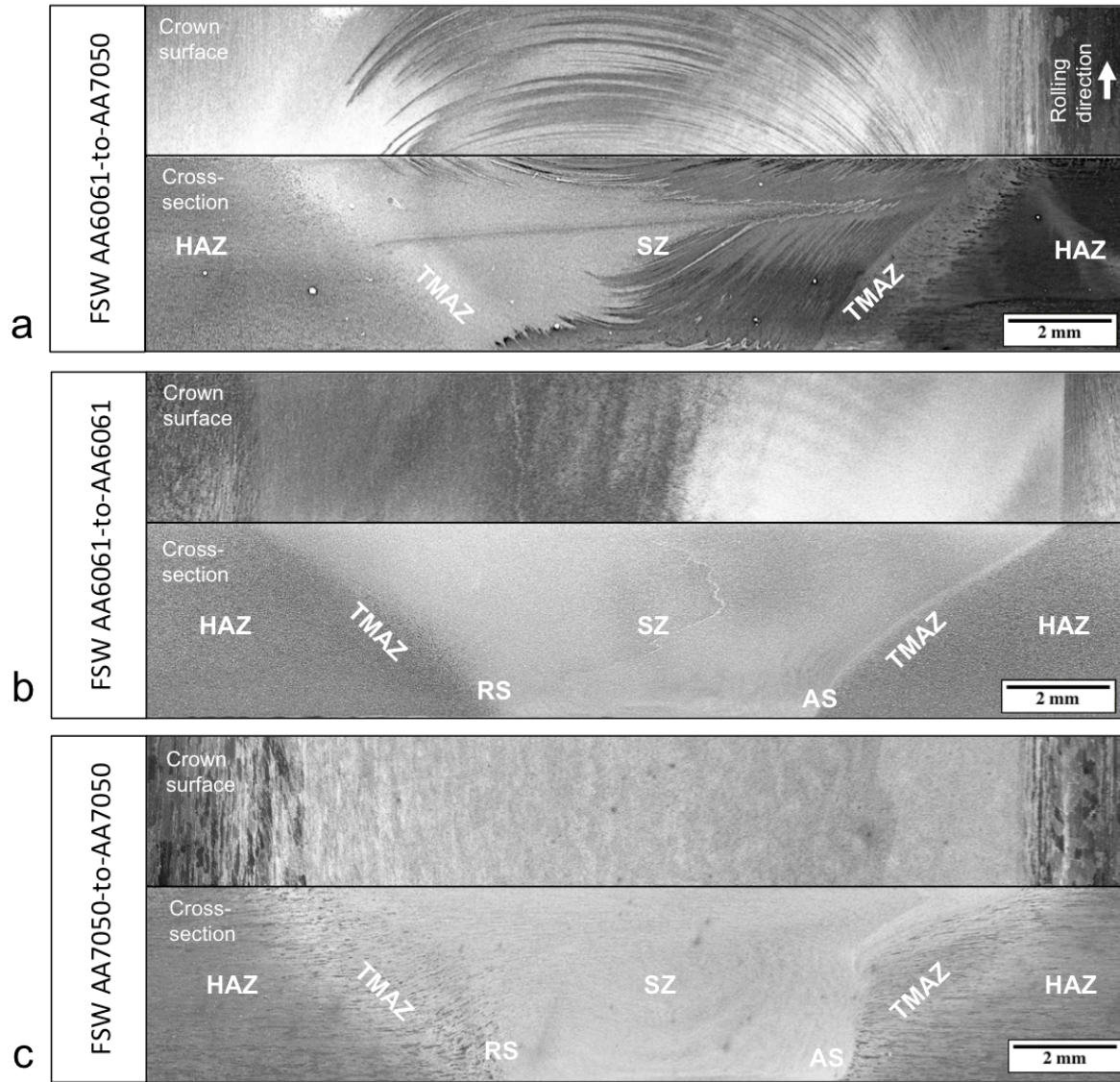


**Figure 4-1. Optical micrograph showing the typical crown (top) surface and the cross-sections for the FSWed (a) AA6061-to-AA7050 (b) AA6061-to-AA6061 and (c) AA7050-to-AA7050.**

The samples used in the pre-corrosion fatigue test were prepared following the ASTM E8 and cut perpendicular to the welding direction. The gage section was cut to a final width of 6 mm, a thickness of 4 mm and length of 50.8 mm. Prior to any testing, samples were hand

polished using silicon carbide paper up to 1200 grit. Subsequently, the samples were coated with a protective rubber layer; only the top surface of the weld was allowed to be unprotected for further corrosion exposure (Figure 4-2). The exposed surface consisted of a 30 mm x 3 mm area, with only the crown surface of the weld and a portion of the TMAZ/HAZ from the advancing (AS) and retreading side (RS) exposed. All samples were cleaned and decreased in deionized water and ethanol before and after been coated. Afterwards, all the samples were exposed to 3.5% NaCl aqueous solution in static immersion for a specific period of time determined based on preliminary testing (Table 4-1). The pH of the solution was monitored daily, measurements varied between 6.5 and 7.5 pH. The aqueous solution was replaced every 15 days. After corrosion exposure, all samples were rinsed in deionize water and ethanol, and dried in air.

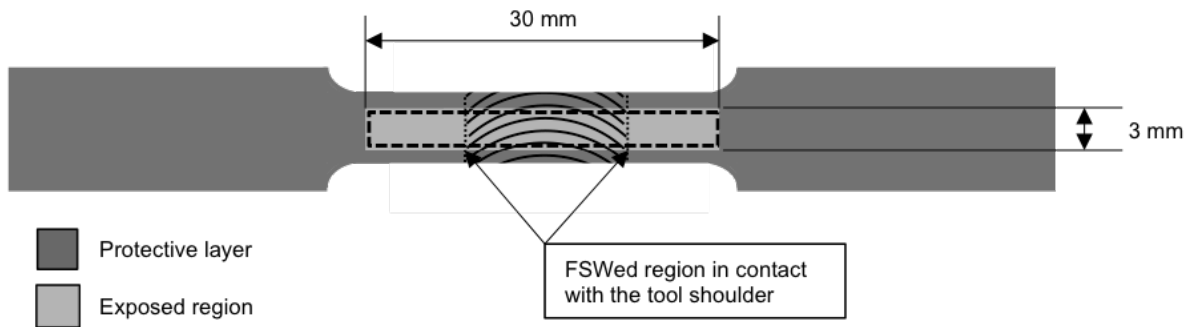


**Figure 4-2. Schematic representation of the sample preparation for the pre-corroded fatigue test.**

After exposure to the corrosive solution, the surfaces of all the pre-corroded welds were characterized prior to mechanical testing using optical microscopy. Subsequently, fatigue testing was performed in fully reversed ( $R=-1$ ) strain control condition at 5 Hz using a servo hydraulic tensile test frame. Testing was conducted at room temperature ( $\sim 21^{\circ}\text{C}$ ) and relative humidity

varying from 30 to 40%. The strain amplitude was varied between 0.6 and 0.2% strain, and testing was performed in duplicates. Fatigue failure was defined when the maximum cycle load dropped by 50%. Post-mortem fractography was performed using optical and scanning electron microscopy.

## 4.4 Results and Discussion

### 4.4.1 As welded microstructure

The macrostructure for the crown surfaces and the cross-sections of the FSWed of AA6061-to-AA7050, AA6061-to-AA6061 and AA7050-to-AA7050 are shown in Figure 4-1a-b. For the dissimilar FSWed AA6061-to-AA7050 (Figure 4-1a), the material in the right-hand-side (AS) of the joint corresponds to the AA7050, while the material in the left-hand-side (RS) corresponds to the AA6061. Three main regions can be clearly distinguished, corresponding to the SZ, the TMAZ, and the HAZ. The base materials comprise elongated grains, ~100 and ~20  $\mu\text{m}$  in horizontal and vertical directions. The microstructure in the SZ was significantly refined (<10  $\mu\text{m}$ ) when compared to the base material. On the other hand, the TMAZ features large grains and subgrains that is evidence of partial mechanical deformation undergone in this area. In addition, the microstructure of the base material and the welding regions features Al-Si-Fe and Al-Fe-Cu coarse intermetallic particles corresponding to the AA6061 and AA7050 (Figure 4-3). Similar characteristics are observed in the FSWed AA6061-toAA6061 (Figure 4-1b) and AA7050-toAA7050 (Figure 4-1c).

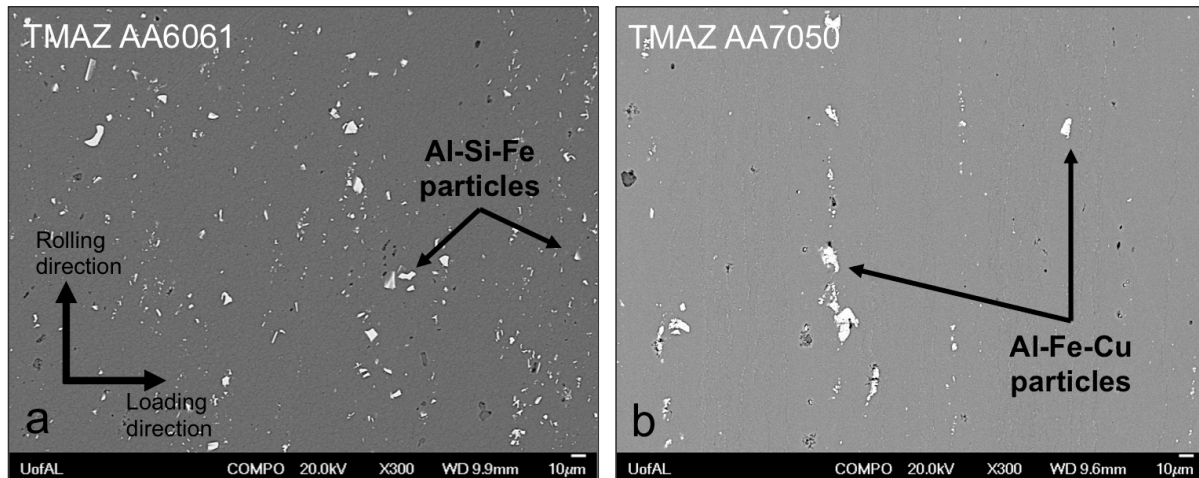


**Figure 4-3. SEM backscatter micrograph showing the location of the secondary intermetallic parties located in the TMAZ corresponding to the (a) AA6061 and the (b) AA7050. This micrographs were obtained from the crown surface of the weld.**

#### 4.4.2 Pre-corroded FSW

##### 4.4.2.1 FSWed AA6061-to-AA7050

The corrosion damage induced in the FSWed AA6061-to-AA7050 after 30 days of static immersion in 3.5% NaCl aqueous solution is shown in the Figure 4-4. As can be seen, severe corrosion attack occurred in the AA7050 side, whereas slight pitting attack was observed in the AA6061 side. Further examination of the surface revealed that the severe corrosion damage on the AA7050 side initiated at approximately 8 mm from the center of the weld and extends towards to base material. This region coincides with the TMAZ/HAZ. In addition, a dark layer is observed on top of the regions mainly composed on the AA7050 alloy, extending along the top surface of the stir zone (SZ), but not observed in the AA6061 side.

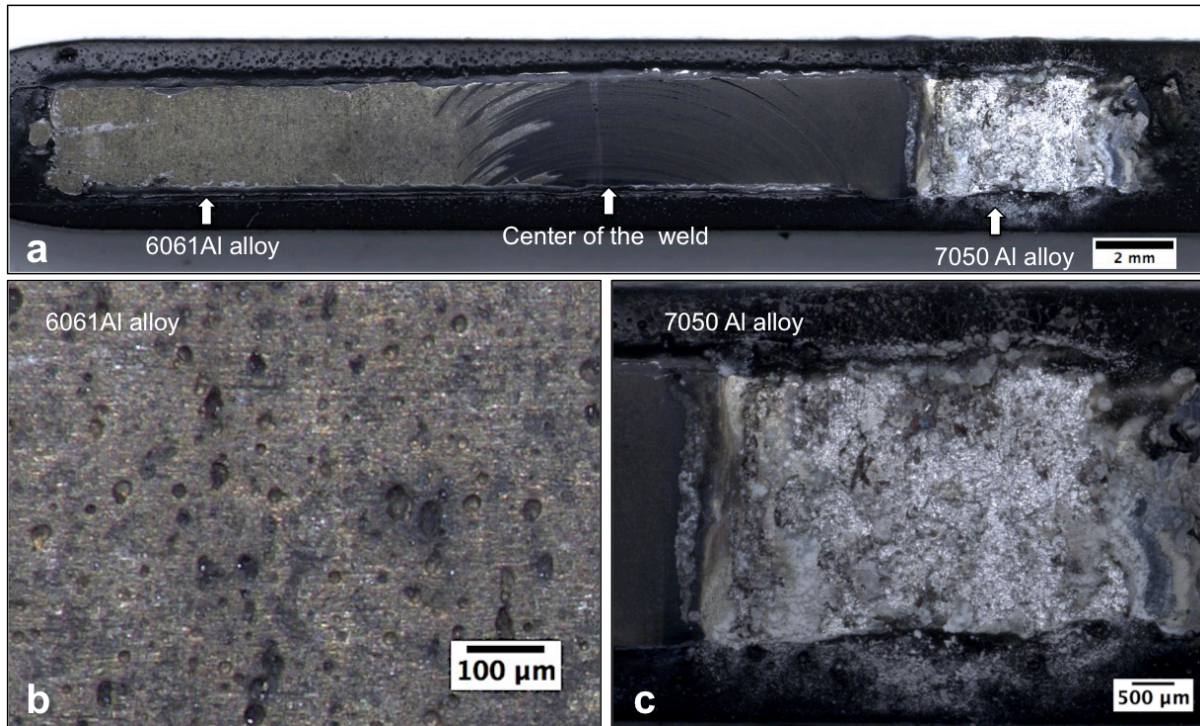


**Figure 4-4. (a) Corrosion damage produced in the FSWed AA6061-to-AA7050 after 30 days of static immersion in 3.5% NaCl aqueous solution. (b) Pitting damage in the AA6061 side. (c) Severe corrosion damage extending from the beginning of the TMAZ towards to base AA7050 base material.**

The extent of corrosion damage was measured by metallographic examination of the cross-sections of the pre-corroded FSWed AA6061-to-AA7050. Figure 4-5a and Figure 4-5b present the observable differences in corrosion resistance between AA6061 and AA7050 alloys. As stated before, slight pitting attack was observed, in the AA6061 side, whereas severe corrosion damage was observed in the AA7050. Optical examination of the cross sections demonstrated that the corrosion damage increased with the increasing exposure time for both materials. The maximum pit depth of 13.42 and 16.18  $\mu\text{m}$  after the 30 and 45 days of exposure respectively, was measured from the cross-section of the AA6061 side. On the other hand, a

maximum depth of 231.47 and 277.84  $\mu\text{m}$  for 30 and 45 days of exposure respectively, measured in the AA7050 side. Figure 4-5c and Figure 4-5d shows a magnified SEM image of the corrosion damage observed from the top view. Corrosion pits on the AA6061 side were observed to be distributed across the whole exposed area of AA6061. On the other hand, severe corrosion damage on the 7050 Al alloy was characterized by anodic dissolution, mainly in the TMAZ /HAZ of the exposed area.

#### 4.4.2.2 FSWed AA6061-to-AA6061

The pre-corroded crown surface for the FSWed AA6061-to-AA6061 is shown in Figure 4-6. The surface features corrosion pits evenly distributed across the surface. The RS demonstrated more aggressive corrosion attack when compared to the AS. Metallographic examination of the cross-section only revealed corrosion pits of approximately 10 to 20  $\mu\text{m}$  in depth. However, the examination of the fracture surface after fatigue test revealed that the fractures initiated from corrosion pits with of larger depths. The extent of the corrosion damage on the FSWed AA6061-to-AA6061 measured from the fractography is discussed later.

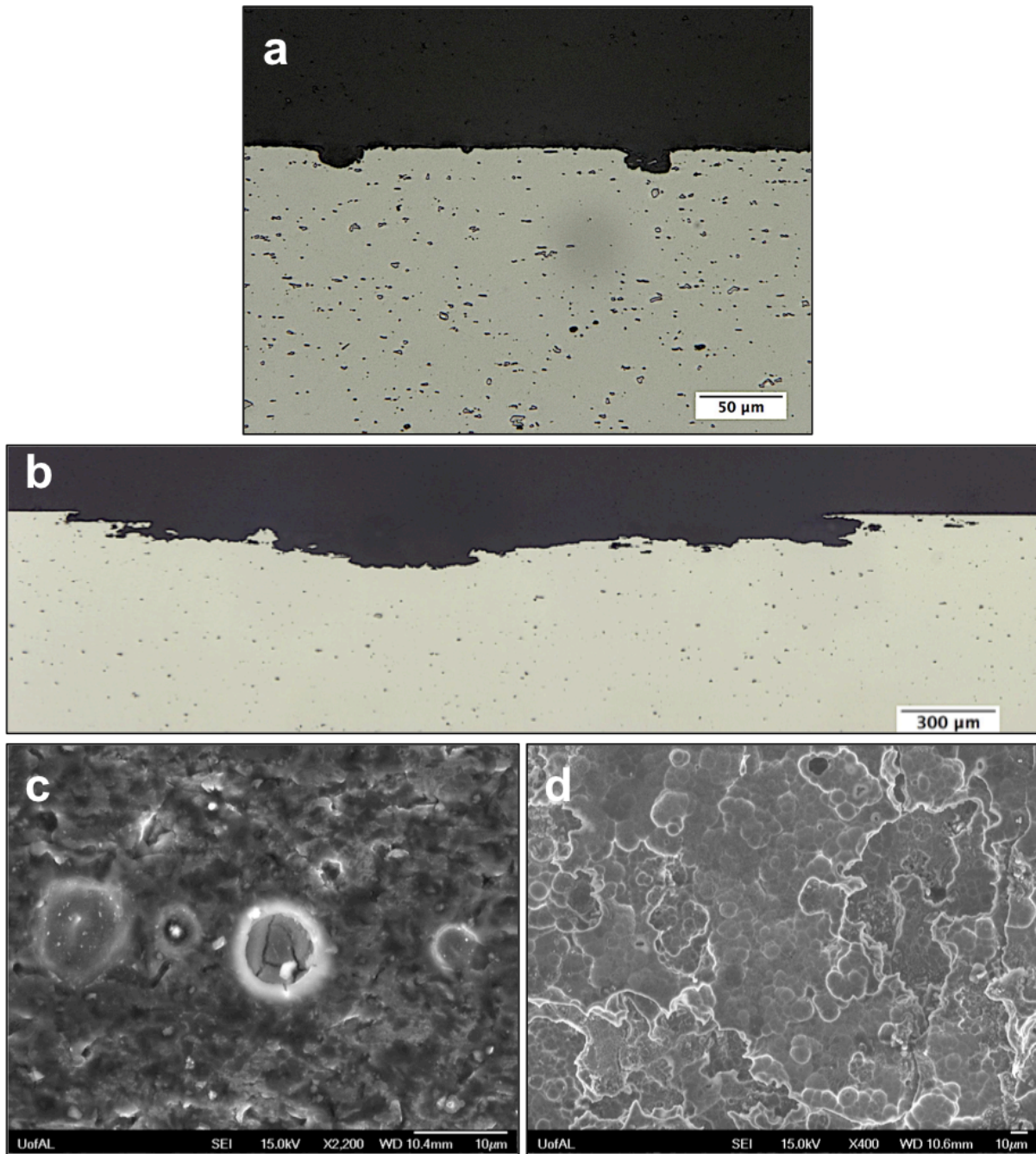


**Figure 4-5. (a) Cross-section showing the corrosion pits observed in the AA6061 side and (b) the severe corrosion damaged observed in the AA7050 side. Magnified SEM micrograph showing the corrosion damage on the (c) AA6061 and in the (d) AA7050 side.**

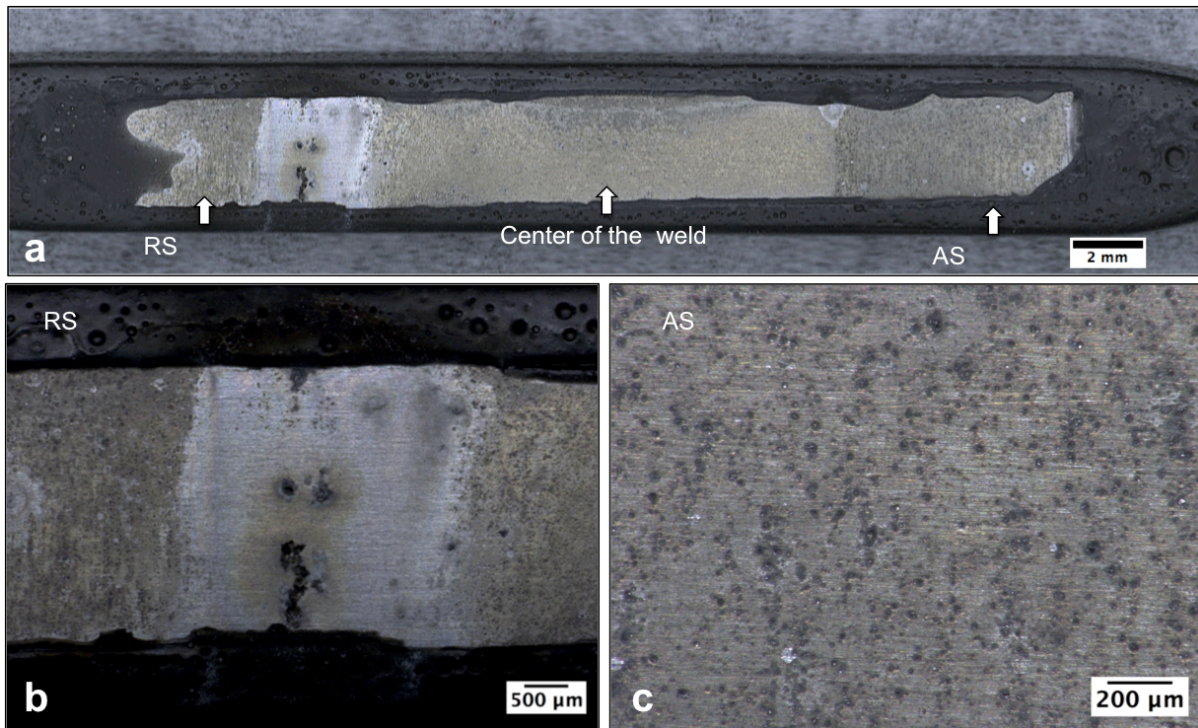


**Figure 4-6. (a) Corrosion damage produced in FSWed AA6061-to-AA6061 Al alloy after 30 days of static immersion in 3.5% NaCl aqueous solution. (b) Cross section showing the severe corrosion damage observed in the advancing side.**

#### 4.4.2.3 FSWed AA7050-to-AA7050

Figure 4-7 shows the corrosion damaged observed in the FSWed AA7050-to-AA7050 Al FSW after 30 days of exposure. In this case, the corrosion damage also extended from the TMAZ to approximate 4 mm towards the base material. The rest of the surface reflected less corrosion damage, whereas a change in color was observed (black layer). The depth of the corrosion attack was measured from the cross-sections of the welds. Results revealed that the larger corrosion depths in the retreating side (RS) when compared to the advancing side (AS). A maximum damage of 153.4 and 166.9 μm was measured in the RS for 15 and 30 days, respectively. On the

other had, a maximum corrosion damage of 109.7 and 151.6  $\mu\text{m}$  was measured for the AS after 15 and 30 days of exposure, respectively. It is known that intermetallic secondary particles play an important role on the corrosion susceptibility of Al alloys. Also, researchers have reported that a major volume of these particles are often found in the retreating side of the weld [107], therefore this could explain the differences in the corrosion damage when comparing both, the AS and RS. The depth of the corrosion damage measured from the fracture surface will be discussed later in this manuscript.

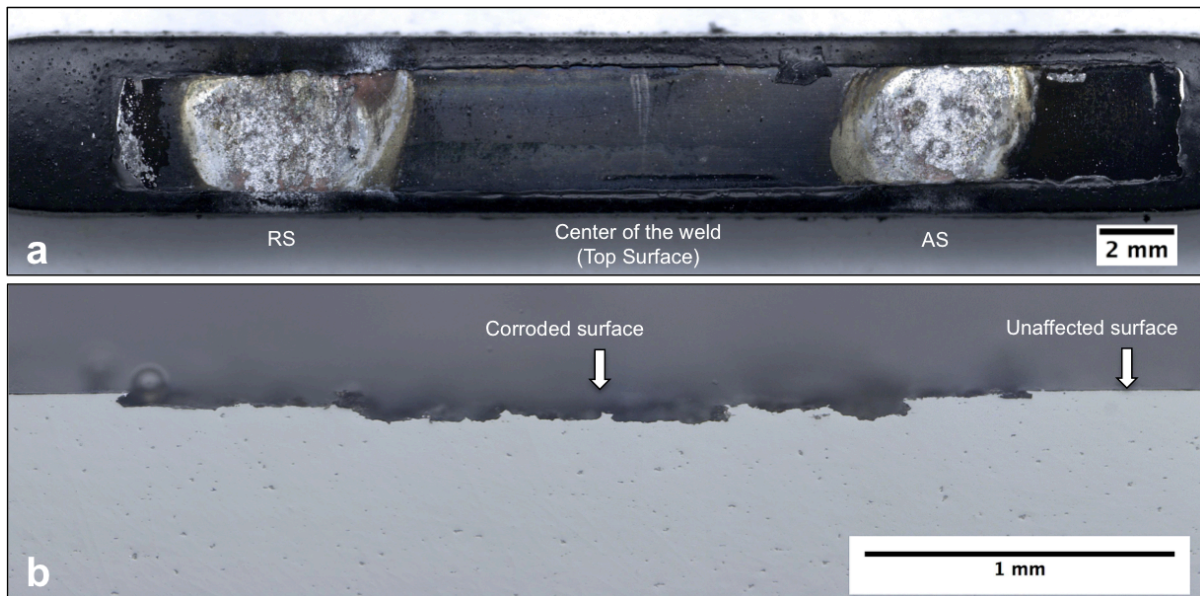


**Figure 4-7. (a) Corrosion damage produced in FSWed AA7050-to-AA7050 after 30 days of static immersion in 3.5% NaCl aqueous solution. (b) Cross-section showing the severe corrosion damage observed in the advancing side.**

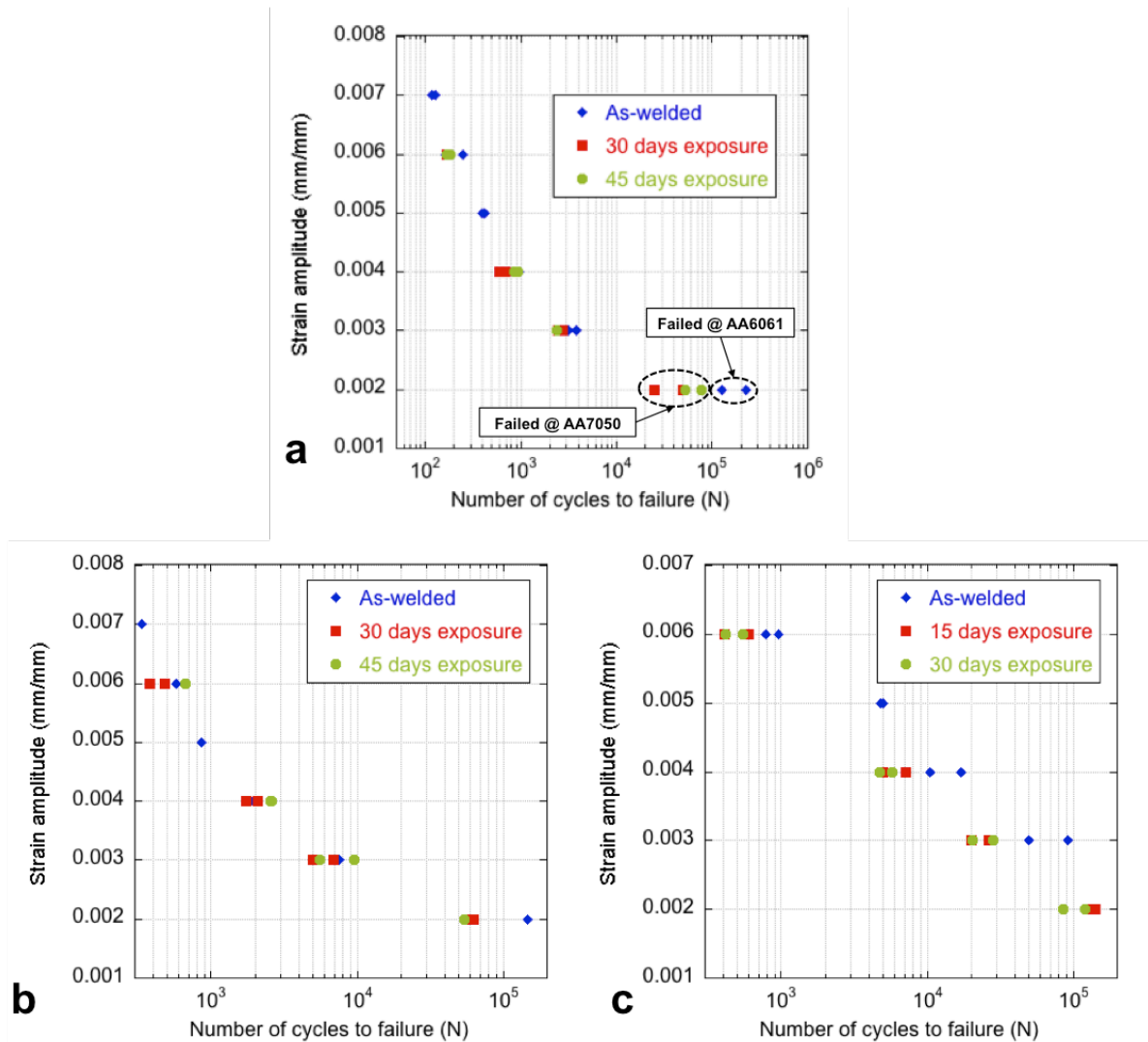
#### 4.4.3 Fatigue Testing of Pre-corroded FSW

Figure 4-8 presents the results for the fatigue test performed to the pre-corroded FSWed AA6061-to-AA7050 (Figure 4-8a), AA6061-to-AA6061 (Figure 4-8b) and AA7050-to-AA7050 (Figure 4-8c). As stated earlier, fatigue test was performed in the pre-corroded samples for the various material combinations presented in this study. Fully reversed ( $R=-1$ ), strain controlled tests were carried out at room temperature in a servo hydraulic frame. The strain amplitude was varied from 0.6% to 0.2% strain, and the tests were conducted in duplicates. In general, the fatigue results revealed a decrease fatigue life of the joints when tested after static immersion in 3.5% NaCl, however, the effects of the corrosion damage on the fatigue life were more prominent in the FSWed AA7050-to-AA7050 when compared to the other two configurations (FSWed AA6061-to-AA7050 and AA6061-to-AA6061). The mechanisms of failure for each of the three cases will be discussed in the following sections.

##### 4.4.3.1 Fatigue of FSWed AA6061-to-AA7050

The fatigue results for the FSWed AA6061-to-AA7050 in the as-welded and pre-corroded conditions are shown in Figure 4-8a and summarized in Table 4-2. For the as-welded condition, the failure mode was dominated by the material with the lowest strength, as in this case the AA6061. However, for the pre-corroded dissimilar joint, two types of failure were observed, the first occurring at the TMAZ/HAZ of the AA6061 side and the second occurring at the TMAZ/HAZ of the AA7050 (Figure 4-8a and Figure 4-9). Despite that metallographic examination of the pre-corroded cross-sections revealed much more severe corrosion damage in the AA7050 side, the majority of the joints failed in the TMAZ/HAZ of the AA6061 side at high

strain amplitudes ( $>0.3\%$ ). Fracture at the TMAZ/HAZ of the AA7050 occurred only at low strain amplitude (0.2% strain).



**Figure 4-8. Fatigue life results for the FSWed (a) AA6061-to-AA7050 (b) AA6061-to-AA6061 and (c) AA7050-to-AA7050 in the as-welded and pre-corroded condition for various exposure times.**

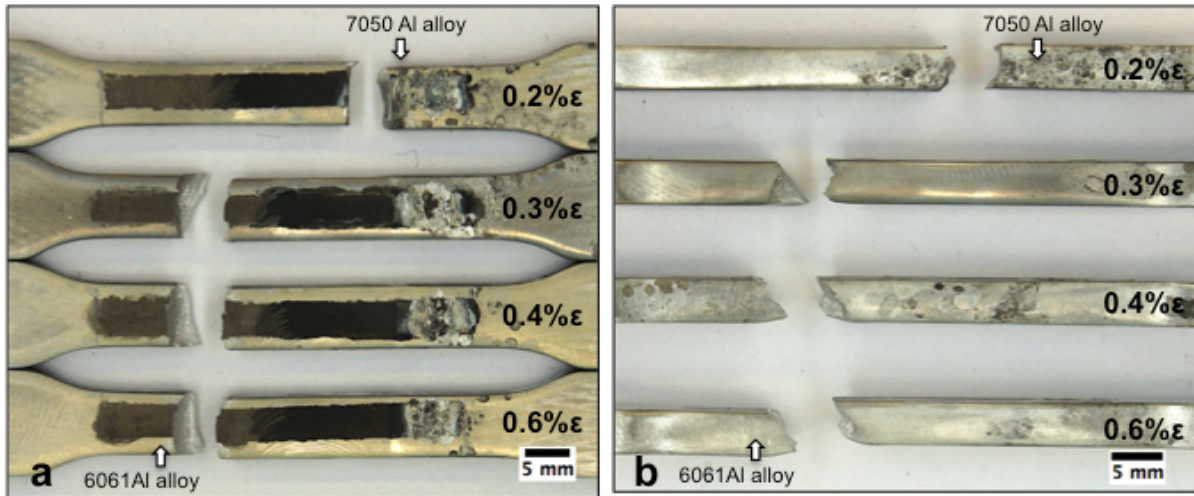


**Figure 4-9. Typical optical micrographs showing the failure locations at various strain amplitudes for the pre-corroded FSWed 6061-to-7050. (a) Top surface of the welds. (b) Surfaces parallel to the cross-section of the welds.**

Close examination of the stress amplitude and plastic strain evolution for the dissimilar FSW in the as-welded condition, provides knowledge about the mechanisms of failure. As shown on Figure 4-10a, at a strain amplitude of 0.2%, the plastic strain decreased until  $10^3$  cycles was reached, after this point the plastic strain was almost or completely negligible. Inspection of the hysteresis loops demonstrated that at such low strain amplitudes, there is an initial stage of strain hardening that constantly evolved, increasing until it reached a maximum strain hardening point, afterwards the cyclic behavior shift to a nearly perfect elastic behavior. Furthermore, in the as-welded condition, failure occurred in the TMAZ/HAZ of the AA6061, which coincides with the low hardness regions detected by microhardness measurements. It is expected that this region will undergo strain hardening during the cyclic loading until failure as demonstrated by the plastic strain evolution curves. The cyclic strain hardening of this region is more prominent at

high strain amplitudes ( $>0.3\%$ ). On the other hand, at low strain amplitude ( $0.2\%$ ), cyclic hardening constantly increased across the welded material until a uniform work hardening is reached. As this point, deformation is distributed evenly across the weld, and a higher stress field is generated in the corrosion defect of the TMAZ/HAZ of the AA7050 when compared to the AA6061. This stress field leads to fatigue crack incubation in this area and therefore to final rupture.

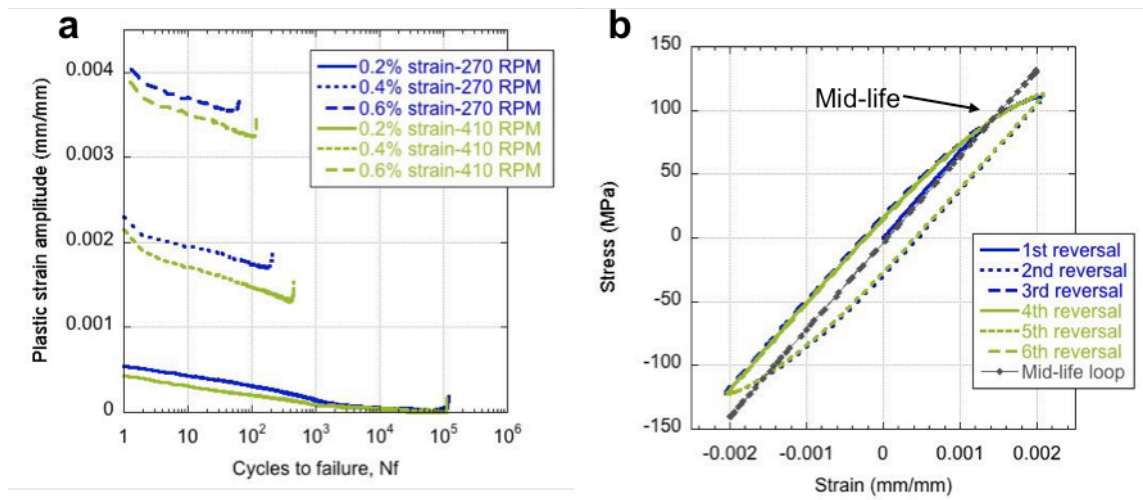


**Figure 4-10. (a) Plastic strain amplitude versus the number of cycles to failure for various strain amplitude condition and tool rotational speeds (welding parameters). Hysteresis loops for (b) 0.2% strain amplitude. All the results are for sample sin the “as-welded” condition.**

The fracture surfaces for the pre-corroded FSWed AA6061-to-AA7050 tested at 0.3 and 0.2% strain amplitude are shown Figure 4-11. Figure 4-11a-b shows the overview and magnified SEM image of the FSWed AA6061-to-AA7050 specimen tested at 0.3% strain. As seen in the overview (Figure 11a) the cracks initiated from the surfaces corresponding to the crown surface

of the weld. A magnified view of the crack initiation region (Figure 4-11b) revealed that crack initiated from the free surfaces and corrosion pits (white arrow in Figure 4-11b). As stated before, at high strain amplitude ( $>0.3\%$ ), failure was observed in the AA6061 side. Detailed examination of these samples revealed that the cracks initiated from corrosion pits located at the crown surface. This corrosion pits demonstrated an average depth of 25.2 and 27.1  $\mu\text{m}$  for an exposure time of 30 and 45 days respectively. Furthermore, as demonstrated by the pit depth measurements, the AA6061 in the dissimilar FSW demonstrated a small degree of corrosion damage. In fact the depth of the corrosion pit were very close to the diameter of the secondary Al-Si-Fe particles that are known to be sources of fatigue cracks for the base material. As such the depth of the corrosion pits was approximately 1.5 times larger that the particles. This explains why the effect of the corrosion damage was so small on the fatigue life of the joint when compared to the undamaged welds. On the other hand, the fracture surface resulted from the failure in the AA7050 at 0.2% strain amplitude (Figure 4-11c-d). As shown in the overview in Figure 4-11c, large defects were observed on the AA7050 side. These defects were produced due to the anodic dissolution of the TMAZ/HAZ region in the presence on NaCl. The corrosion damage observed in the AA7050 had a maximum depth of 368 and 382.9  $\mu\text{m}$  for an exposure time of 30 and 45 days. The depth of the corrosion damage measured from the fracture surfaces for the FSWed AA6061-to-AA7050 are summarized in Table 4-2.

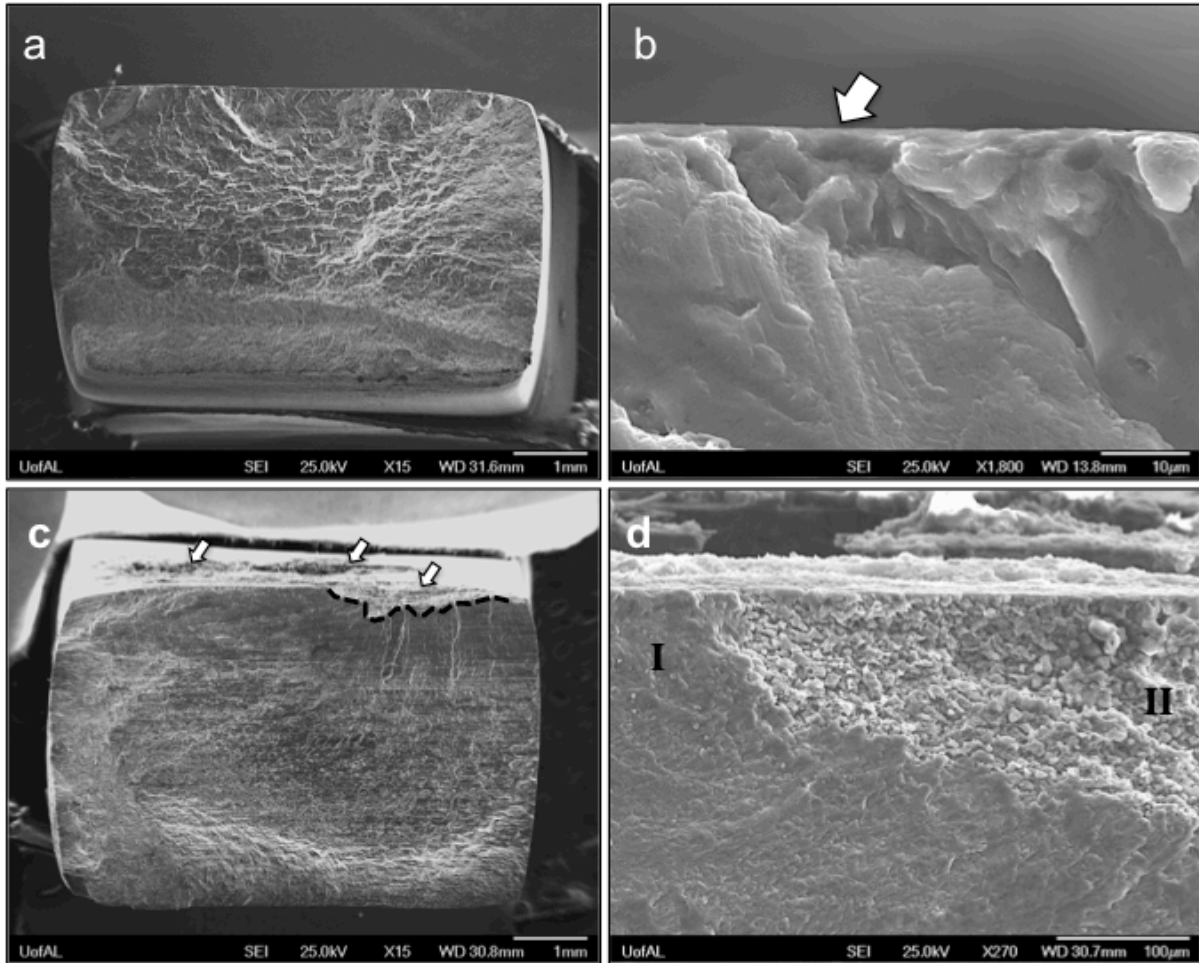


**Figure 4-11. Typical fracture surfaces of the pre-corroded FSWed AA6061-to-AA7050 for the samples tested at (a-b) 0.3% and (c-d) 0.2% strain amplitude. (b) The white arrow indicates the crack initiation site at a corrosion pit of a sample tested at 0.3% strain amplitude. This sample failed at the AA6061 Al side. (d) At 0.2% strain amplitude, the crack initiated (Region I) from the severe corrosion attack (region II) generated after 30 days of static immersion in 3.5% NaCl.**

**Table 4-2. Fatigue tests data for the pre-corroded FSWed AA6061-to-AA7050.**

30 days exposure					45 days exposure				
Sample No.	Strain amp. (%)	N (Cycles)	Corrosion	Failed at:	Sample No.	Strain amp. (%)	N (Cycles)	Corrosion	Failed at:
			damage, max depth (µm)					damage, max depth (µm)	
H15	0.4	592	22.9	AA6061	H11	0.3	2,406	22.1	AA6061
H18	0.6	167	24.0	AA6061	H13	0.6	182	40.4	AA6061
H26	0.4	688	29.1	AA6061	H16	0.4	935	26.0	AA6061
H30	0.6	175	25.2	AA6061	H20	0.4	853	22.9	AA6061
H31	0.3	2,477	30.1	AA6061	H25	0.3	2,387	20.9	AA6061
H41	0.3	2,736	20.0	AA6061	H39	0.6	167	30.1	AA6061
H06	0.2	24,754	368.0	AA7050	H30	0.2	52,529	-	AA7050
H36	0.2	50,038	182.7	AA7050	H33	0.2	76,617	383.9	AA7050
Average pit depth (µm), based on AA6061					Average pit depth (µm), based on AA6061				
25.2					27.1				

#### 4.4.3.2 Fatigue of FSWed AA6061-to-AA6061

The fatigue results for the as-welded and pre-corroded FSWed AA6061-to-AA6061 are shown in Figure 4-7b. As can be seen, at high strain amplitude (>0.3% strain) the results for the pre-corroded samples and the as-welded overlap. However, at low strain amplitude (0.2%) the differences in the fatigue life are more evident. In the as-welded condition, fatigue results

demonstrated fatigue life of up to 147,500 cycles, whereas in the pre-corroded condition, failure was observed at 59,000 cycles. These results demonstrated a reduced fatigue life of up to 60%. However, the decrease in the fatigue life between the exposure times was not significant. Figure 4-12 and Figure 4-13 show the fracture surface of the FSWed AA6061-to-AA6061 after static immersion in 3.5% NaCl. The majority of the samples failed in the RS. In fact a majority of samples failed in the RS for an exposure time of 30 days. Furthermore, 7 out of 8 samples failed in the RS after 45 days of exposure. On the other hand, the fracture surface for a sample tested 0.2% strain amplitude is shown in Figure 4-13. As shown in Figure 4-13a, cracks initiated at corrosion defects located in the crown surface of the joint. The corrosion defects consisted of cluster of corrosion pits as presented in Figure 4-13b and 4-13c. Corrosion pits with a depth varying from 83 to 260  $\mu\text{m}$  were observed. The average pit depth for both 30 and 45 days of exposure was 130.1 and 146.0  $\mu\text{m}$ , respectively. Table 4-3 summarizes the corrosion pit depth measurement for the pre-corroded FSWed AA6061-to-AA6061 obtained from the fracture surfaces.

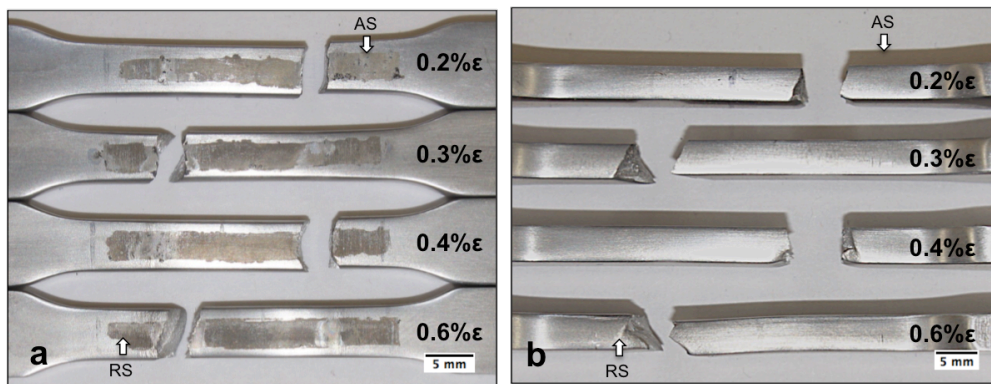


**Figure 4-12. Typical optical micrographs showing the failure locations at various strain amplitudes for the pre-corroded FSWed AA6061-to-AA6061. (a) Top surface of the welds. (b) Surfaces parallel to the cross-section of the welds.**

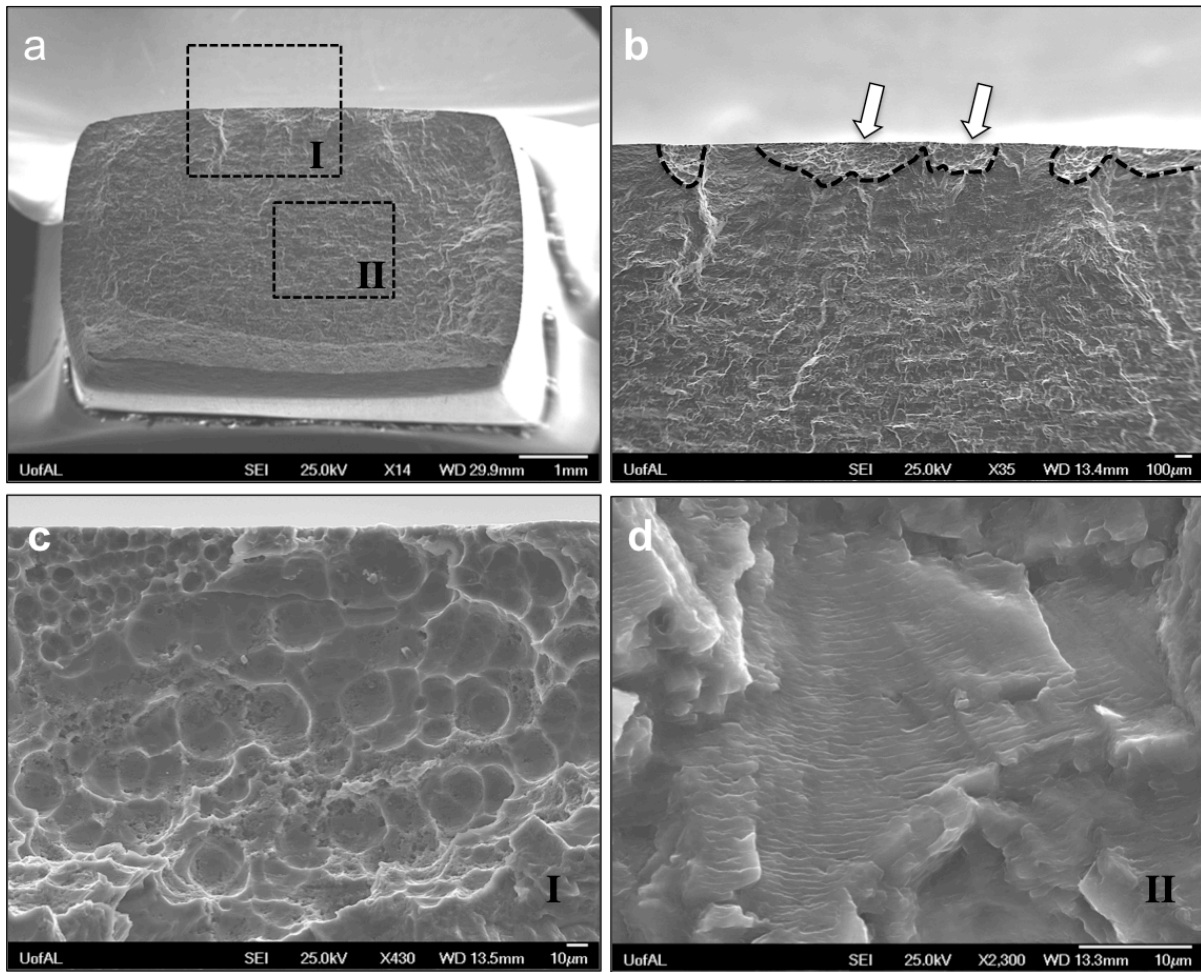


**Figure 4-13. Fracture surface of the pre-corroded FSWed AA6061-to-AA6061 samples tested at 0.2% strain amplitude and 30 days of static immersion in 3.5% NaCl. (a) Overview of the fracture surface. (b-c) Magnified view of the corrosion pits in the crown surface of the weld. (d) Typical striations on the fracture surface of the weld.**

**Table 4-3. Fatigue tests data for the pre-corroded FSWed AA6061-to-AA6061.**

30 days exposure					45 days exposure					
Sample No.	Strain amp. (%)	N (Cycles)	Corrosion damage, max depth (µm)	Failed at:	Sample No.	Strain amp. (%)	N (Cycles)	Corrosion damage, max depth (µm)	Failed at:	
H17	0.2	58,858	106.4	RS	H05	0.4	2,572	27.17	AS	
H25	0.3	4,981	160.01	RS	H07	0.2	53,855	261.33	RS	
H39	0.2	63,356	144.9	RS	H21	0.2	54,851	117.89	RS	
H49	0.4	2,093	147.2	AS	H29	0.3	9,528	106	RS	
H55	0.6	377	101.2	RS	H41	0.6	235	234.24	RS	
H71	0.4	1,752	83.0	AS	H67	0.3	5,588	74.33	RS	
H77	0.6	480	-	RS	H81	0.4	2,535	-	RS	
H85	0.3	6,951	129.9	RS	H87	0.6	668	201.33	RS	
H63	0.2	15,297	168.0	AS						
Average pit depth (µm)			130.1		Average pit depth (µm)			146.0		

#### 4.4.3.3 FSWed AA7050-to-AA7050

Figure 4-7c shows the results from the fatigue test performed in the as-welded and pre-corroded FSWed AA7050-to-AA7050. As noted earlier, the effects of corrosion damage are

more evident in this joint when compared to the dissimilar FSWed AA6061-to-AA7050 and the similar FSWed AA6061-to-AA6061. Failure occurred in both the AS and the RS (Figure 4-14). In fact 2 out of 8 samples failed in the AS after 15 days of exposure, whereas 4 out of 8 samples failed in the AS after 30 days of exposure. This suggests that despite that the larger corrosion damage was measured in the RS, the difference in damage between both sides was not large enough to allow failure to occur preferably in one side over the other (Table 4-4). On the other hand, magnified SEM images of the fracture surface are shown in Figure 4-15. This sample was tested at 0.2% strain amplitude after a 30 days immersion to 3.5% NaCl in aqueous solution. As shown in the overview (Figure 4-15a), the cracks initiated from the corrosion defects produced at the crown surface of the weld (white arrow in Figure 4-15b). In this particular case, the corrosion damage only extended approximately 97  $\mu\text{m}$  below the original undamaged surface, however it extended across the width of the exposed region. The rest of the fracture surface was characterized by striations in the stable crack growth region (Figure 4-15c-d). It important to note that detailed examination of the fracture surface revealed an average and maximum depth for the corrosion damage of 145 and 206  $\mu\text{m}$  respectively, for a 15 days exposure. On the other hand, for a 30 days exposure detailed examination of the fracture surface revealed an average and maximum depth for the corrosion damage of 174.2 and 281.6  $\mu\text{m}$  respectively. Table 4-4 summarizes the corrosion pit depth measurement for the pre-corroded FSWed AA7050-to-AA7050 obtained from the fracture surfaces.

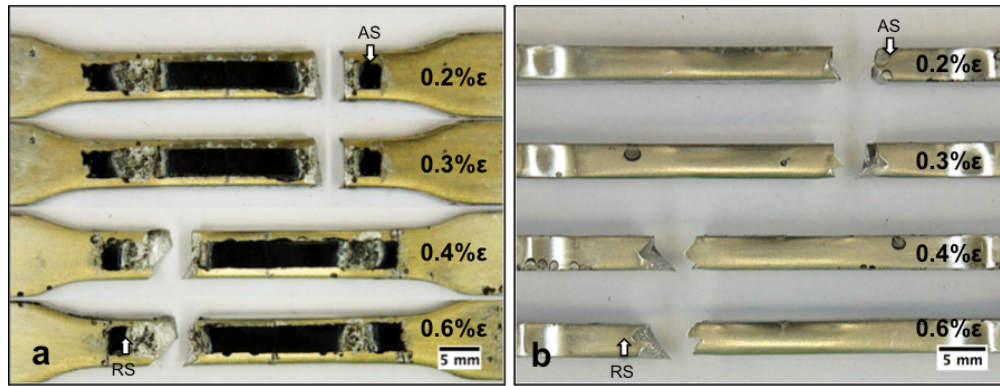


Figure 4-14. Typical optical micrographs showing the failure locations at various strain amplitudes for the pre-corroded FSWed AA705-to-AA7050. (a) Top surface of the welds. (b) Surfaces parallel to the cross-section of the welds.

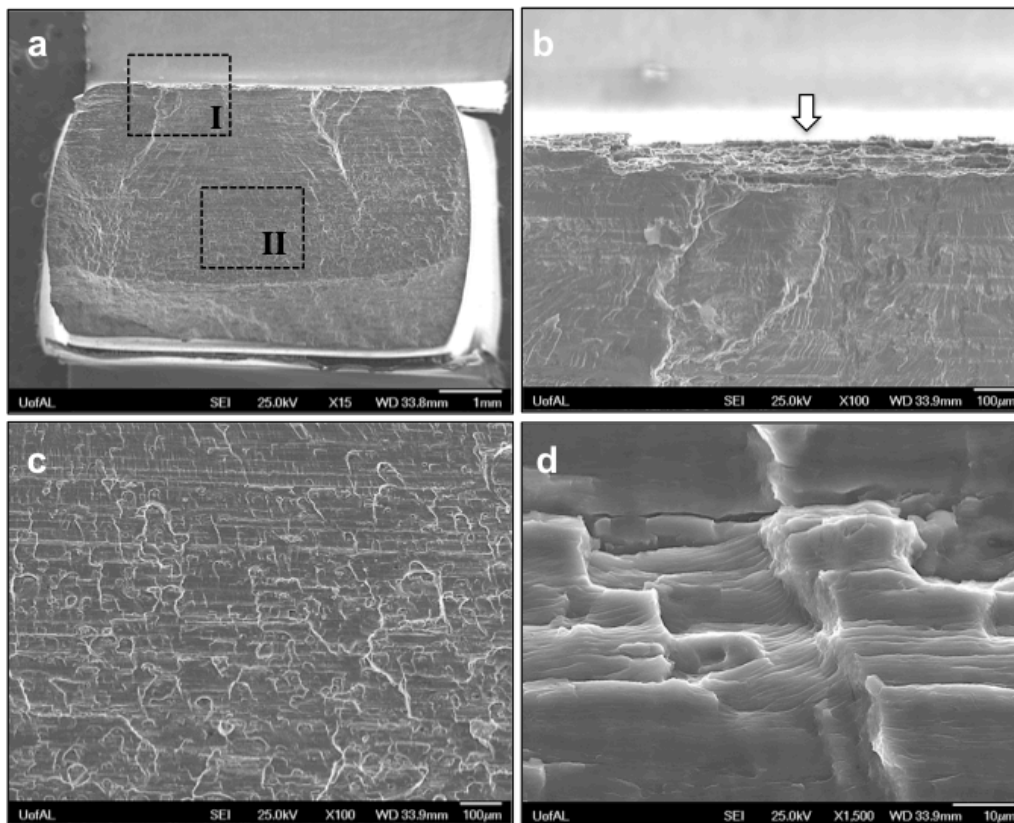


Figure 4-15. (a) Typical fracture surface of the pre-corroded FSWed AA7050-to-AA7050 for the samples tested at 0.2% strain amplitude after static immersion in 3.5% NaCl for 30

days. (b) Magnified view of the crack initiation at corrosion defects (region I). (c) Magnified view of the stable crack propagation (region II). (d) Magnified view of region II showing the striations.

**Table 4-4. Fatigue tests data for the pre-corroded FSWed AA7050-to-AA7050.**

15 days exposure					30 days exposure				
Sample No.	Strain amp. (%)	N (Cycles)	Corrosion damage, max depth (µm)	Failed at:	Sample No.	Strain amp. (%)	N (Cycles)	Corrosion damage, max depth (µm)	Failed at:
H04	0.6	410	206.1	RS	H13	0.4	4,680	162.45	AS
H12	0.2	140,873	173.0	RS	H17	0.4	5,762	169.4	RS
H16	0.4	4,971	145.8	RS	H22	0.3	20,606	281.56	RS
H18	0.3	26,412	120.5	AS	H29	0.2	121,100	144.53	AS
H21	0.6	601	152.0	RS	H42	0.6	419	209.2	RS
H28	0.3	20,121	140.6	RS	H51	0.3	28,348	138.33	AS
H41	0.2	126,517	129.0	AS	H73	0.6	546	191.66	RS
H50	0.4	7,174	93.8	RS	H81	0.2	84,903	96.73	AS
Average pit depth (µm)			147.4		Average pit depth (µm)			174.2	

#### 4.4.4 Remarks in the Corrosion Behavior of dissimilar FSWed AA6061-to-AA7050

In general, localized corrosion damage was observed in the pre-corroded samples for the various combinations of materials and exposure time. The extent of the corrosion damage was characterized by measuring the penetration depth at various exposure times. The corrosion damage featured general pitting, pit clustering and exfoliation, revealing increasing depth with increasing exposure time. The dissimilar FSWed AA6061-to-AA7050 featured corrosion pits that were evenly distributed across the surface AA6061 side of the weld. The pits were nearly on the same scale as the secondary intermetallic particles of the AA6061 base material. The AA7050 in the dissimilar weld featured severe localized corrosion damage, mainly in the TMAZ/HAZ. The corrosion damage was produced due to the anodic dissolution of the matrix, this extended in the order of a hundred microns and over. On the other hand, the FSWed AA6061-to-AA6061 featured moderated corrosion pits evenly distributed in the crown surface of the weld. However, fractography revealed pit clustering on the order of several hundreds microns, which serves as crack initiation sites. Lastly, the FSWed AA7050-to-AA7050 featured severe localized corrosion damage, in both TMA/HAZ corresponding to the AS and RS. The depth of the corrosion damages was in the range several hundred microns.

Based on the results obtained from all the material combinations, various remarkable observations can be made from the results obtained. The first includes the corrosion damage produced in the dissimilar and similar welds. For the dissimilar joint, the AA7050 demonstrated the highest corrosion depth of the two materials (AA6061 and AA7050). This can be explained by considering that the AA7050 has higher corrosion susceptibility when compared to the AA6061. However, the extent of the corrosion damage in the TMAZ/HAZ of the AA7050 in the

dissimilar weld, was roughly 1.3 times more severe than in the TMAZ/HAZ of the similar FSWed AA7050. On the other hand, for the AA6061, the depth of the corrosion damage was roughly 5 times much severe in the similar FSWed AA6061 than in the dissimilar joint (AA6061-to-AA7050). This behavior is attributed to the cathodic protection of the AA6061 in the dissimilar joint.

Lastly, as for the mechanical behavior, results revealed a decrease in the fatigue life of the joints in the presence of corrosion defects. However, the fatigue life results were nearly independent of the exposure time. These results are in agreement with other investigations [72,98], as this can be attributed to total fatigue life dominated by incubation time.

#### 4.4.5 Multistage Fatigue Modeling

One of the aims of the current study is to extend the research on modeling the fatigue behavior of FSWed materials, and to incorporate the effects of the presence of corrosion damage in an attempt to capture the effect on fatigue life. As such, the microstructural sensitive the multistage fatigue model (MSF) developed by [82] was extended for the fatigue life prediction of the joints in the presence of corrosion damage. Initially developed by McDowell and co-workers [82] for the fatigue life modeling of aluminum cast alloys, this model have been extended to other alloy systems and processing methods including Mg [83–86], Al alloys [87–90], and steels [91–93]. This model was developed to evaluate the sensitivity of fatigue response to microstructural features with the purpose of being applied for the fatigue life prediction in the design of materials and structural components. For example, the model considers the role of local constrained microplasticity at fractured inclusions and their effect in the crack incubation, and

the microstructural small crack growth [94]. Lastly, based on the dimensions of the material inclusions, the upper and lower bounds of the fatigue life can be predicted.

The fatigue damage evolution predicted by the MSF model, is divided in three main stages as

$$N_{Total} = N_{Inc} + N_{MSC/PSC} + N_{LC} \quad (5)$$

where  $N_{Total}$  is the total fatigue life, the  $N_{Inc}$  is the number of cycles required for the crack incubation,  $N_{MSC/PSC}$  and  $N_{LC}$  are the number of cycles required for the propagation of the microstructurally small/physically small crack (*MSC/PSC*), and the propagation of the long crack (*LC*) respectively.

The  $N_{inc}$  comprises the number of cycles of a crack incubating at an inclusion, particle, cluster or pore. This stage is treated in the MSF model as a microscale damage parameter in a modified Coffin-Manson law. This nonlocal parameter around the inclusion is described as  $\beta$  and is expressed by Equation 6 as

$$C_{inc} N_{inc}^{\alpha} = \beta = \frac{\gamma_{max}^{P*}}{2} \quad (6)$$

Thus,

$$C_{inc} = CNC + z(C_m - CNC) \quad (7)$$

$$CNC = C_n(1 - R) \quad (8)$$

where  $C_{INC}$  and  $\alpha$  are the coefficient and exponent values obtained for the modified Coffin-Manson law for incubation (Equation 6). On the other hand,  $C_m$  and  $C_n$  are model constants and the  $R$  and  $z$ , are the load ratio and localization multiplier (Equation 9).

$$z = \frac{\frac{l}{D} - n_{lim}}{1 - n_{lim}} \quad (9)$$

Thus,  $D$  is the size of the critical inclusion where that crack incubates,  $l$  is the size of the plastic zone in front of the inclusion, and  $n_{lim}$  is the limiting factor that defines the transition from constrained to unconstrained micronotch root plasticity.

The driving force for the propagation of the microstructurally/physically small cracks in  $N_{MSC/PSC}$ , is defined by the crack tip opening displacement and expressed as

$$\left(\frac{da}{dN}\right)_{MSC} = \chi(\Delta CTD - \Delta CTD_{th}) \quad (10)$$

where  $\Delta CTD$  is the crack tip opening displacement range,  $\Delta CTD_{th}$  ( $2.48 \times 10^{-1} \mu\text{m}$ ) is the crack tip displacement threshold,  $\chi$  is a material constant (0.32 for Al alloys), and the initial crack  $a_i$  is defined as  $0.625D$ .

The crack tip opening displacement range is defined as

$$\Delta CTD = C_{II} \left(\frac{GS}{GS_0}\right)^\omega \left(\frac{GO}{GO_0}\right)^\varpi \left[\frac{U\Delta\hat{\sigma}}{S_{ut}}\right]^\zeta a + C_I \left(\frac{GS}{GS_0}\right)^\omega \left(\frac{GO}{GO_0}\right)^\varpi \left(\frac{\Delta\gamma_{max}^p}{2}\right)^2 \quad (11)$$

where  $C_I$  is the low cycle fatigue coefficient,  $C_{II}$  and  $\zeta$  are the coefficient and exponents for the high cycle fatigue regime.  $S_{ut}$  is the ultimate tensile strength obtained from the monotonic tensile test,  $a$  is the crack length.  $GS$ ,  $GS_0$ ,  $GO$ ,  $GO_0$   $\omega$  and  $\varpi$  are model constants for grain size and

orientation. The equivalent uniaxial stress amplitude is defined by  $\Delta\hat{\sigma}$  and the means stress effects is defined by  $U$ . A detailed description of the model is presented in [82,89,94].

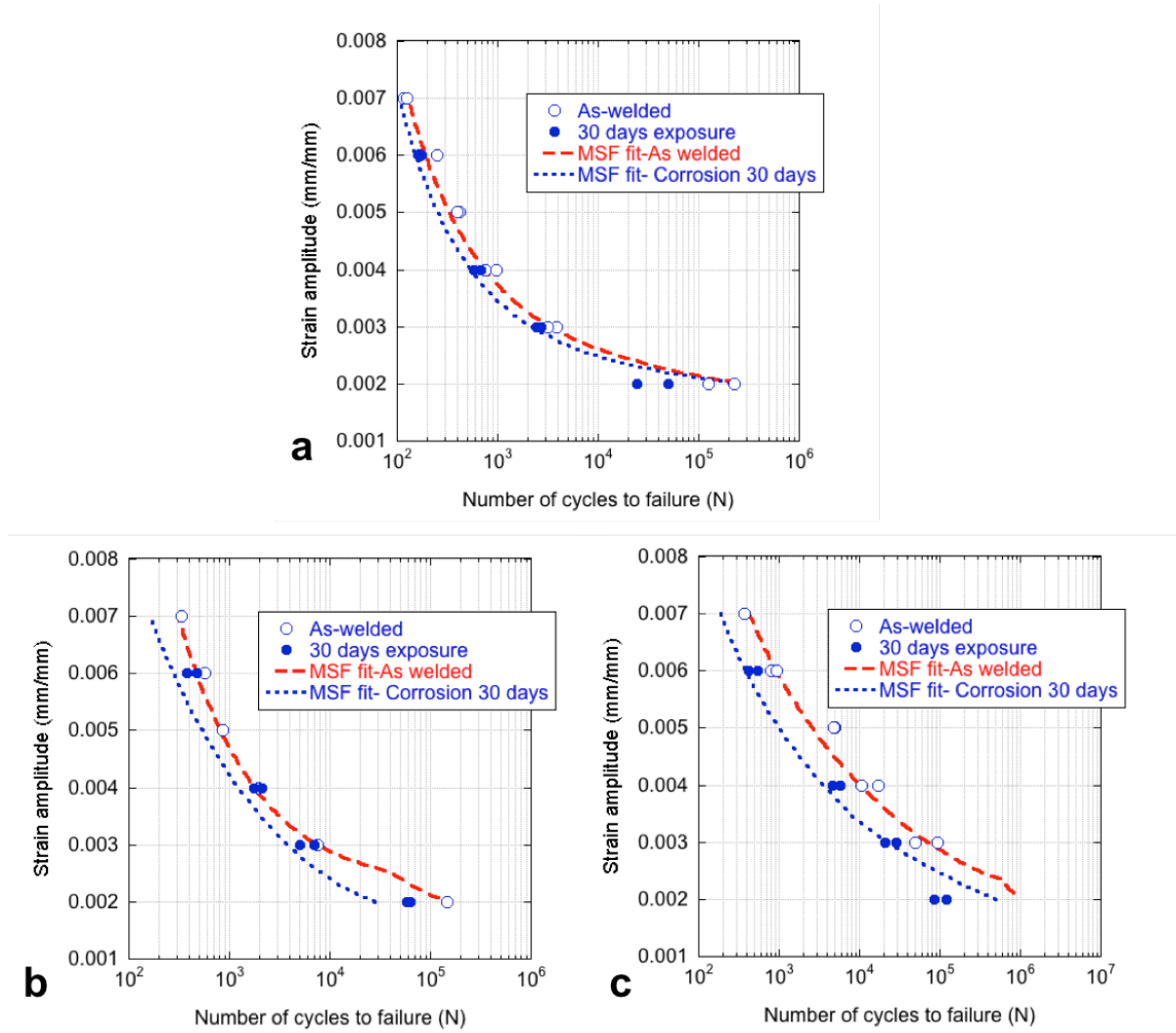


**Figure 4-16. MSF model fit for the fatigue life prediction after corrosion attack for the FSWed (a) AA6061-to-AA7050, (b) AA6061-to-AA6061 and (c) AA7050-to-AA7050.**

The MSF model correlation for the prediction of the fatigue life of the FSWed AA6061-to-AA7050, AA6061-to-AA6061 and AA7050-to-AA7050 in the presence of corrosion defects

is shown in Figure 4-16a-b. The MSF model correlation for the joints in the as-welded condition was calibrated using the low cycle fatigue properties summarized in Table 4-5 and the microstructural features of the joint, such as the grain size and the dimensional characteristic of the secondary intermetallic particles, found in the location of crack propagation which in fact TMAZ/HAZ. It is important to note that the low cycle fatigue properties summarized in Table 4-5 were calculated using the strain-life approach as described in [108]. The MSF model was extended to predict the fatigue life of the joints in the presence of corrosion defects by including the maximum depths of the corrosion pit into the fatigue model calibrated for the as-welded condition.

**Table 4-5. Summary of the low cycle fatigue properties for the dissimilar FSWed AA6061-to-AA7050, AA6061-to-AA6061 and AA7050-to-AA7050.**

Materials	YS $S_y$ (MPa)	UTS $S_u$ (MPa)	Modulus of elasticity $E$ (GPa)	Cyclic hardening exponent $n'$	Cyclic strength coefficient $K'$ (Mpa)	Fatigue strength coefficient $\sigma'_y$ (MPa)	Fatigue strength exponent $b$	Fatigue ductility coefficient $\epsilon'_f$	Fatigue ductility exponent $c$
AA6061-to-AA7050	134.2	192.6	69.7	0.06	266.9	238.7	-0.04	0.14	-0.68
AA6061-to-AA6061	198.0	210.0	68.0	0.06	249.0	251.9	-0.03	0.34	-0.68
AA7050-to-AA7050	345.2	482.2	70.9	0.20	1,574.7	879.1	-0.13	0.07	-0.63

The MSF model for the dissimilar joint is presented in Figure 4-16a. These model results were calculated using the maximum pit depth (30  $\mu\text{m}$ ) measured in the fracture surfaces of the AA6061 side, after 30 days of static immersion in 3.5% NaCl in aqueous solution. As shown in Figure 4-16a, the MSF model captures the effects of the corrosion damage on the fatigue life of the dissimilar welds for strain amplitudes greater than 0.3% strain. However, at 0.2% strain the model deviates and fails in predicting the number of cycles to failure. This deviation at 0.2% strain amplitudes is attributed to the change in the failure mode observed at such low strain amplitude values. As shown in Figure 4-8a, the dissimilar FSWed AA6061-to-AA7050 failed in the TMAZ/HAZ of the AA6061 side, however, the joint failed in the AA7050 side at 0.2% strain. In fact, the defect in the AA7050 side was larger than the mean size observed, which justifies the early failure when compared to the prediction by the model.

Figure 4-16b and Figure 4-16c present the MSF model fit for the fatigue life of the FSWed AA6061-to-AA6061 and AA7050-to-7050 in the as-welded condition and after exposure to the corrosive solution. For the case of the AA6061 joints, the model under predicts the fatigue life in the presence of corrosion defects. In fact, as shown in Figure 4-8b, the fatigue life did not show much decrease after exposure to corrosive solution. The induced corrosion defects resulted in very little effect on decreasing the fatigue life of the joints. Lastly, the MSF model fit for the FSWed AA7050-to-AA750 is shown in Figure 4-16c. As described before, the effects of the exposure to the corrosive solution were more evident in the AA7050 joint when compared to the other two cases. As shown in Figure 4-16c, the MSF was showed a good correlation to the presence of the corrosion defects on the fatigue life of the joints. At low strain amplitudes (0.2%)

the model slightly deviates from the experimental results. As such, additional experimental results are needed, including larger exposure time, to calibrate the model with more precision.

#### 4.5 Conclusions

The low cycle fatigue study of pre-corroded FSW of high strength aluminum alloys is presented. Pre-corroded FSWed AA6061-to-AA7050, AA6061-to-AA6061, and AA7050-to-AA7050 were tested in low cycle fatigue after various exposure times in 3.5% NaCl in aqueous solution. The results and finding from this study are summarized as follows:

1. Localized corrosion damage was observed in the pre-corroded samples for the various combinations of materials and exposure time. The extent of the corrosion damage was characterized by measuring the penetration depth at various exposure times. The corrosion damage featured general pitting, pit clustering and exfoliation, revealing increasing depth with increasing exposure time.
2. For the dissimilar joint, the AA7050 demonstrated the highest corrosion depth of the two materials (AA6061 and AA7050). This can be explained by considering that the AA7050 has higher corrosion susceptibility when compared to the AA6061.
3. The extent of the corrosion damage in the TMAZ/HAZ of the AA7050 in the dissimilar weld, was roughly 1.3 times much severe than the TMAZ/HAZ of the similar FSWed AA7050. On the other hand, for the AA6061, the depth of the corrosion damage was roughly 5 times more severe in the similar FSWed AA6061 when compared to the dissimilar joint (AA6061-to-AA7050). This behavior is attributed to the cathodic protection of the AA6061 in the dissimilar joint.

4. Experimental fatigue results demonstrated a decrease in the fatigue life for all material combinations, with evidence of crack initiation at the corrosion defects; however, the fatigue life was nearly independent of the exposure time. This can be attributed to total fatigue life dominated by incubation time.
5. For the similar FSWed AA6061-to-AA6061 and AA7050-to-AA7050, the cracks initiated at the corrosion defects from either the AS or RS. There was not significant difference on crack propagation on either side.
6. The pre-corroded dissimilar FSWed AA6061-to-AA7050 presented two types of failures: crack propagation in the AA6061 side at high strain amplitudes ( $>0.3\%$ ), and crack propagation in the AA7050 side at low strain amplitudes ( $<0.2\%$ ). This can be attributed to the cyclic strain hardening evolution and the localized high stress field at the tip of the corrosion defect.

## CHAPTER 5

### CONCLUSIONS AND RECOMMENDATIONS

The microstructure and mechanical properties of dissimilar friction stir welding of AA6061-to-AA7050 Al alloys were evaluated. FSW joints were produced under a range of tool rotational speeds, while other parameters were held constant. Also, the effects of corrosion damage on the low cycle fatigue of dissimilar FSWed AA6061-toAA7050 were tested. Furthermore, the multistage fatigue model was extended for the prediction of fatigue life of the dissimilar joint considering the microstructural features such as grain size and intermetallic particles. The finding and contributions of the investigation are summarized as follows:

- For the dissimilar FSWed AA6061-to-AA7050, microstructure analysis of the stir zone revealed the presence of bands of mixed and unmixed material that demonstrated the degree of material intermixing, as the tool rotational speed was varied. Material intermixing and joint strength were found to increase with the increasing tool rotational speed.
- Monotonic tensile tests results demonstrated an increase in the joint strength as the tool rotation speed was increased. This was correlated to the material intermixing.
- Fatigue results revealed an increase in the strain hardening properties as well as the fatigue life as the tool rotational speed was increased for the as-welded conditions.

- For both static and cyclic mechanical testing, the joint strength and failure mode was dominated by the low hardness region corresponding to the AA6061.
- After cyclic loading, crack initiation sites were identified at the crown and root surface of the welds, possibly from near surface secondary intermetallic particles.
- As for the pre-corrosion testing, localized corrosion damage was observed in the pre-corroded samples for the various combinations of materials and exposure time. The corrosion damage featured general pitting, pit clustering and exfoliation, revealing increasing depth with increasing exposure time.
- For the dissimilar joint, the AA7050 demonstrated the highest corrosion depth of the two materials (AA6061 and AA7050). This can be explained by considering that the AA7050 has higher corrosion susceptibility when compared to the AA6061. However, the AA6061 dominated the fatigue performance of the joint.
- Results demonstrated a decrease in the fatigue life for all material combinations, with evidence of crack initiation at the corrosion defects; however, the fatigue life was nearly independent of the exposure time. This can be attributed to total fatigue life dominated by incubation time.
- The pre-corroded dissimilar FSWed A6061-to-AA7050 presented two types of failure: crack propagation in the AA6061 side at high strain amplitudes ( $>0.3\%$ ), and crack propagation in the AA7050 side at low strain amplitudes ( $<0.2\%$ ). This can be attributed to the cyclic strain hardening evolution and the localized high stress field at the tip of the corrosion defect.

- Lastly, a microstructure sensitive multistage fatigue model (MSF) was implemented for the prediction of the fatigue life of the dissimilar joint. The model was successfully correlated for the fatigue prediction of the dissimilar joint in the as-welded and pre-corroded conditions. The upper and lower bounds were calculated considering the microstructural features existing in the location of failure of the welds such as grain size and secondary intermetallic particles.

#### Recommendations and Future Work

- ✓ Under static loading, the maximum joint strength was approximately 192 MPa for a tool rotational speed of 410 rpm. This strength is approximate 62% of the ultimate tensile strength of the AA6061-T6 base material. Thus, future research should focus on exploring other welding parameters to determine the maximum strength that can be achieved for this dissimilar FSWed AA6061-to-AA7050 joint.
- ✓ Further research should focus on studying the local cyclic stress response of dissimilar welded regions. The aim is to achieve better understanding of the effect of local cyclic hardening that can result due to the relative stiffness differences and hardening mechanisms between the parent metals and FSW regions.
- ✓ Since wrought materials can exhibit anisotropic material properties, future work should study the effect of welding orientation (rolling, transverse) on fatigue behavior in the dissimilar FSW.

- ✓ As for future corrosion work, research should investigate more aggressive corrosive solutions such as EXCO. This will allow shorter exposure times, but also lead to more time intervals to better capture exposure time effects on the fatigue life.
- ✓ Lastly, future work should study the effect plug welding in dissimilar welds. Plug welding is particularly used for hole close-outs (as in pressure vessels) and for the weld repairs.

## REFERENCES

- [1] “About AM-2 Matting,” CASS Services [Online]. Available: [www.cassholdings.com/AM2.htm](http://www.cassholdings.com/AM2.htm). [Accessed: 09-Sep-2014].
- [2] “Aluminum and Military Landing Mat,” Calcumet Ind. [Online]. Available: [www.calcumetindustries.com](http://www.calcumetindustries.com). [Accessed: 09-Sep-2014].
- [3] Aizpuru, N., Le, D., McDonald, J., McLennan, L., Tewfik, S., Lee, E. W., Piatkowski, D., Foyos, J., Ogren, J., McLennan, J., and Es-Said, O. S., 2005, “The Effect of Flash Annealing on the Mechanical and Electrical Properties of Previously used AM2 Mats Composed of Al 6061-T6,” *Eng. Fail. Anal.*, **12**(5), pp. 691–698.
- [4] Wilhelm, C., LaCaille, G., Wright, N., Ward, N., Shu, C., Painter, R., Vinqvist, C., Stoyanov, P., Lee, E. W., Piatkowski, D., McLennan, J., Ogren, J., Kumor, C., and Es-Said, O. S., 2009, “Mechanical Properties and Microstructure Characterization of Coated AM2 Al 6061-T6 Mats Exposed to sSimulated Thermal Blast,” *Eng. Fail. Anal.*, **16**(1), pp. 1–10.
- [5] Prietto, M., Tsang, M., Hernandez, S., Roepke, J., Piatkowski, D., Lee, E., Stoyanov, P., Ogren, J., and Es-Said, O. S., 2011, “The eEffects of Heat Damage of Aluminum 6061-T6 AM-2 Mats and High Power Run-Up Anchor,” *Eng. Fail. Anal.*, **18**(1), pp. 124–137.
- [6] “Pre-Engineered Structures: Short Airfield For Tactical Support” [Online]. Available: <http://www.tpub.com/steelworker2/107.htm>. [Accessed: 09-Sep-2014].
- [7] Elangovan, K., and Balasubramanian, V., 2008, “Influences of Tool Pin Profile and Tool Shoulder Diameter on the Formation of Friction Stir Processing Zone in AA6061 Aluminium Alloy,” *Mater. Des.*, **29**, pp. 362–373.
- [8] Nourani, M., Milani, A. S., and Yannacopoulos, S., 2011, “Taguchi Optimization of Process Parameters in Friction Stir Welding of 6061 Aluminum Alloy : A Review and Case Study,” *Engineering*, **2011**(February), pp. 144–155.
- [9] Wang, D., and Chen, C., 2008, “Fatigue Lives of Friction Stir Spot Welds in Aluminum 6061-T6 Sheets,” *J. Mater. Process. Technol.*, **209**(2007), pp. 367–375.
- [10] Colligan, K., 1999, “Material Flow Behavior During Friction Stir Welding of Aluminum,” *Weld. J.*, pp. 229–237.

- [11] Murr, L. E., Liu, G., and McClure, J. C., “A TEM Study of Precipitation and Related Microstructures in Friction-Stir-Welded 6061 Aluminium,” **3**, pp. 1243–1251.
- [12] Rajakumar, S., Muralidharan, C., and Balasubramanian, V., 2010, “Establishing Empirical Relationships to Predict Grain Size and Tensile Strength of Friction Stir Welded AA 6061-T6 Aluminium Alloy Joints,” *Trans. Nonferrous Met. Soc. China*, **20**(10), pp. 1863–1872.
- [13] Gibson, B. T., Lammlein, D. H., Prater, T. J., Longhurst, W. R., Cox, C. D., Ballun, M. C., Dharmaraj, K. J., Cook, G. E., and Strauss, A. M., 2014, “Friction Stir Welding: Process, Automation, and Control,” *J. Manuf. Process.*, **16**(1), pp. 56–73.
- [14] Kulekci, M. K., 2008, “Magnesium and its Alloys Applications in Automotive Industry,” *Int. J. Adv. Manuf. Technol.*, **39**, pp. 851–865.
- [15] Commin, L., Dumont, M., Masse, J.-E., and Barrallier, L., 2009, “Friction Stir Welding of AZ31 Magnesium Alloy Rolled Sheets: Influence of Processing parameters,” *Acta Mater.*, **57**(2), pp. 326–334.
- [16] Solanki, K. N., Jordon, J. B., Whittington, W., Rao, H., and Hubbard, C. R., 2012, “Structure–Property Relationships and Residual Stress Quantification of a Friction Stir Spot Welded Magnesium Alloy,” *Scr. Mater.*, **66**(10), pp. 797–800.
- [17] Yang, Y. K., Dong, H., Cao, H., Chang, Y. A., and Kou, S., 2008, “Liquation of Mg Alloys in Friction Stir Spot Welding,” *Weld. J.*, **87**(July), pp. 167–177.
- [18] Mishra, R.S., Ma, Z. Y., 2005, “Friction Stir Welding and Processing,” *Mater. Sci. Eng. R*, (50), pp. 1–78.
- [19] “Landing Mat” [Online]. Available: [www.militarysystems-tech.com](http://www.militarysystems-tech.com).
- [20] “The Expeditionary Airfield Capability: A Core USMC Competence for Global Operations.”
- [21] Mishra, R. S., and Ma, Z. Y., 2005, “Friction Stir Welding and Processing,” *Mater. Sci. Eng. R* **50**, **50**, pp. 1–78.
- [22] Dursun, T., and Soutis, C., 2014, “Recent Developments in Advanced Aircraft Aluminium Alloys,” *Mater. Des.*, **56**, pp. 862–871.
- [23] John, R., Jata, K. V., and Sadananda, K., 2003, “Residual Stress Effects on Near-Threshold Fatigue Crack Growth in Friction Stir Welds in Aerospace Alloys,” *Int. J. Fatigue*, **25**(9-11), pp. 939–948.

- [24] “What is friction stir welding of aluminum?,” ESAB Knowl. Cent. [Online]. Available: <http://www.esabna.com/us/en/education/blog/what-is-friction-stir-welding-of-aluminum.cfm>.
- [25] Cam, G., and Mistikoglu, S., 2014, “Recent Developments in Friction Stir Welding of Al-Alloys,” *J. Mater. Eng. Perform.*, **23**(6), pp. 1936–1953.
- [26] Schweitzer, P. A., 2003, “Aluminum and Aluminum Alloys,” *Metallic Materials: Physical, Mechanical, and Corrosion Properties*.
- [27] Ozturk, F., Sisman, A., Toros, S., Kilic, S., and Picu, R. C., 2010, “Influence of Aging Treatment on Mechanical Properties of 6061 Aluminum Alloy,” *Mater. Des.*, **31**(2), pp. 972–975.
- [28] Upadhyay, P., and Reynolds, A. P., 2010, “Effects of Thermal Boundary Conditions in Friction Stir Welded AA7050-T7 Sheets,” *Mater. Sci. Eng. A*, **527**, pp. 1537–1543.
- [29] Fuller, C. B., Mahoney, M. W., Calabrese, M., and Micono, L., 2010, “Evolution of Microstructure and Mechanical Properties in Naturally Aged 7050 and 7075 Al Friction Stir Welds,” *Mater. Sci. Eng. A*, **527**(9), pp. 2233–2240.
- [30] Feng, A. H., Chen, D. L., and Ma, Z. Y., 2010, “Microstructure and Low-Cycle Fatigue of a Friction-Stir-Welded 6061 Aluminum Alloy,” *Metall. Mater. Trans. A*, **41**(10), pp. 2626–2641.
- [31] Su, J.-Q., Nelson, T. ., Mishra, R., and Mahoney, M., 2003, “Microstructural Investigation of Friction Stir Welded 7050-T651 aluminium,” *Acta Mater.*, **51**(3), pp. 713–729.
- [32] Jata, K. V., Sankaran, K. K., and Ruschau, J. J., 2000, “Friction-Stir Welding Effects on Microstructure and Fatigue of Aluminum Alloy 7050-T7451,” **31**(September).
- [33] Brown, R., Tang, W., and Reynolds, A. P., 2009, “Multi-Pass Friction Stir Welding in Alloy 7050-T7451: Effects on Weld Response Variables and on Weld Properties,” *Mater. Sci. Eng. A*, **514**, pp. 115–121.
- [34] Su, J.-Q., Nelson, T. W., Mishra, R., and Mahoney, M., 2003, “Microstructural Investigation of Friction Stir Welded 7050-T651 Aluminium,” *Acta Mater.*, **51**(3), pp. 713–729.
- [35] Xu, W. F., Liu, J. H., Chen, D. L., Luan, G. H., and Yao, J. S., 2012, “Improvements of Strength and Ductility in Aluminum Alloy Joints Via Rapid Cooling During Friction Stir Welding,” *Mater. Sci. Eng. A*, **548**, pp. 89–98.
- [36] “Technical Handbook: Friction Stir Welding.”

- [37] Murr, L. E., 2010, "A Review of FSW Research on Dissimilar Metal and Alloy Systems," *J. Mater. Eng. Perform.*, **19**(8), pp. 1071–1089.
- [38] Lee, W.-B., Yeon, Y.-M., and Jung, S.-B., 2003, "The Joint Properties of Dissimilar Formed Al Alloys by Friction Stir Welding According to the Fixed Location of Materials," *Scr. Mater.*, **49**(5), pp. 423–428.
- [39] Murr, L. E., Li, Y., and Elizabeth, R. D. F., 1998, "Intercalation Vortices and Related Microstructural Features in the Friction-Stir Welding of Dissimilar Metals," *Mat Res Innov.*, **2**, pp. 150–163.
- [40] Cavaliere, P., Nobile, R., Panella, F. W., and Squillace, A., 2006, "Mechanical and Microstructural Behaviour of 2024–7075 Aluminium Alloy Sheets Joined by Friction Stir Welding," *Int. J. Mach. Tools Manuf.*, **46**(6), pp. 588–594.
- [41] Palanivel, R., Koshy Mathews, P., Murugan, N., and Dinaharan, I., 2012, "Effect of Tool Rotational Speed and Pin Profile on Microstructure and Tensile Strength of Dissimilar Friction Stir Welded AA5083-H111 and AA6351-T6 Aluminum Alloys," *Mater. Des.*, **40**, pp. 7–16.
- [42] Shigematsu, I., Kwon, Y., Suzuki, K., Imai, T., and Saito, N., 2003, "Joining of 5083 and 6061 Aluminum Alloys by Friction Stir Welding," *J. Mater. Sci. Lett.*, **22**, pp. 353–356.
- [43] Guo, J. F., Chen, H. C., Sun, C. N., Bi, G., Sun, Z., and Wei, J., 2014, "Friction Stir Welding of Dissimilar Materials Between AA6061 and AA7075 Al Alloys Effects of Process Parameters," *Mater. Des.*, **56**, pp. 185–192.
- [44] Feng, a. H., Chen, D. L., and Ma, Z. Y., 2010, "Microstructure and Cyclic Deformation Behavior of a Friction-Stir-Welded 7075 Al Alloy," *Metall. Mater. Trans. A*, **41**(4), pp. 957–971.
- [45] Cavaliere, P., De Santis, A., Panella, F., and Squillace, A., 2009, "Effect of Welding Parameters on Mechanical and Microstructural Properties of Dissimilar AA6082–AA2024 Joints Produced by Friction Stir Welding," *Mater. Des.*, **30**(3), pp. 609–616.
- [46] Sarsilmaz, F., Ozdemir, N., and Kırık, I., 2012, "Evaluation of Microstructure and Fatigue Properties of Dissimilar AA7075/AA6061 Joints Produced by Friction Stir Welding," *Kov. Mater.*, **50**, pp. 259–268.
- [47] Uematsu, Y., Tozaki, Y., Tokajo, K., and Nakamura, M., 2008, "Fatigue Behavior of Dissimilar Friction Stir Welds Between Cast And Wrough Aluminum Alloys," *Strength Mater.*, **40**(1), pp. 138–141.
- [48] Wadson, D. a., Zhou, X., Thompson, G. E., Skeldon, P., Oosterkamp, L. D., and Scamans, G., 2006, "Corrosion Behaviour of Friction Stir Welded AA7108 T79 Aluminium Alloy," *Corros. Sci.*, **48**(4), pp. 887–897.

- [49] Dong, P., Sun, D., Wang, B., Zhang, Y., and Li, H., 2014, “Microstructure, Microhardness and Corrosion Susceptibility of Friction Stir Welded AlMgSiCu Alloy,” *Mater. Des.*, **54**, pp. 760–765.
- [50] Pao, P. ., Gill, S. ., Feng, C. ., and Sankaran, K. ., 2001, “Corrosion–Fatigue Crack Growth in Friction Stir Welded Al 7050,” *Scr. Mater.*, **45**(5), pp. 605–612.
- [51] Jariyaboon, M., Davenport, A. J., Ambat, R., Connolly, B. J., Williams, S. W., and Price, D. a., 2007, “The Effect of Welding Parameters on the Corrosion Behaviour of Friction Stir Welded AA2024–T351,” *Corros. Sci.*, **49**(2), pp. 877–909.
- [52] Kang, J., Fu, R., Luan, G., Dong, C., and He, M., 2010, “In-Situ investigation on the Pitting Corrosion Behavior of Friction Stir Welded Joint of AA2024-T3 Aluminium Alloy,” *Corros. Sci.*, **52**(2), pp. 620–626.
- [53] Corral, J., Trillo, E. A., Li, Y., and Murr, L. E., 2000, “Corrosion of Friction-Stir Welded Aluminum Alloys 2024 and 2195,” **19**, pp. 2117–2122.
- [54] Srinivasan, P. B., Dietzel, W., Zettler, R., dos Santos, J. F., and Sivan, V., 2005, “Stress Corrosion Cracking Susceptibility of Friction Stir Welded AA7075–AA6056 Dissimilar Joint,” *Mater. Sci. Eng. A*, **392**(1-2), pp. 292–300.
- [55] Elangovan, K., Balasubramanian, V., and Valliappan, M., 2008, “Effect of Tool Pin Profile and Tool Rotational Speed on Mechanical Properties of Friction Stir Welded AA6061 Aluminium Alloy,” *Mater. Manuf. Process.*, **23**(3), pp. 251–260.
- [56] Selvaraj, M., Murali, V., and Koteswara Rao, S. R., 2013, “Mechanism of Weld Formation during Friction Stir Welding of Aluminum Alloy,” *Mater. Manuf. Process.*, **28**(5), pp. 595–600.
- [57] Rajakumar, S., and Balasubramanian, V., 2011, “Predicting Grain Size and Tensile Strength of Friction Stir Welded Joints of AA7075-T6 Aluminium Alloy,” *Mater. Manuf. Process.*, **27**(1), pp. 78–83.
- [58] Kumar, K., Kailas, S. V, and Srivatsan, T. S., 2008, “Influence of Tool Geometry in Friction Stir Welding,” *Mater. Manuf. Process.*, **23**(2), pp. 188–194.
- [59] Vijayan, S., Raju, R., and Rao, S. R. K., 2010, “Multiobjective Optimization of Friction Stir Welding Process Parameters on Aluminum Alloy AA 5083 Using Taguchi-Based Grey Relation Analysis,” *Mater. Manuf. Process.*, **25**(11), pp. 1206–1212.
- [60] Ouyang, J. H., and Kovacevic, R., 2002, “Material Flow and Microstructure in the Friction Stir Butt welding Welds of the Same and Dissimilar Aluminum Alloys,” *J. Mater. Eng. Perform.*, **11**(51).

- [61] Esmaeili, A., Besharati Givi, M. K., and Zareie Rajani, H. R., 2012, “Experimental Investigation of Material Flow and Welding Defects in Friction Stir Welding of Aluminum to Brass,” *Mater. Manuf. Process.*, **27**(12), pp. 1402–1408.
- [62] Palanivel, R., Koshy Mathews, P., Dinaharan, I., and Murugan, N., 2014, “Mechanical and metallurgical properties of dissimilar friction stir welded AA5083-H111 and AA6351-T6 aluminum alloys,” *Trans. Nonferrous Met. Soc. China*, **24**(1), pp. 58–65.
- [63] Amancio-Filho, S. T., Sheikhi, S., dos Santos, J. F., and Bolfarini, C., 2008, “Preliminary Study on the Microstructure and Mechanical Properties of Dissimilar Friction Stir Welds in Aircraft Aluminium Alloys 2024-T351 and 6056-T4,” *J. Mater. Process. Technol.*, **206**(1-3), pp. 132–142.
- [64] Liu, G., Murr, L. E., Niou, C.-S., McClure, J. C., and Vega, F. R., 1997, “Microstructural Aspects of the Friction-Stir Welding of 6061-T6 Aluminum,” *Scr. Mater.*, **37**(3), pp. 355–361.
- [65] Da Silva, A. A. M., Arruti, E., Janeiro, G., Aldanondo, E., Alvarez, P., and Echeverria, A., 2011, “Material Flow and Mechanical Behaviour of Dissimilar AA2024-T3 and AA7075-T6 Aluminium Alloys Friction Stir Welds,” *Mater. Des.*, **32**(4), pp. 2021–2027.
- [66] Koilraj, M., Sundareswaran, V., Vijayan, S., and Koteswara Rao, S. R., 2012, “Friction Stir Welding of Dissimilar Aluminum Alloys AA2219 to AA5083 – Optimization of Process Parameters Using Taguchi Technique,” *Mater. Des.*, **42**, pp. 1–7.
- [67] Jamshidi Aval, H., 2015, “Influences of Pin Profile on the Mechanical and Microstructural Behaviors in Dissimilar Friction Stir Welded AA6082–AA7075 Butt Joint,” *Mater. Des.*, **67**, pp. 413–421.
- [68] Baragetti, S., and D’Urso, G., 2014, “Aluminum 6060-T6 Friction Stir Welded Butt Joints: Fatigue Resistance With Different Tools and Feed Rates,” *J. Mech. Sci. Technol.*, **28**(3), pp. 867–877.
- [69] Sharma, C., Dwivedi, D. K., and Kumar, P., 2014, “Fatigue Behavior of Friction Stir Weld Joints of Al–Zn–Mg Alloy AA7039 Developed Using Base Metal in Different Temper Condition,” *Mater. Des.*, **64**, pp. 334–344.
- [70] Moreira, P. M. G. P., de Oliveira, F. M. F., and de Castro, P. M. S. T., 2008, “Fatigue Behaviour of Notched Specimens of Friction Stir Welded Aluminium Alloy 6063-T6,” *J. Mater. Process. Technol.*, **207**(1-3), pp. 283–292.
- [71] James, M. N., Hattingh, D. G., and Bradley, G. R., 2003, “Weld Tool travel Speed Effects on Fatigue Life of Friction Stir Welds in 5083 Aluminium,” *Int. J. Fatigue*, **25**(12), pp. 1389–1398.

- [72] Ghidini, T., and Dalle Donne, C., 2009, “Fatigue Life Predictions Using Fracture Mechanics Methods,” *Eng. Fract. Mech.*, **76**(1), pp. 134–148.
- [73] Dickerson, T. L., and Przydatek, J., 2003, “Fatigue of Friction Stir Welds in Aluminium Alloys that Contain Root Flaws,” *Int. J. Fatigue*, **25**(12), pp. 1399–1409.
- [74] Ericsson, M., 2003, “Influence of Welding Speed on the Fatigue of Friction Stir Welds, and Comparison with MIG and TIG,” *Int. J. Fatigue*, **25**(12), pp. 1379–1387.
- [75] Sillapasa, K., Surapunt, S., Miyashita, Y., Mutoh, Y., and Seo, N., 2014, “Tensile and Fatigue Behavior of SZ, HAZ and BM in Friction Stir Welded joint of Rolled 6N01 Aluminum Alloy Plate,” *Int. J. Fatigue*, **63**, pp. 162–170.
- [76] Takahashi, Y., Shikama, T., Yoshihara, S., Aiura, T., and Noguchi, H., 2012, “Study on Dominant Mechanism of high-Cycle Fatigue Life in 6061-T6 Aluminum Alloy Trough Microanalyses of Microstructurally Small Cracks,” *Acta Mater.*, **60**(6-7), pp. 2554–2567.
- [77] Zhou, C., Yang, X., and Luan, G., 2006, “Investigation of Microstructures and Fatigue Properties of Friction Stir Welded Al-Mg Alloy,” *Mater. Chem. Phys.*, **98**(2-3), pp. 285–290.
- [78] Xu, W. F., Liu, J. H., Chen, D. L., Luan, G. H., and Yao, J. S., 2012, “Change of Microstructure and Cyclic Deformation Behavior Along the Thickness in a Friction-Stir-Welded Aluminum Alloy,” *Scr. Mater.*, **66**(1), pp. 5–8.
- [79] Ceschini, L., Boromei, I., Minak, G., Morri, a., and Tarterini, F., 2007, “Microstructure, tensile and fatigue properties of AA6061/20 vol.%Al<sub>2</sub>O<sub>3</sub>p friction stir welded joints,” *Compos. Part A Appl. Sci. Manuf.*, **38**(4), pp. 1200–1210.
- [80] Czechowski, M., 2005, “Low-Cycle Fatigue of Friction Stir Welded Al-Mg Alloys,” *J. Mater. Process. Technol.*, **164-165**, pp. 1001–1006.
- [81] Rodriguez, R. I., Jordon, J. B., Allison, P. G., Rushing, T., and Garcia, L., 2015, “Microstructure and Mechanical Properties of Dissimilar Friction Stir Welding of 6061-to-7050 Aluminum Alloys,” *Mater. Des.*, **83**, pp. 60–65.
- [82] McDowell, D. L., Gall, K., Horstemeyer, M. F., and Fan, J., 2003, “Microstructure-Based Fatigue Modeling of Cast A356-T6 Alloy,” *Eng. Fract. Mech.*, **70**(1), pp. 49–80.
- [83] Jordon, J. B., Gibson, J. B., Horstemeyer, M. F., El Kadiri, H., Baird, J. C., and Luo, a. a., 2011, “Effect of Twinning, Slip, and Inclusions on the Fatigue Anisotropy of Extrusion-Textured AZ61 Magnesium Alloy,” *Mater. Sci. Eng. A*, **528**(22-23), pp. 6860–6871.
- [84] Lugo, M., Jordon, J. B., Solanki, K. N., Hector, L. G., Bernard, J. D., Luo, A. a., and Horstemeyer, M. F., 2013, “Role of Different Material Processing Methods on the Fatigue Behavior of an AZ31 Magnesium alloy,” *Int. J. Fatigue*, **52**(August), pp. 131–143.

- [85] Rettberg, L. H., Jordon, J. B., Horstemeyer, M. F., and Jones, J. W., 2012, “Low-Cycle Fatigue Behavior of Die-Cast Mg Alloys AZ91 and AM60,” *Metall. Mater. Trans. A Phys. Metall. Mater. Sci.*, **43**(7), pp. 2260–2274.
- [86] Xue, Y., Horstemeyer, M. F., McDowell, D. L., El Kadiri, H., and Fan, J., 2007, “Microstructure-Based Multistage Fatigue Modeling of a Cast AE44 Magnesium Alloy,” *Int. J. Fatigue*, **29**, pp. 666–6796.
- [87] Xue, Y., Burton, C. L., Horstemeyer, M. F., McDowell, D. L., and Berry, J. T., 2007, “Multistage Fatigue Modeling of Cast A356-T6 and A380-F Aluminum Alloys,” *Metall. Mater. Trans. B Process Metall. Mater. Process. Sci.*, **38**(4), pp. 601–606.
- [88] Xue, Y., McDowell, D. L., Horstemeyer, M. F., Dale, M. H., and Jordon, J. B., 2007, “Microstructure-Based Multistage Fatigue Modeling of Aluminum Alloy 7075-T651,” *Eng. Fract. Mech.*, **74**(17), pp. 2810–2823.
- [89] Xue, Y., El Kadiri, H., Horstemeyer, M. F., Jordon, J. B., and Weiland, H., 2007, “Micromechanisms of Multistage Fatigue Crack Growth in a High-Strength Aluminum Alloy,” *Acta Mater.*, **55**(6), pp. 1975–1984.
- [90] McCullough, R. R., Jordon, J. B., Brammer, a. T., Manigandan, K., Srivatsan, T. S., Allison, P. G., and Rushing, T. W., 2013, “A Fatigue Model for Discontinuous Particulate-Reinforced Aluminum Alloy Composite: Influence of Microstructure,” *J. Mater. Eng. Perform.*, **23**(1), pp. 65–76.
- [91] Jordon, J. B., and Horstemeyer, M. F., 2014, “Microstructure-Sensitive Fatigue Modeling of AISI 4140 Steel,” *J. Eng. Mater. Technol.*, **136**(2), p. 021004.
- [92] Allison, P. G., Hammi, Y., Jordon, J. B., and Horstemeyer, M. F., 2013, “Modelling and experimental study of fatigue of powder metal steel (FC-0205),” *Powder Metall.*, **56**(5), pp. 388–396.
- [93] Xue, Y., Pascu, A., Horstemeyer, M. F., Wang, L., and Wang, P. T., 2010, “Microporosity Effects on Cyclic Plasticity and fFatigue of LENS-Processed Steel,” *Acta Mater.*, **58**(11), pp. 4029–4038.
- [94] Xue, Y., McDowell, D. L., Horstemeyer, M. F., Dale, M. H., and Jordon, J. B., 2007, “Microstructure-based multistage fatigue modeling of aluminum alloy 7075-T651,” *Eng. Fract. Mech.*, **74**(17), pp. 2810–2823.
- [95] Dos Santos, J. F., Olea, C. A. ., Coelho, R. ., Kostaka, A., Paglia, C. C., Ghidini, T., and Donne, C. D., 2009, “Metallurgy and Weld Performance in Friction Stir Welding,” *Friction Stir Welding, From Basics to Applications*, pp. 314–409.

- [96] Lumsden, J. B., Mahoney, M. W., Pollock, G., and Rhodes, C. G., 1999, "Intergranular Corrosion Following Friction Stir Welding of Aluminum Alloy 7075-T651," *Corrosion*, **55**(12), pp. 1127–1135.
- [97] DuQuesnay, D. L., Underhill, P. R., and Britt, H. J., 2003, "Fatigue Crack Growth From Corrosion Damage in 7075-T6511 Aluminium Alloy Under Aircraft Loading," *Int. J. Fatigue*, **25**(5), pp. 371–377.
- [98] Burns, J. T., Kim, S., and Gangloff, R. P., 2010, "Effect of Corrosion Severity on Fatigue Evolution in Al-Zn-Mg-Cu," *Corros. Sci.*, **52**(2), pp. 498–508.
- [99] Burns, J. T., Larsen, J. M., and Gangloff, R. P., 2012, "Effect of Initiation Feature on Microstructure-Scale Fatigue Crack Propagation in Al-Zn-Mg-Cu," *Int. J. Fatigue*, **42**, pp. 104–121.
- [100] Jones, K., Shinde, S. R., Clark, P. N., and Hoepfner, D. W., 2008, "Effect of Prior Corrosion on Short Crack Behavior in 2024-T3 Aluminum Alloy," *Corros. Sci.*, **50**(9), pp. 2588–2595.
- [101] Kim, S., Burns, J. T., and Gangloff, R. P., 2009, "Fatigue Crack Formation and Growth from Localized Corrosion in Al-Zn-Mg-Cu," *Eng. Fract. Mech.*, **76**(5), pp. 651–667.
- [102] Sankaran, K. K., Perez, R., and Jata, K. V., 2001, "Effects of Pitting Corrosion on the Fatigue Behavior of Aluminum Alloy 7075-T6: Modeling and Experimental Studies," *Mater. Sci. Eng. A*, **297**(1-2), pp. 223–229.
- [103] Van der Walde, K., and Hillberry, B. M., 2007, "Initiation and Shape Development of Corrosion-Nucleated Fatigue Cracking," *Int. J. Fatigue*, **29**(7), pp. 1269–1281.
- [104] Van der Walde, K., and Hillberry, B. M., 2008, "Characterization of Pitting Damage and Prediction of Remaining Fatigue Life," *Int. J. Fatigue*, **30**(1), pp. 106–118.
- [105] Van Der Walde, K., Brockenbrough, J. R., Craig, B. a., and Hillberry, B. M., 2005, "Multiple Fatigue Crack Growth in Pre-Corroded 2024-T3 Aluminum," *Int. J. Fatigue*, **27**(10-12), pp. 1509–1518.
- [106] Gruenberg, K. M., Craig, B. a., Hillberry, B. M., Bucci, R. J., and Hinkle, a. J., 2004, "Predicting Fatigue Life of Pre-corroded 2024-T3 Aluminum," *Int. J. Fatigue*, **26**(6), pp. 629–640.
- [107] Yang, B., Yan, J., Sutton, M. a., and Reynolds, A. P., 2004, "Banded Microstructure in AA2024-T351 and AA2524-T351 Aluminum Friction stir Welds. Part I. Metallurgical studies," *Mater. Sci. Eng. A*, **364**(1-2), pp. 55–65.
- [108] Stephens, R. ., Fatemi, A., Stephenes, R. R., and Fuchs, H. O., 2001, "Cyclic Deformation and the Strain -life (e-N) aApproach," *Metal Fatigue In Engineering* 2nd ed, pp. 93–121.

- [109] Guo, J., Gougeon, P., and Chen, X.-G., 2012, "Microstructure Evolution and Mechanical Properties of Dissimilar Friction Stir Welded Joints Between AA1100-B4C MMC and AA6063 Alloy," *Mater. Sci. Eng. A*, **553**, pp. 149–156.
- [110] Ravikumar, S., Rao, V. S., and Pranesh, R. V, 2014, "Effect of Process Parameters on Mechanical Properties of Friction Stir Welded Dissimilar Materials between AA6061-T651 and AA7075-T651 Alloys," *Int. J. Adv. Mech. Eng.*, **4**(1), pp. 101–114.

APPENDIX

**Table 7-1. Dissimilar FSW of Al alloys.**

Materials	Welding Parameters	Max Joint Strength	Contributions/Findings	Ref.
<ul style="list-style-type: none"> <li>•AA7075</li> <li>•AA6061</li> </ul>	<ul style="list-style-type: none"> <li>• Tilt angle: 2.5°</li> <li>• Triangular and cylindrical threaded pin tool</li> <li>• T: 120-250 mm/min</li> <li>• R: 1120 and 1400 rpm</li> </ul>	204.2 MPa (65.8 % efficiency)	<ul style="list-style-type: none"> <li>•Dissimilar FSW AA6061-to-AA7075</li> <li>•Monotonic tensile testing</li> <li>•Microstructural evaluation (OM)</li> <li>•High cycle fatigue</li> </ul>	[46]
<ul style="list-style-type: none"> <li>•A 356</li> <li>•AA6061</li> </ul>	<ul style="list-style-type: none"> <li>• Tilt angle 3°</li> <li>• Cylindrical threaded pin tool</li> <li>• T: 87-267 mm/min</li> <li>• R: 1600 rpm</li> </ul>	192 MPa	<ul style="list-style-type: none"> <li>•Microstructural evaluation (OM and SEM)</li> <li>•Monotonic tensile testing</li> </ul>	[38]
<ul style="list-style-type: none"> <li>•AA2219-T7</li> <li>•AA5083-H321</li> </ul>	<ul style="list-style-type: none"> <li>• Pin length: 5.7 mm, pin diameter (6 mm)</li> <li>• T: 15–60 mm/s</li> <li>• R: 400-800 rpm</li> </ul>	298 MPa	<ul style="list-style-type: none"> <li>•Process optimization using Taguchi method</li> <li>•Microstructural characterization (OM)</li> </ul>	[66]

<ul style="list-style-type: none"> <li>•AA5083</li> <li>•AA6061</li> </ul>	<ul style="list-style-type: none"> <li>• Tool shoulder diameter: 10 mm</li> <li>• Pin diameter: 3 mm</li> <li>• Pin length: 2.8 mm</li> <li>• T: 155 mm/min</li> <li>• R: 890-1540 rpm</li> </ul>	202 MPa	<ul style="list-style-type: none"> <li>•Microstructural characterization (OM)</li> <li>•Microstructural evolution after aging at 433K for 3, 6 and 9 hours.</li> </ul>	[42]
<ul style="list-style-type: none"> <li>•AA2024</li> <li>•AA6061</li> </ul>	<ul style="list-style-type: none"> <li>• T: 57-330 mm/min</li> <li>• R: 151-914 rpm</li> </ul>	N/A	<ul style="list-style-type: none"> <li>•Material flow and microstructural characterization (OM)</li> <li>•Comparison between 6061-to-6061 FSW and 2024-to-6061 FSW</li> </ul>	[60]
<ul style="list-style-type: none"> <li>•AA5083</li> <li>•AA6351</li> </ul>	<ul style="list-style-type: none"> <li>• T: 36, 63 and 90 mm/min</li> <li>• R: 950 rpm</li> <li>• Shoulder diameter: 18 mm</li> <li>• Pin diameter: 6 mm</li> <li>• Pin length: 5.7 mm</li> </ul>	270 MPa	<ul style="list-style-type: none"> <li>•Material flow and microstructural characterization (OM)</li> <li>•Monotonic tensile loading</li> </ul>	[62]
<ul style="list-style-type: none"> <li>•AA2024-T351</li> </ul>	<ul style="list-style-type: none"> <li>• R: 500-1200 rpm</li> <li>• T: 150-400 mm/min</li> </ul>	246 MPa	<ul style="list-style-type: none"> <li>•Material flow and microstructural</li> </ul>	[63]

<ul style="list-style-type: none"> <li>•AA6056-T4</li> </ul>	<ul style="list-style-type: none"> <li>• Pin diameter: 5 mm</li> <li>• Shoulder diameter: 15 mm</li> <li>• Cylindrical threaded tool</li> </ul>		<ul style="list-style-type: none"> <li>• characterization (OM and SEM)</li> <li>• Temperature monitoring during FSW process.</li> <li>• Micromechanical testing (flat tensile specimens) of different locations at the weld.</li> </ul>	
<ul style="list-style-type: none"> <li>•AA6061</li> <li>•AA7075</li> </ul>	<ul style="list-style-type: none"> <li>• R: 1200 rpm</li> <li>• T: 2-5 mm/s</li> <li>• Tilt angle: 2.5°</li> </ul>	<p>245 MPa (79 % efficiency), AA6061 in the advancing side</p>	<ul style="list-style-type: none"> <li>• Peak temperature at different tool parameters</li> <li>• Material flow and microstructural characterization (OM, SEM and EDS)</li> <li>• Monotonic mechanical testing</li> <li>• Effects of the material location (advancing or retreating) in the joint</li> </ul>	<p>[43]</p>

			<p>efficiency</p> <ul style="list-style-type: none"> <li>• Material mixing was found to be more effective when the softer material was located in the advancing side.</li> </ul>	
<ul style="list-style-type: none"> <li>• AA2024-T3</li> <li>• AA7075-T6</li> </ul>	<ul style="list-style-type: none"> <li>• R: 1200 rpm</li> <li>• T: 2-5 mm/s</li> <li>• Tilt angle: 3°</li> <li>• Threaded pin and flat shoulder</li> <li>• AA7075 placed in the advancing side</li> <li>• T: 254 mm/min</li> <li>• R: 400-2000 rpm</li> </ul>	<p>443 MPa (96% joint efficiency)</p>	<ul style="list-style-type: none"> <li>• Material flow and microstructural characterization (OM)</li> <li>• Monotonic tensile loading.</li> <li>• Material flow using stop action technique.</li> </ul>	[65]
<ul style="list-style-type: none"> <li>• AA6061</li> <li>• AA2024</li> </ul>	<ul style="list-style-type: none"> <li>• R: 400-1200rpm</li> <li>• T-1-3 mm/s</li> <li>• 0.65 cm threaded cylindrical pin</li> <li>• 1.9 cm shoulder</li> </ul>	N/A	<ul style="list-style-type: none"> <li>• Material flow and microstructural characterization (OM).</li> <li>• TEM evaluation of the stir zone in the dissimilar FSW of</li> </ul>	[39]

			AA2024-to-AA6061	
<ul style="list-style-type: none"> <li>•AA1100-B4C MMC</li> <li>•AA6063</li> </ul>	<ul style="list-style-type: none"> <li>• R: 2000 rpm</li> <li>• T: 100-200 mm/min</li> </ul>	126-128 MPa (~100% joint efficiency)	<ul style="list-style-type: none"> <li>•Feasibility study of dissimilar FSW between AA1100-16 vol.% b4C metal matrix composite and AA6063 Al alloy.</li> <li>•Material flow and microstructural characterization (OM)</li> <li>•EBSD analysis of the nugget.</li> <li>•Monotonic tensile test.</li> </ul>	[109]
<ul style="list-style-type: none"> <li>•AA2014</li> <li>•AA2195</li> </ul>	<ul style="list-style-type: none"> <li>• R: 800 rpm</li> <li>• T: 1 mm/s</li> </ul>	N/a	<ul style="list-style-type: none"> <li>•Microstructural characterization (OM and TEM)</li> <li>•Corrosion behavior of dissimilar FSW.</li> </ul>	[53]
•AA6061-T651	<ul style="list-style-type: none"> <li>• Multiple tool profiles: 1) simple square, 20</li> </ul>	205 MPa	•AA6061 in the advancing side	

<ul style="list-style-type: none"> <li>•AA7075-T651</li> </ul>	<p>cylindrical tapered and</p> <p>3) tapered square</p> <ul style="list-style-type: none"> <li>• R: 800-1000 rpm</li> <li>• T: 90-110 mm/min</li> </ul>		<ul style="list-style-type: none"> <li>• Monotonic tensile loading</li> <li>• Microstructural characterization (OM)</li> </ul>	[110]
<ul style="list-style-type: none"> <li>•AA2024</li> <li>•AA7075</li> </ul>	<ul style="list-style-type: none"> <li>• T: 2.67 mm/s</li> <li>• Tilt angle: 3°</li> <li>• 6 mm pin diameter</li> <li>• 20 mm shoulder diameter</li> </ul>	424 MPa	<ul style="list-style-type: none"> <li>• Microstructural characterization (OM).</li> <li>• Monotonic tensile loading</li> <li>• High cycle fatigue</li> </ul>	[40]
<ul style="list-style-type: none"> <li>•AA5083-H111</li> <li>•AA6351-T6</li> </ul>	<ul style="list-style-type: none"> <li>• R: 600-1300 rpm</li> <li>• 5 different tool pin profiles 1) straight square, 2) straight hexagon, 3) straight octagon, 4) tapered square and 5) tapered octagon.</li> </ul>	273 MPa	<ul style="list-style-type: none"> <li>• Microstructural characterization (OM)</li> <li>• Tool profile effects</li> <li>• Monotonic tensile loading</li> </ul>	[41]

**Table 7-2. Fatigue life performance: Similar and dissimilar FSW Al alloys.**

	Materials	Welding Parameters	Max Joint Strength	Contributions/Findings	Ref.
Similar FSW	<ul style="list-style-type: none"> <li>• AA66061-T651</li> </ul>	<ul style="list-style-type: none"> <li>• Cylindrical threaded tool</li> <li>• Shoulder diameter: 16 mm</li> <li>• Pin diameter: 6 mm</li> <li>• R: 600-1400 rpm</li> <li>• T: 200-600 mm/min</li> </ul>	N/A	<ul style="list-style-type: none"> <li>• Microstructural evaluation (OM, SEM, EBSD and TEM).</li> <li>• Low cycle fatigue (R=-1), Strain 0.2-0.8%.</li> <li>• Fatigue lifetime and cyclic stress amplitude increased with increasing welding speed, but they were independent of the rotational rate</li> <li>• The majority of the welds failed though the low hardness zones (TMAZ)</li> </ul>	[30]
	<ul style="list-style-type: none"> <li>• AA7075</li> </ul>	<ul style="list-style-type: none"> <li>• Cylindrical threaded tool</li> </ul>	N/A	<ul style="list-style-type: none"> <li>• Microstructural evaluation (OM, SEM,</li> </ul>	[44]

		<ul style="list-style-type: none"> <li>• Shoulder diameter: 20 mm</li> <li>• Pin diameter: 8 mm</li> <li>• R: 800-1200 rpm</li> <li>• T: 100-400 mm/min</li> </ul>		<p>and TEM).</p> <ul style="list-style-type: none"> <li>• Low cycle fatigue (R=-1), Strain 0.2-1.0%.</li> <li>• Cyclic hardening and fatigue life increased with increasing welding speed from 100 to 400 mm/min.</li> <li>• The majority of the welds failed though the low hardness zones (TMAZ)</li> </ul>	
	<ul style="list-style-type: none"> <li>• AA7050-T7451</li> </ul>	<ul style="list-style-type: none"> <li>• R: 396 rpm</li> <li>• T: 1.7 mm/s</li> </ul>	417 MPa	<ul style="list-style-type: none"> <li>• Microstructural characterization in the as-receive and post-heat treated (annealed at 121C for 24 hours) conditions (OM, SEM and TEM).</li> <li>• Post weld heat treatment did not resulted in strength or</li> </ul>	[32]

				<p>ductility improvement.</p> <ul style="list-style-type: none"> <li>• Fatigue crack growth at 0.70 stress ratio.</li> <li>• Very fine strengthening precipitates were formed in the weld-nugget region after heat treatment.</li> </ul>	
Dissimilar FSW	<ul style="list-style-type: none"> <li>• AA6061</li> <li>• AC4CH-T6</li> </ul>	<ul style="list-style-type: none"> <li>• Tilt angle: 3°</li> <li>• Pin diameter: 6 mm</li> <li>• Shoulder diameter: 14 mm</li> <li>• T: 150 mm/min</li> <li>• R: 1000 rpm</li> </ul>	N/A	<ul style="list-style-type: none"> <li>• Fatigue fracture occurred through the AC4CH-T6.</li> <li>• Microstructural evaluation (OM)</li> <li>• High cycle fatigue.</li> <li>• Fatigue strength was nearly the same as the AC4CH parent metal.</li> </ul>	[47]
	<ul style="list-style-type: none"> <li>• AA7075</li> <li>• AA6061</li> </ul>	<ul style="list-style-type: none"> <li>• Tilt angle: 2.5°</li> <li>• Two different tool profiles: 1) cylindrical and 2) triangular</li> </ul>	204.2 MPa	<ul style="list-style-type: none"> <li>• Microstructural evolution (OM)</li> <li>• Monotonic tensile loading</li> <li>• High cycle fatigue</li> </ul>	[46]

		<ul style="list-style-type: none"> <li>• T: 1120-1400 rpm</li> <li>• R: 160-250 mm/min</li> </ul>		(stress controlled)	
<ul style="list-style-type: none"> <li>•AA6082</li> <li>•AA2024</li> </ul>	<ul style="list-style-type: none"> <li>• T: 1600 rpm</li> <li>• R: 80-115 mm/min</li> <li>• Tool: Conical shape with a large diameter of 3.8 mm and small diameter of 2.6 mm, the shoulder diameter measured 9.5 mm.</li> </ul>	235 MPa	<ul style="list-style-type: none"> <li>• Microstructural evaluation (OM)</li> <li>• Effects of material position in the joint strength.</li> <li>• Effects of annealing at 250C for 1 hour.</li> <li>• High cycle fatigue.</li> <li>• The best tensile and fatigue properties were obtained for the joints with the AA6082 on the advancing side and welded with an advancing speed of 115 mm/min.</li> </ul>	[45]	
<ul style="list-style-type: none"> <li>•AA2024</li> <li>•AA7075</li> </ul>	<ul style="list-style-type: none"> <li>• T: 2.67 mm/s</li> <li>• Tilt angle: 3°</li> </ul>	424 MPa	<ul style="list-style-type: none"> <li>• Microstructural characterization (OM).</li> </ul>	[40]	

		<ul style="list-style-type: none"><li>• 6 mm pin diameter</li><li>• 20 mm shoulder diameter</li></ul>		<ul style="list-style-type: none"><li>• Monotonic tensile loading</li><li>• High cycle fatigue</li></ul>	
--	--	---	--	--	--

**Table 7-3. Corrosion: Similar and dissimilar FSW of Al alloys.**

	Materials	Welding Parameters	Corrosion Test	Contributions/Findings	Reference
Similar FSW	•AA7108-T79	<ul style="list-style-type: none"> <li>• Cylindrical threaded tool</li> <li>• Shoulder diameter: 16 mm</li> <li>• Pin diameter: 6 mm</li> <li>• R: 600-1400 rpm</li> <li>• T: 1 m/min</li> </ul>	<ul style="list-style-type: none"> <li>• Modified ASTM G34, EXCO test.</li> <li>Exposure to corrosive solution for 72 hours.</li> </ul>	<ul style="list-style-type: none"> <li>• Open circuit potential measurements.</li> <li>• Microstructural characterization (OM, SEM and TEM).</li> <li>• TMAZ regions were the most susceptible to corrosion.</li> </ul>	[48]
	•6005A-T6	<ul style="list-style-type: none"> <li>• Shoulder diameter: 10 mm</li> <li>• Pin diameter; 2.8 mm</li> <li>• R: 1200 rpm</li> <li>• T: 300 mm/min</li> </ul>	<ul style="list-style-type: none"> <li>• Intergranular corrosion test (ASTM:G110)</li> </ul>	<ul style="list-style-type: none"> <li>• Microstructural characterization (OM, SEM and TEM).</li> <li>• Pitting and corrosion in the heat affect zone were observed due to the precipitate coarsening after</li> </ul>	[49]

				welding.	
	<ul style="list-style-type: none"> <li>• AA7050-T451</li> </ul>	<ul style="list-style-type: none"> <li>• R: 400 rpm</li> <li>• 100 mm/min</li> <li>• Aging at 121 C for 24 hours.</li> </ul>	<ul style="list-style-type: none"> <li>• Fatigue crack growth in accord with ASTM E647 (3.5% NaCl solution)</li> </ul>	<ul style="list-style-type: none"> <li>• Microstructural characterization (OM, SEM and TEM).</li> <li>• Fatigue crack growth</li> <li>• Fatigue crack growth rates in FSW weld and HAZ regions are up to two times higher than NaCl than those in air.</li> <li>• Intergranular fracture when exposed to corrosive environment.</li> </ul>	[50]
	<ul style="list-style-type: none"> <li>• AA2024-T351</li> </ul>	<ul style="list-style-type: none"> <li>• R: 215-468 rpm</li> <li>• T: 75-154 mm/min</li> </ul>	<ul style="list-style-type: none"> <li>• Immersion test in 0.1 M NaCl for 24 hours</li> <li>• Immersion test in 57 g/l (0.98 M) NaCl and 10</li> </ul>	<ul style="list-style-type: none"> <li>• Microstructural characterization (OM and SEM).</li> <li>• Friction stir welds were susceptible to corrosion in the nugget and HAZ regions.</li> <li>• Intergranular attack.</li> </ul>	[51]

			<p>ml.l 30 vol.% H<sub>2</sub>O<sub>2</sub> for susceptibility to intergranular attack.</p>	<p>•The rotation speed was found as the main factor in determining the location for corrosion attack.</p>	
	<p>•AA2024-T3</p>	<ul style="list-style-type: none"> <li>• R: 700 rpm</li> <li>• T: 200 mm/min</li> </ul>	<ul style="list-style-type: none"> <li>• Immersi on test according to ASTM G34-01 using EXCO solution to accelerated pitting and exfoliation carrion.</li> <li>• Tested were carried out at 0, 0.5, 1</li> </ul>	<ul style="list-style-type: none"> <li>•Microstructural characterization (OM and SEM).</li> <li>•Pitting corrosion was observed after 2 hour of exposure to EXCO.</li> </ul>	<p>[52]</p>

			and 2 hours.		
Dissimilar FSW	<ul style="list-style-type: none"> <li>• AA2024-T4</li> <li>• AA2195</li> </ul>	<ul style="list-style-type: none"> <li>• Tilt angle: 3°</li> <li>• Pin diameter: 6.35 mm</li> <li>• Shoulder diameter: 19 mm</li> <li>• T: 1 mm/s</li> <li>• R: 800 rpm</li> </ul>	<ul style="list-style-type: none"> <li>• Static immersion test in 0.6 M NaCl for 20, 48 and 600 hours.</li> </ul>	<ul style="list-style-type: none"> <li>• Microstructural characterization (OM and TEM)</li> <li>• Potentiodynamic characterization.</li> <li>• An even amount of by-product build up was observed in the FSW and base material sections after submersion test.</li> </ul>	[53]
	<ul style="list-style-type: none"> <li>• AA7075</li> <li>• A6056</li> </ul>	<ul style="list-style-type: none"> <li>• Pin diameter: 5 mm</li> <li>• Shoulder diameter: 15 mm</li> <li>• T: 250 mm/min</li> <li>• R: 900 rpm</li> </ul>	<ul style="list-style-type: none"> <li>• Stress corrosion cracking test in 3.5% NaCl at a nominal strain rate of <math>10^{-6} \text{s}^{-1}</math></li> </ul>	<ul style="list-style-type: none"> <li>• Microstructural characterization (OM, SEM and EDS).</li> <li>• The base materials, TMAZ, HAZ and SZ are not susceptible to stress corrosion cracking when tested at <math>10^{-6} \text{s}^{-1}</math> strain rate.</li> </ul>	[54]

				<ul style="list-style-type: none"><li>• Stress corrosion cracking occurs at lower strain rates (<math>10^{-7} \text{ s}^{-1}</math>) in the TMAZ/HAZ of the AA7075</li></ul>	
--	--	--	--	--	--

**Table 7-4. Microstructure-sensitive fatigue modeling parameters for dissimilar FSWed  
AA6061-to-AA7050.**

	Constant	270 rpm	410 rpm	Description
	<b>Crack Incubation</b>	$C_m$	0.15	0.15
$C_n$		0.07	0.07	HCF coefficient in Modified Coffin Manson Law
$\alpha$		-0.75	-0.68	Ductility exponent in Modified Coffin Manson Law
$q$		2.8	2.8	Exponent in remote strain to local plastic shear strain
$y_1$		100	100	Constant in remote strain to local plastic shear strain
$y_2$		1000	1000	Linear constant in remote strain to local plastic shear strain
$\xi$		1	1	Geometric factor in micromechanics study
$r$		0.1	0.1	Exponent in micromechanics study
<b>Small Crack (MSC/PSC)</b>		$\omega$	1	1
	$\theta$	0	0	Load path dependent and loading combination parameter
	$\zeta$	1	1	Exponent in Small crack growth
	$C_I$	600000	1.0x10 <sup>6</sup>	HCF constant in small crack growth
	$C_{II}$	0.0009	0.0009	LCF constant in small crack growth
	$\chi$	0.32	0.32	Crack growth rate constant

**Table 0-5. Microstructure-sensitive fatigue modeling parameters for FSWed AA6061-to-AA6061 (460 rpm-205.4 mm/min).**

	Constant		Description
	<b>Crack Incubation</b>	$C_m$	0.22
$C_n$		0.1	HCF coefficient in Modified Coffin Manson Law
$\alpha$		-0.68	Ductility exponent in Modified Coffin Manson Law
$q$		2.3	Exponent in remote strain to local plastic shear strain
$y_1$		100	Constant in remote strain to local plastic shear strain
$y_2$		1000	Linear constant in remote strain to local plastic shear strain
$\xi$		2	Geometric factor in micromechanics study
$r$		0.3	Exponent in micromechanics study
<b>Small Crack (MSC/PSC)</b>		$\omega$	1
	$\theta$	0	Load path dependent and loading combination parameter
	$\zeta$	2	Exponent in Small crack growth
	$C_I$	100000	HCF constant in small crack growth
	$C_{II}$	0.006	LCF constant in small crack growth
	$\chi$	0.32	Crack growth rate constant

**Table 7-6. Microstructure-sensitive fatigue modeling parameters for FSWed AA7050-to-AA7050 (360 rpm-152.4 mm/min).**

	Constant		Description
	<b>Crack Incubation</b>	$C_m$	0.05
$C_n$		0.03	HCF coefficient in Modified Coffin Manson Law
$\alpha$		-0.63	Ductility exponent in Modified Coffin Manson Law
$q$		2.8	Exponent in remote strain to local plastic shear strain
$y_1$		100	Constant in remote strain to local plastic shear strain
$y_2$		100	Linear constant in remote strain to local plastic shear strain
$\xi$		1	Geometric factor in micromechanics study
$r$		0.5	Exponent in micromechanics study
<b>Small Crack (MSC/PSC)</b>		$\omega$	0.8
	$\theta$	0	Load path dependent and loading combination parameter
	$\zeta$	6.5	Exponent in Small crack growth
	$C_I$	400000	HCF constant in small crack growth
	$C_{II}$	0.05	LCF constant in small crack growth
	$\chi$	0.32	Crack growth rate constant

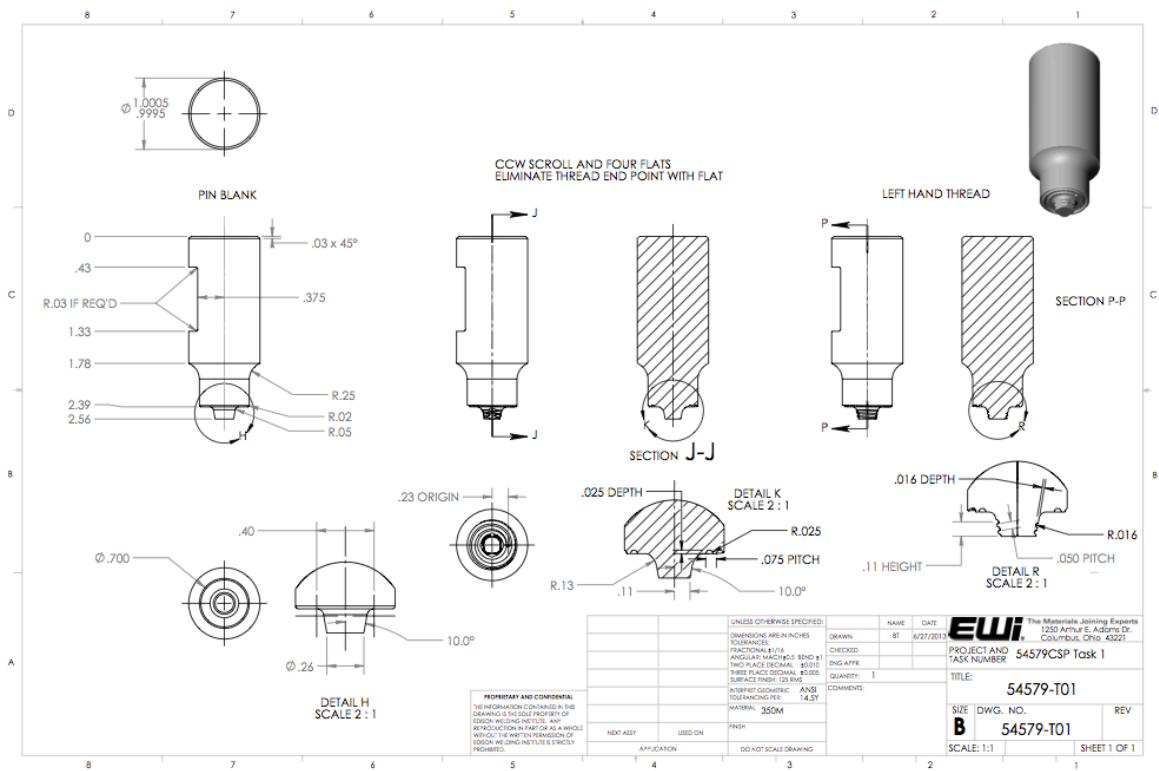


**Figure 7-1. Design of the FSW used for the samples preparation of this study.**